

Monte Carlo Dosimetry of Total Body Irradiation

by

Levi Burns

B.Sc (Hons.), Queen's University, 2016

A THESIS SUBMITTED IN PARTIAL FULFILLMENT
OF THE REQUIREMENTS FOR THE DEGREE OF

Master of Science

in

THE FACULTY OF GRADUATE AND POSTDOCTORAL
STUDIES
(Physics)

THE UNIVERSITY OF BRITISH COLUMBIA
(Vancouver)

April 2018

© Levi Burns, 2018

Abstract

The total body irradiation (TBI) technique at the Vancouver Cancer Centre uses a sweeping Cobalt-60 beam with patient-specific lung compensators and a stationary flattening filter, with the patient lying in supine and prone positions during each fraction. The dose calculations for this technique are limited to the dose delivered to a point at patient mid-separation at the level of the umbilicus, and the mean dose to the body must fall within a 10% tolerance of prescription. While the current technique is effective, it has been in place for over 23 years, and detailed dose data to critical organs is necessary before the technique can be upgraded to a more conformal technique that would offer an improved patient experience.

For this purpose, a Monte Carlo simulation technique has been developed and applied to collect organ dose data from TBI treatments based on retrospective data of patients recently treated with 12 Gy in 6 fractions. 20 patients, including adults and pediatric patients, are simulated by constructing Monte Carlo phantoms in each of the supine and prone positions based on planning CT images. The supine and prone dose distributions are summed with a deformable registration tool and the doses to the lungs, kidneys, thyroid, and liver are analyzed as well as the dose delivered to the body. It is determined that while all doses fall within prescription, there is a trend where smaller patients receive lower mean body doses and vice-versa (mean body dose range: 10.93-12.01 Gy). For most patients, the lungs and liver consistently receive doses below the mean body dose, and the thyroid and kidneys consistently receive higher doses than the mean body dose.

This thesis presents an overview of the background physics and biology of TBI as well as a comprehensive survey of different techniques described in the literature. The Monte Carlo simulation technique used for the retrospective study is described with calibration, validation, and optimization details, and the organ dose results of the retrospective study are shown.

Lay Summary

Total body irradiation (TBI) is a treatment used primarily to prepare a patient for a bone marrow transplant. While the TBI technique at the Vancouver Cancer Centre is effective, an upgrade is being considered based on recent advances in radiation therapy technology that would improve the patient experience. Before such a modern technique can be installed, organ dose data from the current technique are required at a more detailed level than what has been needed clinically to date. This thesis presents a method of collecting this organ dose data by performing computer simulations of the TBI treatments of recently treated patients. It is shown that there are consistent organ dose patterns across the patient population, and this will inform the design of the next generation TBI technique.

Preface

This thesis was completed by the author, Levi Burns, at the Vancouver Cancer Centre, and represents a continuation of work done by a previous UBC doctoral student, Dr. Tony Teke. Use of patient data was cleared by the institutional research ethics board (REB #H17-02276).

A report based on preliminary versions of Chapters 4 and 5 has been accepted for publication:

L Burns, T Teke, I A Popescu, C Duzenli. Monte Carlo dosimetry of organ doses from a sweeping-beam total body irradiation technique: feasibility and first results. Proceedings of the World Congress on Medical Physics and Biomedical Engineering. Accepted March 2018, in press.

Further publications are in preparation which will build on the results presented in Chapters 4 and 5.

Table of Contents

Abstract	ii
Lay Summary	iii
Preface	iv
Table of Contents	v
List of Tables	viii
List of Figures	ix
List of Abbreviations	x
Acknowledgements	xii
1 Introduction	1
1.1 Purpose	1
1.2 Overview	2
2 Background biology and physics	3
2.1 Bones and blood	3
2.1.1 Stem cells	3
2.1.2 Hematopoiesis and bone marrow	4
2.1.3 Blood cells	7
2.2 Cancer	7
2.2.1 The hallmarks	7
2.2.2 Hematological malignancies	9
2.2.3 Hematological malignancies in Canada	10
2.2.4 Bone marrow transplants	12

2.3	Physics	13
2.3.1	Light-matter interactions	13
2.3.2	Radiobiology and dose	16
2.3.3	Radioactivity and Cobalt-60 radiotherapy units	18
3	Total body irradiation (TBI)	21
3.1	Historical development	21
3.2	Modern TBI	23
3.2.1	Fractionation, dose, and dose rate	23
3.2.2	Worldwide heterogeneity in techniques	24
3.2.3	Advances in conventional TBI	26
3.2.4	Toxicities	29
3.2.5	Helical tomotherapy and VMAT	33
3.2.6	Total marrow irradiation and total lymphatic irradiation . .	37
3.2.7	Treatment planning systems and in-vivo dosimetry	39
3.2.8	Monte Carlo dosimetry	41
3.3	TBI at the Vancouver Cancer Centre	43
4	Monte Carlo dosimetry of the TBI technique in Vancouver	49
4.1	Introduction to Monte Carlo	49
4.1.1	History	49
4.1.2	Monte Carlo simulations in radiation oncology physics . .	50
4.1.3	EGSnrc	53
4.2	Phantom production for TBI simulations	54
4.3	Simulations	58
4.3.1	Cobalt source model	58
4.3.2	Simulation procedure and de-noising	58
4.3.3	Optimization	60
4.3.4	Calibration	61
4.3.5	Validation measurements	64
4.4	Deformable registration of dose distributions	68

5	Retrospective dose analysis of a TBI patient cohort	72
5.1	Purpose and aim	72
5.2	Methods: patient selection and contouring	73
5.3	Results and discussion	76
6	Future work	83
6.1	Ongoing investigations	83
6.2	Conclusion	86
	Bibliography	88

List of Tables

Table 2.1	Incidence and mortality statistics of hematological cancers in Canada	10
Table 4.1	Abridged results of an optimization study	61
Table 4.2	Measurement and simulation results from the validation measurements	69
Table 5.1	Aggregate organ dose results across the 20 simulated patients .	77
Table 5.2	Standard deviation data of the doses delivered to each organ . .	77

List of Figures

Figure 2.1	Diagram of a typical long bone in the human body	5
Figure 2.2	The hierarchies of different types of blood cells	6
Figure 2.3	Relative probabilities of photon interactions in medical physics.	16
Figure 2.4	The Cobalt-60 unit at the Vancouver Cancer Centre	19
Figure 3.1	Schematic representation of a TBI treatment at the VCC . . .	45
Figure 3.2	CT images of a TBI patient with radio-opaque markers	46
Figure 4.1	Flowchart describing the basic elements of a Monte Carlo simulation of charged particle transport	52
Figure 4.2	A section of an egphant file modelling a lung compensator . .	54
Figure 4.3	Slices of a Monte Carlo phantom of a patient	57
Figure 4.4	Isodoses from three dose distributions produced in an optimization study	62
Figure 4.5	Setup of the calibration measurement	64
Figure 4.6	Simulated dose distribution from the calibration measurement.	65
Figure 4.7	Setup used for the validation measurements	67
Figure 4.8	Simulated dose distribution for the validation measurements. .	68
Figure 4.9	Final results of a Monte Carlo simulated TBI patient treatment.	70
Figure 5.1	Organ contours shown for a simulated patient.	75
Figure 5.2	Variation of TBI mean body dose with patient size for the 20 patients.	78
Figure 5.3	PDD curves for parallel-opposed beams at extended SSD . .	79
Figure 5.4	The homogeneity indices of the dose delivered to the body contour against body size	80
Figure 5.5	Organ dose data plotted against mean body dose for lungs, kidneys, liver and thyroid.	81
Figure 5.6	Dose-volume histogram for a simulated patient.	82

List of Abbreviations

ALL	acute lymphoblastic leukemia
AML	acute myeloblastic leukemia
BMT	bone marrow transplant
CLL	chronic lymphoblastic leukemia
CML	chronic myeloblastic leukemia
CT	computed tomography
DVH	dose-volume histogram
GVHD	graft-versus-host disease
HI	homogeneity index
HL	Hodgkin's lymphoma
HSC	hematopoietic stem cell
HT	helical tomotherapy
IMRT	intensity-modulated radiation therapy
MC	Monte Carlo
MOSFET	metal oxide semiconductor field effect transistor
MU	monitor unit
MVCT	megavoltage computed tomography
NHL	non-Hodgkin's lymphoma
OAR	organ at risk

OSLD	optically stimulated luminescent dosimeter
PDD	percent depth dose
POP	parallel-opposed pair
PTV	planning target volume
RIC	reduced intensity conditioning
QA	quality assurance
SSD	source-to-surface distance
TBI	total body irradiation
TLD	thermoluminescent dosimeter
TLI	total lymphatic irradiation
TMI	total marrow irradiation
TMLI	total marrow and lymphatic irradiation
TPS	treatment planning system
VCC	Vancouver Cancer Centre
VMAT	volumetric modulated arc therapy

Acknowledgements

I have been enormously fortunate throughout my graduate studies to be able to brag to people about the amazing company I have had along the way. Between all of the physicists, physics assistants, students, and staff at BC Cancer, I was never deprived of mentorship, technical help, or entertainment as my degree moved along, for which I am boundlessly grateful.

There are several contributions to recognize specifically. I would like to thank Conrad Yuen, Susan Zhang, and Tony Popescu for their support in bringing my project to the finish line and beyond, as well as Claudia Mendez and Ron Horwood for their assistance with measurements, Nevin McVicar for his MIM wizardry, and Steven Thomas for his revisions and helpful comments on this thesis. To Tony Popescu and Tony Teke, thank you for your patience and enthusiasm in teaching me the ways of Monte Carlo and for your encouragement throughout the project. Most importantly, to Cheryl Duzenli for taking me on as a graduate student, for being endlessly supportive of me in my pursuits, for creating opportunities for me, and for your guidance, advice, physics wisdom, and open door; it has been a pleasure and a privilege to work with you. Lastly, to Byron Wilson and Youssef Ben Bouchta, for the brainstorming, life chats, and camaraderie in our grotto downstairs, and the many laughs that I look forward to continuing beyond our time as grad students.

Chapter 1

Introduction

1.1 Purpose

In treating cancer with radiotherapy, the goal is to treat a target at a prescription dose while minimizing the dose delivered to organs at risk. Radiation oncology is a collaboration between skilled professionals including, but certainly not limited to, radiation oncologists who select the planning target volume (PTV) and the prescription dose, radiation therapists who work directly with patients to prepare and deliver their treatments, and medical physicists who ensure that planned treatments will correctly deliver the prescription dose to the target volumes, commission new techniques, perform quality assurance, and carry out research to improve existing treatments, among other responsibilities.

Total body irradiation (TBI) is a radiotherapy treatment typically employed to prepare a patient for a bone marrow transplant. TBI is a unique treatment in that the entire body is the PTV, rather than a localized tumour or specific region of interest. Treating the entire body at a single prescription dose is a challenging task for many reasons including the large size of a patient compared to the size of conventional radiation field sizes, the heterogeneous tissue composition of the body, and the fact that the dose delivered by a radiotherapy beam decreases with depth as it travels through the patient.

The TBI technique at the Vancouver Cancer Centre (VCC) is effective and has been in place for over 23 years. However, given the advances in radiation oncology physics in these years, it has become feasible to raise the quality of our technique to a new standard with improved homogeneity of dose throughout the patient and more flexibility to reduce the dose delivered to critical organs that do not require the full body prescription. The team at the VCC is considering such an

upgrade which will move from a sweeping Cobalt-60 beam to a technique using a linear accelerator (linac). Before this transition can be made, a more detailed understanding of the doses delivered to each organ at risk (OAR) in the body is required from the current method.

In this thesis, a Monte Carlo dosimetry technique is developed and applied to simulate TBI treatments of a retrospective patient cohort. The resulting three-dimensional dose distributions will both serve as a basis for our upgrade and provide a new quality assurance (QA) tool for the existing treatment.

1.2 Overview

Chapter 2 provides a brief introduction to topics in physics, anatomy, physiology, and medicine that are relevant to the research. It is written to answer the following questions to a non-specialist audience: what is cancer, what does it mean for our blood to have cancer, and how does physics play a role in treating it?

Chapter 3 concerns total body irradiation (TBI). Most of the chapter is a literature review of modern TBI techniques, and section 3.3 details the current technique at the VCC. This chapter is written with the dual intention of situating the research of this thesis in the literature and serving as a reference for the VCC clinical team as the upgraded techniques continues to be developed.

Chapter 4 describes the Monte Carlo method as it pertains to radiation oncology physics. This chapter explains the methodology of the research project in producing simulated organ dose data, including a brief optimization study and details of how our simulations are validated against dosimeter measurements.

Chapter 5 presents a retrospective dose-volume analysis of organs at risk in TBI patients treated recently at our centre, and is an illustration of how the designed Monte Carlo dosimetry technique can be applied. 20 patients were simulated with body and organ doses presented. The ongoing and future work based on this project are described in Chapter 6.

Chapter 2

Background biology and physics

2.1 Bones and blood

2.1.1 Stem cells

In 1665, the term “cell” was coined by Robert Hooke in his ground-breaking work, *Micrographia*, used to describe the microscopic units that make up a slice of cork. The following two centuries brought scientists closer and closer to the conclusion that this subdivision into small units applies to living organisms as well. The official formulation of biological cell theory is considered to have occurred in 1838 and 1839 by Matthias Jakob Schleiden and Theodor Schwann. Several years later, Rudolf Virchow built on these ideas and provided history with a famous line, *omnis cellula e cellula*: All cells come from cells [1].

More recent work allows 21st century scientists to be more specific. Organisms begin as one cell that will undergo many divisions to become a full lifeform, and most of these cells become highly specialized for a certain purpose; for example, muscle cells are very different from brain cells. A given specialized cell cannot give rise to a different specialized cell by ordinary cell division. Stem cells, on the other hand, can divide to give rise to many different kinds of specialized cells through a process called differentiation. The division of stem cells is asymmetric such that the products include not only a new cell that will differentiate, but also a new stem cell to replace the mother stem cell [2].

The first cell in a human is the zygote, a fertilized egg produced by a female egg cell and a male sperm cell. The zygote is the ancestor of all other cells in the organism and thus sits at the highest level of the stem cell hierarchy, classified

as a totipotent stem cell [2, 3]. The next cells in the development line are called pluripotent stem cells, which can divide into any type of human tissue but are unable to produce a full organism independently. Following these are multipotent stem cells, which can differentiate into different cell types of a given lineage. One population of multipotent stem cells in the human body, and one of the best-studied types of stem cell, is the hematopoietic stem cell (HSC)¹. Like all stem cells, HSCs have the capacity for self-renewal and give rise to a line of more specialized cells, these being the cells of the blood.

We can now refine Virchow's famous statement for the purposes of this thesis: all blood cells come from hematopoietic stem cells. This process is called hematopoiesis.

2.1.2 Hematopoiesis and bone marrow

Hematopoiesis occurs throughout the yolk sac in the first few weeks of fetal life. From six weeks until six to seven months of gestation, the liver and the spleen are the major blood-producing organs. Towards the end of pregnancy, the bone marrow becomes the most important site of hematopoiesis, and becomes the only source of new blood cells after a few weeks past birth [5]. Thus, further discussion of blood formation first requires a discussion of bones.

An adult human skeleton has 206 bones [3]. Bone tissue can be classified as either cortical bone, which is dense, solid, and forms the exterior portion of most bones, or as trabecular bone (also known as spongy bone) which threads through the interior of the bones. About 80% of adult human bone is cortical, although the ratio of cortical to trabecular bone varies widely within individual bones in the body [6, 7].

Internal cavities exist in most bones and these are usually filled with bone marrow, which is a softer tissue [3, 6]. There are two types of bone marrow: yellow bone marrow, which contain fatty tissue that can serve as an energy source, and red bone marrow, which is where hematopoiesis takes place. The bone marrow provides a microenvironment that is suitable for HSCs to divide, self-renew, and differentiate. Accordingly, the bones play a key role in regulating blood formation

¹There is some debate in the literature as to whether HSCs should be considered pluripotent in light of recent research into their plasticity [4], but this is outside the scope of this discussion.

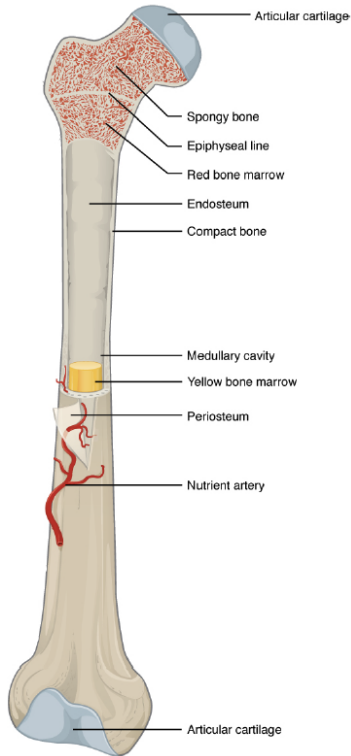


Figure 2.1: Diagram of a typical long bone in the human body. Blood cells are formed in the red bone marrow. Image source: Anatomy and Physiology, OpenStax [3] (edited).

[8]. A diagram of a typical long bone is given in Figure 2.1.

In infants, almost all bones in the body contain blood-producing red marrow regions, but these regions are gradually replaced by yellow marrow regions with age. In adults, hematopoietic marrow exists only in the central skeleton and the proximal ends of the femurs and humeri (that is, the ends that are closer to the center of the body), and even these regions only consist of approximately 50% red marrow. Under extraordinary circumstances, such as the destruction of bone marrow by bone cancers, the spleen and liver can recommence their natal production of blood cells through extramedullary hematopoiesis [3, 5].

There are relatively few HSCs in the bone marrow cell population, roughly one per 20 million nucleated cells, but each HSC is capable of producing one million

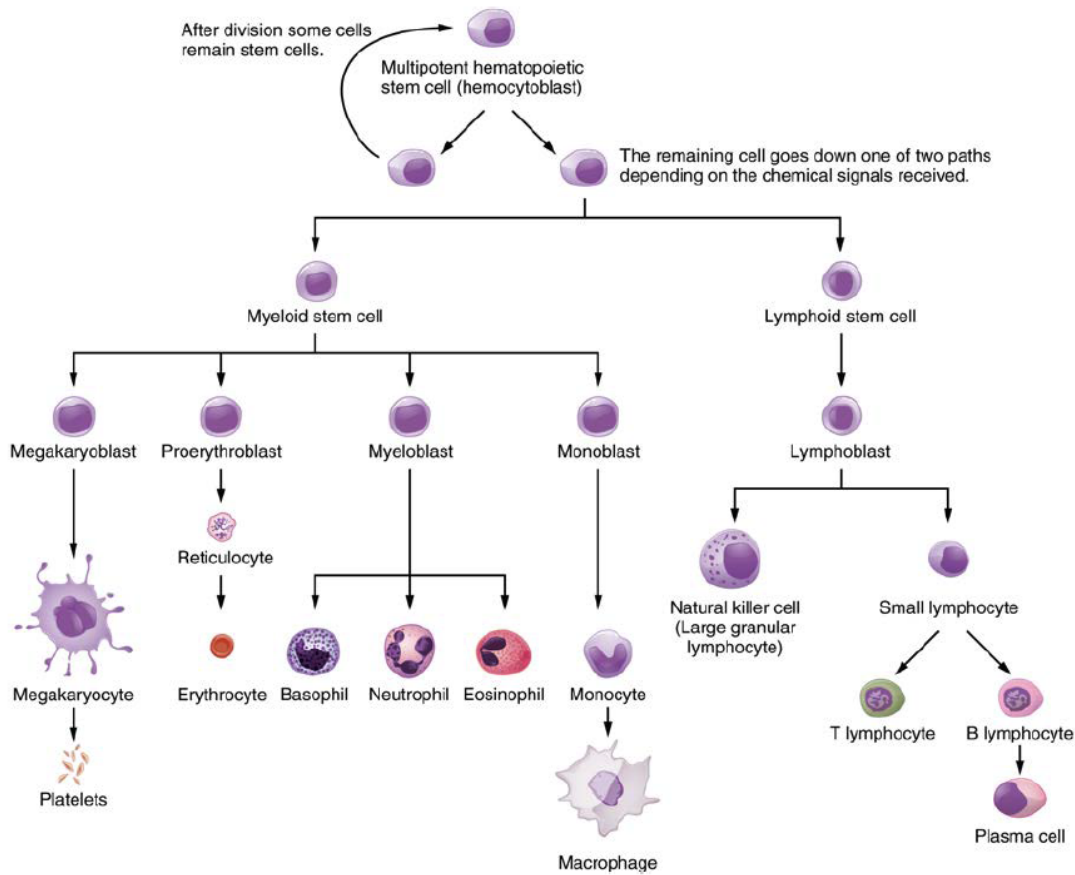


Figure 2.2: Different types of blood cells, shown in hierarchical order beginning with the asymmetric division of a hematopoietic stem cell (HSC). The blood cells on the left hand side are of myeloid lineage, and on the right hand side, lymphoid lineage. Image source: Anatomy and Physiology, OpenStax [3].

mature blood cells after twenty divisions. The types of blood cells that will arise from each division depend on a complex interplay of growth factors and extracellular signals received by each HSC from the cellular environment [5]. Each HSC division gives rise to either a myeloid stem cell or a lymphoid stem cell which differentiate further as shown in Figure 2.2.

2.1.3 Blood cells

In an average adult, blood constitutes roughly 8% of the body mass [3]. Blood is comprised of various cells and cellular fragments collectively known as the formed elements, as well as the fluid that suspends these elements, which is called plasma.

The formed elements consist of platelets, erythrocytes (red blood cells), and leukocytes (white blood cells), as shown in Figure 2.2. Platelets, each with a lifetime of about 10 days, make up less than 1% of the formed elements and are primarily involved in healing damaged tissue and preventing blood loss following injury to a blood vessel. Erythrocytes make up over 99% of the formed elements and each cell has a lifetime of about 120 days. They are responsible for transporting inhaled oxygen from the lungs to nourish the other cells in the body, and for transporting carbon dioxide produced as byproducts of bodily functions to the lungs for exhalation.

Many types of leukocytes exist, and these are primarily involved in immunity. The eosinophils, neutrophils, and basophils are collectively referred to as granulocytes. The granulocytes and monocytes follow a myeloid lineage. On the other hand, lymphocytes (of lymphoid lineage) are labelled as either B lymphocytes or T lymphocytes depending on whether the precursor lymphoid stem cell matured in the bone marrow (B cells) or in the thymus gland (T cells). While red blood cells and platelets are confined within the vascular system, leukocytes are able to leave the circulation to reach other tissues. Lymphocytes are the only leukocytes that can return to the circulation afterwards [3, 6].

2.2 Cancer

2.2.1 The hallmarks

One day, we imagine that cancer biology and treatment [...] will become a science with a conceptual structure and logical coherence that rivals that of chemistry or physics.

— Weinberg and Hanahan, The Hallmarks of Cancer, 2000 [9]

Cancer has been recognized as a disease for millennia, with the earliest known description of a breast tumour recorded in hieroglyphs by Imhotep, an ancient

Egyptian physician, dating to 2500 BC. In brief, cancer can be considered a disease of uncontrolled cell growth. But, given the thousands of different forms of cancer that can affect virtually any part of the body, the symptoms of cancer vary vastly, and physicians for much of history were mystified by the complex illness. Little progress in cancer treatment was made for several thousand years.

Fortunately, scientific advances in the 19th and 20th centuries began to produce treatments that would go on to meaningfully prolong the lives of patients of many cancer types, whether by cure or palliation. The advent of molecular biology in the late 20th century in particular has given researchers an unprecedented wealth of information about the disease at a microscopic level [10, 11].

In 2000, a review article by Douglas Hanahan and Robert Weinberg was published that set the tone for discussions of cancer biology into the 21st century. They outlined six “Hallmarks of Cancer” that govern the production and the growth of tumours, synthesizing an enormous amount of information collected about the disease up to that point in time. Since then, further research, debate, and discussion have identified two additional hallmarks, leading to a total of eight features that are more descriptive of cancer than the simple “uncontrolled cell growth” [9, 10, 12]:

1. Self-sustaining growth signalling; that is, cancer cells provide their own instructions to grow, rather than being directed to do so externally
2. Insensitivity to anti-growth signals that ordinarily suppress tumour growth
3. Evasion of programmed cell death (apoptosis)
4. Limitless replicative potential; normally, cells can only divide a certain number of times
5. Ability to build their own supply of blood (angiogenesis)
6. Ability to metastasize; that is, to travel through the body and initiate a new cancer site elsewhere
7. A rewiring of cellular metabolism processes, redefining how cancer cells produce their energy
8. Evasion of immune system responses

2.2.2 Hematological malignancies

Rather than taking the form of a solid tumour like many other types of cancer, cancers of the blood begin as an affliction of blood-producing HSCs. From there, production of blood cells is altered. Hematological malignancies can be broadly split into three categories: leukemia, lymphoma, and myeloma. These can be split further into many subcategories. Here, we go into detail for a subset of classifications of blood disease encompassing the majority of cases.

Leukemia can be either myelogenous or lymphoblastic, corresponding to a disease of either too many myeloblasts or too many lymphoblasts, respectively. These are also divided into either acute or chronic disease, as the symptoms can either arise and progress quickly on the span of days or weeks, or slowly on the span of months or years. Acute lymphoblastic leukemia (ALL) is most common in young children. Acute myeloblastic leukemia (AML) is the most common type of leukemia in adults, with the median age of diagnosis being 65 years. Chronic lymphoblastic leukemia (CLL) most often appears in patients in their seventies, where there are too many abnormal B lymphocytes. Chronic myeloblastic leukemia (CML) is of particular interest in the development of cancer research as a whole, as it represents the first time that a specific type of cancer was linked to a consistent chromosomal aberration: the Philadelphia chromosome, a translocation of chromosomes 9 and 22 [13, 14]. The chromosomal basis of cancer is described further in section 2.3.2. Recent research has identified leukemic stem cells which are resistant to traditional therapeutic approaches and may explain why some leukemias relapse [15].

Lymphoma involves the lymphatic system, which includes the spleen, tonsils, lymph vessels that transport waste products and pathogens away from our cells, and lymph nodes that filter lymph fluid. It is traditionally classified as either Hodgkin or non-Hodgkin lymphoma (HL or NHL): while NHL has many forms and can develop almost anywhere in the body, in either indolent or aggressive forms and in B or T lymphocytes, HL is well-defined by the presence of Reed-Sternberg cells, which are mature B cells that have become large, malignant, and have several nuclei. HL typically develops in lymph nodes of the upper body [13, 14]. One precursor for lymphoma is human immunodeficiency virus (HIV) [5].

	New cases		Deaths	
	Men (103,100)	Women (103,200)	Men (42,600)	Women (38,200)
Non-Hodgkin lymphoma	4.5%	3.6%	3.5%	3.1 %
Hodgkin lymphoma	0.6%	0.4%	0.2%	0.2 %
Leukemia (all types)	3.5%	2.5%	3.9%	3.3 %
Multiple myeloma	1.6%	1.2%	1.9%	1.7 %

Table 2.1: Projected numbers of new cases and deaths from hematological malignancies in Canada for the year 2017. Numbers are given as percentages of the total number of new cases and deaths in Canada across all cancer types, given in parentheses. Data from reference [20].

Finally, multiple myeloma - the most common form of myeloma - is a B-cell malignancy, where plasma cells are overproduced, which in turn overproduce immunoglobins that build up in the bone marrow. The median age at diagnosis is 70 years with bone pain being a common symptom. While multiple myeloma is highly treatable, it is a complex disease that remains incurable [16, 17].

Beyond the scope of this thesis, each of these cancer types can be subdivided further. In fact, there are over 70 types of leukemia, and over 90 types of lymphoma [18, 19].

2.2.3 Hematological malignancies in Canada

Every year, the Canadian Cancer Society publishes a comprehensive report describing Canadian cancer incidence and mortality by disease type. This section is a brief overview of the information from the 2017 report concerning leukemia, lymphoma, and multiple myeloma [20].

In 2017, it is estimated that 206,200 new cancer cases were diagnosed in Canada with 80,800 cancer deaths. Hematological malignancies are relatively rare compared to other cancers, with information about new cases and deaths for leukemia, multiple myeloma, HL, and NHL given in Table 2.1. For comparison, 20.7% of new cases in men were expected to be prostate cancer, and 25.5% of new cases in women were expected to be breast cancer.

The largest risk factor for developing cancer is age, and 89% of new cases are

expected to be in people over 50. This means that the rate of cancer incidence is bound to increase in a country with an aging population such as Canada. However, age-standardized incidence rates and age-standardized mortality rates can be produced that compare cancer cases across many years as if the population structure was not aging. These reveal that for many cancers, the age-adjusted mortality and incidence rates are actually decreasing, despite an increasing number of cases due to aging demographics, and the total age-adjusted mortality rate from all forms of cancer is decreasing (although this varies substantially based on the type).

Lymphoma, both HL and NHL, are two cancers with notable declines in mortality rates. For HL, mortality has decreased by 2.6% per year since 1992, owing to improved treatments. For NHL, mortality decreased between 2.3% and 2.5% per year between 2000 and 2012. A notable contributor to this decrease is the use of highly active antiretroviral therapy (HAART) beginning in the late 1990s to combat HIV, corresponding to a decrease in the number of aggressive lymphoma cases owing to the virus.

The incidence statistics for leukemia vary drastically for pediatric patients compared to the general public. While only 0.7% of new cancer cases in Canada occur in people 19 years or younger, leukemia and lymphoma are two of the most common cancers in the patient cohort aged 0-14 years (32% of childhood cancers are leukemias, and 11% are lymphomas). Overall, survival for childhood cancers is higher than for adult cancers.

In a study comparing Canadian cancer cases in two time periods, between 1992-1994 and between 2006-2008, five-year age-standardized net survival increased from 53% to 60% for all cancers combined. The largest increases in survival across all cancers between these two time periods were seen in NHL (15% increase), leukemia (15% increase, varying by subtype from 9% for AML to 25% for CML), and multiple myeloma (14% increase). In 2006-2008, HL had the third-highest rate among cancers of five-year survival (87% in women and 83% in men).

A final note in this section is that survival statistics describe patients treated in the past. In reality, if advances in medicine are constantly improving healthcare, the survivability of diseases is always higher than previously reported due to advances in detection and treatment compared to of past patients.

2.2.4 Bone marrow transplants

Bone marrow transplants (BMTs) are a treatment option for some patients with hematological malignancies. The procedure involves collecting stem cells to deliver to a patient by infusion. BMTs can be allogeneic, where they receive stem cells from a matched donor, or autologous, where the stem cells are collected from the patient and then re-infused after a treatment. In the earlier days of chemotherapy, the biological dose limit that could be delivered to the bone marrow was a limiting factor in the amount of chemotherapy that could be given to a patient [11]. Bone marrow transplants effectively raise the dose limit of chemotherapy or radiation that can be delivered without mortality, and are sometimes referred to as rescue treatments [13, 14].

Cancer patients who receive bone marrow transplants must first receive a conditioning regimen to destroy unhealthy stem cells. This is done with either chemotherapy, radiation, or a combination of both. Regimens including TBI are an option for patients with relapsed disease who may have become chemo-resistant from earlier treatments, or for patients where sanctuary sparing from chemotherapy may be a particular concern (e.g. in the testes or central nervous system). A prophylactic treatment is normally given to suppress the immune system to prevent the onset graft-versus-host disease (GvHD). There is also a graft-versus-tumour or graft-versus-leukemia effect that some recent treatments take advantage of by using reduced intensity conditioning [13, 21]. With an autologous transplant, there is no risk of GvHD, although the relapse rates may be higher. The results of some clinical trials are discussed in section 3.2.4.

While many centres have historically been reluctant to treat patients of an advanced age with BMTs (with upper age limits around 55-60 years), a recent clinical trial demonstrated that while the number of comorbidities does reduce the chance of patient survival following such a BMT, age alone does not predict survival. Based on this, referrals for a BMT should be based on patient condition rather than biological age [21, 22].

The terms “bone marrow transplant” and “stem cell transplant” are used interchangeably by the general public. BMTs originally involved collecting donor bone marrow from the bone itself, while more recent technology allows for stem

cell collection from the blood, called a “peripheral blood stem cell transplantation”. The only difference between this and a BMT are the source of the collected stem cells [14]. A recent meta-analysis spanning 1,224 patients of either peripheral blood transplants or bone marrow transplants have shown similar overall survival and mortality rates, with peripheral blood transplants having improved disease-free survival, a decrease in relapse, and increased GvHD for hematologic malignancy treatment [23].

2.3 Physics

2.3.1 Light-matter interactions

The role that physics plays in the treatment of cancer begins with an understanding of light-matter interactions [24–26].

Electromagnetic radiation, which encompasses all types of electromagnetic waves including radio waves, visible light, gamma rays, and the therapeutic X-rays used in radiotherapy, is conceptualized as small packets of energy called photons. As radiation travels from an isotropic source, it spreads over a larger area as it propagates and spreads out. As a result, the number of photons per unit area decreases, and the radiation becomes less intense in proportion with the square of the distance travelled. This effect is called the inverse square law,

$$\frac{\Phi_1}{\Phi_2} = \frac{r_2^2}{r_1^2} \quad (2.1)$$

where Φ_1 and Φ_2 are the photon fluences at two points corresponding to distances r_1 and r_2 from the source of the radiation.

When photons travel through matter, the distance travelled before interacting with the medium can be estimated from the linear attenuation coefficient, μ , which is the fraction of photons that attenuate per unit thickness of attenuating material. The value of μ depends on the energy of the photon and the electron density of the material. The attenuation of a photon beam over a distance x is exponential,

$$N = N_o e^{-\mu x} \quad (2.2)$$

where N_o and N correspond to the number of photons in the beam at the origin and at a distance x , respectively.

There are four light-matter interactions that form the basis of radiation oncology physics:

Rayleigh scattering: An incoming photon interacts with the electrons of an atom in the medium, and is deflected away in a new direction without loss of energy to the medium.

Photoelectric effect: An incoming photon is fully absorbed by an atom in the medium. An amount of energy, E_{tr} , is then transferred away from the atom by an ejected electron carrying the energy $h\nu$ of the incident photon less the binding energy E_b that originally held this electron in place in the atom,

$$E_{tr} = h\nu - E_b. \quad (2.3)$$

The resulting inner-shell electron vacancy can then be filled by a higher-shell electron in the atom. This transition results in a new photon being emitted from the atom with an energy equal to the difference between the binding energies of the shells in the transition. For large transitions, these photons can eject more electrons from the atom which are then called Auger electrons.

Compton scattering: An incoming photon of energy $h\nu$ interacts with an electron of an atom in the medium. The electron is knocked out of the atom and carries away with it an energy given by E_{tr} ,

$$E_{tr} = \frac{\frac{h\nu}{m_e c^2} (1 - \cos(\theta))}{1 + \frac{h\nu}{m_e c^2} (1 - \cos(\theta))} \quad (2.4)$$

where c is the speed of light, m_e is the mass of an electron, and θ is the scattering angle of the photon. The incident photon continues in a new direction after deflecting with the atom, with less energy.

Pair production: An incoming photon interacts with the nuclear field of an atom and is converted to an electron and a positron. The photon must have

energy of at least $2m_e c^2$, or 1.022 MeV, corresponding to the rest mass of an electron and positron combined. The total energy transferred to the charged particles is given by

$$E_{tr} = h\nu - 1.022 \text{ MeV}. \quad (2.5)$$

Another interaction that is possible is triplet production, where a photon interacts with the field of an electron in an atom to produce three charged particles. The threshold energy of this interaction is 2.044 MeV which is above the energy scales used in this thesis with a Cobalt-60 unit (described in section 2.3.3).

The attenuation coefficient μ can be written in terms of the interaction cross-sections for each of these processes,

$$\mu = \sigma_R + \tau + \sigma_C + \kappa \quad (2.6)$$

where the four variables on the right-hand side correspond to Rayleigh scattering, photoelectric absorption, Compton scattering, and pair production. The relative probabilities of these interactions depend on the energy of the photons and the atomic number of the medium. These probabilities for water are shown in Figure 2.3.

Energy is transferred from photon beams to a medium in two steps. First, through these processes, energy is transferred from a photon beam to charged particles. Next, these charged particles deposit their energy elsewhere in the medium. Charged particles interact by collisional effects throughout their tracks, or they experience radiative energy losses where photons are produced that may go on to produce more charged particles. This radiative interaction is called bremsstrahlung, German for “braking radiation”.

Radiation comprising of photons is called indirectly ionizing radiation, and radiation comprising of charged particles is called directly ionizing radiation. The photons incident on a patient from radiotherapy sources, in and of themselves, are unable to cause any sort of biological or chemical changes. It is the charged particles they set in motion that are able to cause damage to cells, explained in the next section.

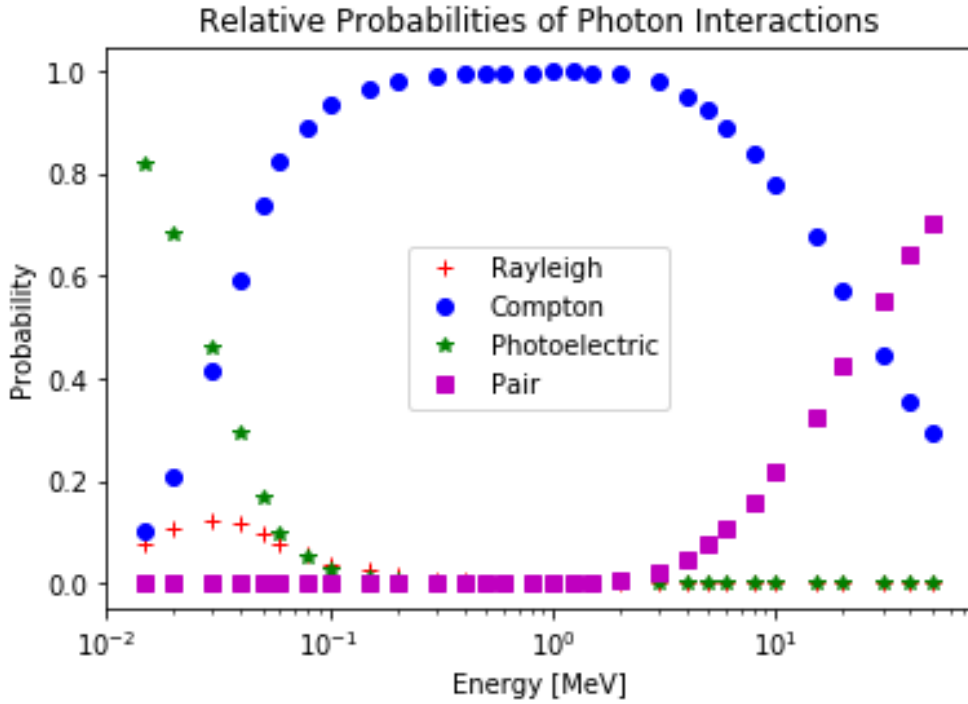


Figure 2.3: Relative probabilities of the four photon interactions described in section 2.3.1 as a function of photon energy for radiation travelling through water. The energies of concern in this thesis are 1.17 MeV and 1.33 MeV, described further in section 2.3.3.

2.3.2 Radiobiology and dose

DNA is the double-stranded helix that contains our genetic code in cell nuclei. DNA is tightly wound into a set of 46 structures called chromosomes, divided into 23 homologous pairs. When cells divide through mitosis, the genetic information is duplicated with a copy given to each daughter cell.

The strands of DNA are composed of many atoms with charged and uncharged portions. When charged particles are incident on DNA, there are many features in the orderly pattern of molecules and atoms in DNA that can be disrupted, and molecules may be broken apart due to these interactions. When a single DNA strand is broken (a single strand break, or SSB), there are several biological repair mechanisms available to fix this broken strand and repair the double helix

structure. However, when both DNA strands are broken in locations that are very close to each other (a double strand break, or DSB), it is much more difficult to repair the DNA correctly [27]. Chromosomal aberrations result from the incomplete or incorrect repair of chromosomes, such as the Philadelphia chromosome translocation mentioned in section 2.2.2. If there are chromosomal aberrations that go unrepaired, the cell will become dysfunctional in mitosis; either one or both daughter cells will be abnormal, or the process of mitosis may not be able to take place at all. As a result, ionizing radiation acts not to kill a cell immediately, but rather to induce reproductive death in the cell.

The induction of reproductive cell death can occur in both normal and cancerous tissue. Unfortunately, it is impossible to avoid completely the radiation of healthy tissue in radiotherapy. It is known that radiation can induce cancer as well as treat it. Notably, from following survivors of the atomic bombings in Hiroshima and Nagasaki in 1945, it is known that whole-body exposures to radiation can induce leukemia [5, 27]. Typically, these cancers have a long latency period before manifesting symptomatically, which can occur decades after a radiation therapy treatment [28]. Therefore, the aim of radiotherapy becomes to maximize the cell killing in cancerous tissue while sparing normal tissue to reduce the number or severity of treatment-related toxicities (side-effects).

The amount of cell killing increases in proportion with the radiation dose, that is, the amount of energy absorbed per unit mass in the medium. Dose is given a unit called the gray (Gy), where $1 \text{ Gy} = 1 \text{ J/kg}$. Also commonly used is the centigray (cGy), with $100 \text{ cGy} = 1 \text{ Gy}$. Because photons must first transfer their energy to damaging charged particles before energy is deposited in the medium, the maximum dose does not occur immediately at the surface of a patient when radiotherapy is delivered as a photon beam. Rather, there is a build-up region between the surface and the depth of maximum dose d_{max} . This depth is 0.5 cm for Cobalt-60 photon beams and increases with photon energy in other treatment modalities. After reaching d_{max} , the dose delivered decreases steadily with depth through the patient, measured relative to the maximum dose at d_{max} by a quantity called percent depth dose (PDD).

Dose can be measured by several means experimentally with dosimeters. There are many types of dosimeters and each has strengths and weaknesses that make

them suitable for measurement of dose in different settings. The dosimeter should provide an accurate measurement of the dose without changing the radiation beam. Another dosimetry technique, discussed at length in Chapter 4, is Monte Carlo dosimetry, where computer simulations are used rather than a physical device in the path of a beam. While Monte Carlo can be time consuming, requires heavy computational resources and careful validation measurements, it produces a full dose distribution of a given target without having to use clinical machine resources.

2.3.3 Radioactivity and Cobalt-60 radiotherapy units

It's these few eternally unstable elements that possibly hold the key to the fate of the world. They were first developed and employed for mass destruction. Now Canada has taken the lead in showing how they can be used for the mass benefit of mankind.
 — Eric Hutton, The Atom Bomb That Saves Lives, 1952 [29]

The previous sections describe the goal of radiotherapy and the mechanism by which therapeutic X-rays interact with matter. Finally, radioactivity enables a discussion of the origin of this cell-damaging radiation.

Matter is comprised at a fundamental level by atoms consisting of protons and neutrons in their nuclei. Some atomic nuclei are unstable and eventually undergo decay, leading to a new daughter nucleus along with byproducts depending on the decay mode. The rate of a radioactive decay is proportional only to the number of radioactive nuclei N in a given sample,

$$\frac{dN}{dt} = -\lambda N \quad (2.7)$$

where λ is the decay constant for the given decay mode.

In external beam radiation therapy, the most important radioactive isotope is Cobalt-60, with a half-life of 1921.5 days, or roughly 5 years and 3 months. 99.8% of Cobalt-60 decays occur first by decay to an excited state of Nickel-60, which then emits two photons of energies 1.173 MeV and 1.332 MeV [24]. Other subsequent decays from Cobalt-60 give rise to other photons with energies below and in between these two values [30]. It is these X-rays that provide useful radiation for



Figure 2.4: The Cobalt-60 unit at the Vancouver Cancer Centre. The radioactive Cobalt source is housed in a lead shielding unit in the treatment head.

radiotherapy². The implementation of Cobalt-60 for radiation therapy was a Canadian innovation, championed by Harold Johns with the first treatments on human cancer patients taking place in Saskatoon, Saskatchewan and London, Ontario in 1951 [29, 31]. In these units, a Cobalt-60 source is sealed in a lead shielding unit, until a treatment occurs when the source moves to the treatment head for its decay X-rays to pass through the beam collimator. A picture of the Cobalt unit in use at the VCC is shown in Figure 2.4.

At this energy range, in tissue, Compton scattering dominates heavily over any other light-matter interaction, until the photons scatter to lower energies where

²Often, the energy of Cobalt-60 is simply written as 1.25 MeV, the average of the two most common photons.

the photoelectric effect and Rayleigh scattering become noticeable. While Cobalt-60 photon energies are marginally above the threshold for pair production, the small amount by which they are over the threshold (and the low atomic number of tissue material) make this interaction infinitesimally rare. On the other hand, in lead, Cobalt-60 photons are still mostly attenuated by the Compton effect, but photoelectric absorption and pair production are occurring as well, each at roughly 5% of the frequency of the Compton interactions [26].

Chapter 3

Total body irradiation (TBI)

3.1 Historical development

The discoveries of the X-ray by Wilhelm Roentgen in 1895 and of radioactivity by Marie Curie in 1902, which lead to their awarding of Nobel Prizes in 1901 and 1903 respectively [32], quickly gave rise to many studies investigating the applications of these discoveries in medicine. Very shortly afterwards, TBI was proposed in 1905 by Friedrich Dessauer, a German biophysicist, in the same year that Einstein published his famous papers that included a description of the photoelectric effect. TBI was being advocated at the time as a treatment for leukemias. Dessauer had suggested TBI as a simultaneous irradiation of the patient by three different sources from the superior, inferior, and anterior directions to the patient [33].

The first unit constructed specifically for TBI was constructed at Memorial Hospital in New York [34], championed in May 1931 by Arthur Heublein who passed away less than a year later. This unit allowed for two patients to be irradiated simultaneously in adjacent rooms by the same low-voltage X-ray tube, for approximately 20 hours per day over one to two weeks [35]. The earliest publication describing “a new method of X-ray therapy consisting of continuous irradiation of the entire body at long distances from the tube” was published posthumously by Heublein in June 1932 [36].

Early interest in TBI was held not only by physicians, but also in secret by the officials of the Manhattan Project in World War II, and later on by the United States Department of Defense. Information about whole-body radiation exposures was considered valuable in the contexts of occupational exposures of workers developing nuclear weapons, determining whether the pilots of nuclear-powered airplanes would be at risk of developing radiation sickness, and in preparing a defense

and response strategy in the event of a nuclear strike. The involvement of the Department of Defense in hospital clinical trials was a source of controversy when it came to light, along with other ethical issues involved with these studies, and the final TBI trial that was funded by the Department of Defense at the University of Cincinnati was closed in 1971. In the 1990s, the administration of President Clinton struck the Advisory Committee on Human Radiation Experiments to study and report on such issues in detail. The final report of the committee included a chapter on TBI, among discussions of what research conducted with patients is considered therapeutic or non-therapeutic [37]. Fortunately, only this small subset of research in TBI is shrouded in ethical concerns.

Historically, TBI was used to treat malignancies that spanned the whole body, or as last resort treatment for patients with poor outcomes [37]. While the myeloablative, or cancer-fighting, properties of TBI were studied early on, its progress was dismal in fighting cancer compared to developments that were being made with chemotherapeutic approaches. However, TBI was recognized as an effective immunosuppressant and plays an important role in the history of organ transplantation to condition patients; in 1959, a successful solid organ transplant was performed for the first time between non-identical twins, a kidney, breaching a genetic barrier to organ transplantation for the first time, in a patient who had first received TBI [38, 39].

Pioneering research in the use of bone marrow transplants occurred in Seattle, championed by Dr. E Donnell Thomas in the early 1970s [34], who received the 1990 Nobel Prize in Physiology or Medicine for his work [32, 40]. The Seattle team conducted many groundbreaking experiments with TBI and bone marrow transplants, both in animal trials and in human clinical trials [39], some of which are outlined in subsequent sections of this report. In current practice, when TBI is given before a transplant, it is prescribed as only one part of the patient care plan alongside chemotherapy.

3.2 Modern TBI

3.2.1 Fractionation, dose, and dose rate

Early TBI prescriptions were typically given in one large fraction of 8-10 Gy, which involved a high risk of treatment-related mortality [40]. Many TBI studies throughout the 1980s and 1990s established a clear benefit of fractionation: by spreading the treatment over multiple days, patients were able to tolerate larger total doses. These studies included not only experiments with dogs receiving marrow infusions, many of which were from the Seattle group [41, 42], but also other studies of a theoretical nature based on radiobiological considerations [43, 44]. A randomized clinical trial in 1990 in Seattle found that overall survival from patients in two treatment arms, one receiving 12 Gy in 6 days and one receiving 15.75 Gy in 7 days, had similar overall survival, but the higher-dose arm saw more treatment-related mortality while the lower-dose arm had more relapse-related mortality [45]. 12 Gy in 6 fractions has widely become the most common TBI prescription.

The dose rate used in TBI treatments is typically low. A clinical trial in 1982 found that a dose rate above 6 cGy per minute was significantly correlated to mortality in acute leukemia patients receiving TBI, although it was confounded with other factors in the study, and a definitive conclusion could not be drawn [46]. A trial with dogs found that a lower dose rate lead to improved survival when receiving single-fraction doses of TBI, but in fractionated schemes, the results were less clear [42]. A more recent meta-analysis did not find a dose rate effect on the incidence of interstitial pneumonitis (a severe scarring of the lung tissue that can be fatal) [47], while a study produced around the same time indicated that there is an effect above 15 cGy per minute [48]. It has been suggested elsewhere that low TBI dose rates are important for optimal outcomes and reducing the risk of interstitial pneumonitis [49], but this has not been adopted universally and is not used as a limit in helical tomotherapy or volumetric modulated arc therapy techniques.

There are several distinct conditioning regimens that exist, reflected in different types of TBI prescriptions. The prescription of 12 Gy in 6 fractions falls under the myeloablative conditioning category where stem cell support is later required to rescue the patient. Nonmyeloablative regimens are those that produce minimal

loss of mature blood cells and stem cell support is not required afterwards for the patient. In between these two categories is reduced intensity conditioning (RIC), where it is possible that the patient could recover without further support, but there would be significant morbidity and mortality. Some lower-dose TBI prescriptions are given as parts of RIC techniques and suit patients who are not eligible for full myeloablative conditioning [50]. RIC, where a trade-off is made between reduced incidence of toxicities and an increased risk of relapse, has gained popularity since the late 1990s [51]. A graft-versus-tumour or graft-versus-leukemia effect can also be harnessed with RIC to combat the disease [52]. A recent study comparing 45 patients who received RIC to 135 patients receiving myeloablative conditioning found similar rates of overall survival and relapse, but with lower rates of toxicities in the RIC group [53].

Some recent early-stage clinical trials have revisited the concepts of dose escalation and TBI-only conditioning for patients with refractory disease or resistant relapses. One study for lymphoma patients had three patients in arms of 16 Gy, 18 Gy, and 20 Gy treatments, using lung and kidney shielding [54]. The feasibility of TBI-only conditioning was demonstrated, with only one patient in the 18 Gy arm developing severe lung toxicity. Another study of four leukemia patients receiving autologous transplants following TBI doses of 16 Gy again showed that this procedure was tolerable [55], likely due to improved treatment delivery systems and supportive care strategies in the time elapsed since the 12 Gy in 6 fraction regimen became the standard of care.

3.2.2 Worldwide heterogeneity in techniques

Clinics with TBI programs treat a very small volume of TBI patients compared to the total volume of patients receiving any kind of radiation treatment. A recent survey across Canadian cancer centres identified 12 centres that deliver TBI and found that around 400 patients per year receive TBI across the country [56]. For many reasons, there is enormous diversity in how TBI is delivered across the world; a recent European survey of 56 centres from 23 countries found no pair of centers delivering TBI the same way [57], which is also true of the Canadian survey. These reasons include the small patient volume, the number of degrees of freedom in the

planning of a TBI treatment - including the dose rate, fractionation schedule, beam energy, immobilization techniques, and organ dose constraints - and the inherent physics challenge of delivering a uniform dose to a large and non-uniform human body. The very small number of TBI patients makes it difficult to justify the construction of a dedicated TBI unit in a clinic, which leads to existing units being repurposed based on the equipment and expertise available at each centre. While these conditions allow for each treatment centre to develop a technique that best suits their personnel and resources, it renders inter-centre collaboration difficult, with little standardization in place, and the design of multicentre clinical trials to study TBI becomes difficult.

Information on different TBI techniques in the world is sampled from three recent surveys: the mentioned Canadian survey of 12 centres likely representing all of Canadian TBI [56]; the mentioned European survey of 56 centres located in 19 European countries as well as Australia, Israel, Saudi Arabia, and Tunisia [57]; and an informal survey of 62 centres with about half of the responses from the USA, with the rest throughout the rest of the world (reflecting some double-responses between this survey and the first two) [58].

The most common TBI prescription around the world is 12 Gy in 6 fractions. The European survey focused on myeloablative transplantation only and found a total dose range from 8 Gy (in 1 fraction) to 14.4 Gy (in 8 fractions). The Canadian survey included TBI for all purposes, including doses of 2 Gy (in 1 fraction) up to 13.5 Gy (in 8 fractions), as well as unspecified fractionation schedules tabulated as “other”. The dose rate range for most centres is below 20 cGy per minute, although some European countries report up to 37.5 cGy per minute and some Canadian centres up to 50 cGy per minute. Lung shielding is common practice, being reported by 47 out of 56 centres in the European survey, 11 out of 12 centres in the Canadian survey, and 41 out of 59 respondents in the informal survey, although the degree of shielding varies substantially. A small number of centres use chest wall compensation with either electrons, photons, or both, to avoid underdosing the tissue anterior to the lungs. Some other organs are infrequently shielded as well, including the kidneys, liver, heart, eye lenses, and thyroid gland.

The apparatus involved in each technique varies widely as well. Most centres use linear accelerators (51 out of 56 centres in the European survey, 10 out

of 12 responses in the Canadian survey, and 55 out of 61 responses in the informal survey) with 6 MV beam energies being used in more than half of centres, and other energies ranging up to 25 MV. The other centres use Cobalt-60 techniques. More than half of centres use two fields per fraction in parallel-opposed pair (POP) techniques, with either anterior-posterior fields or bilateral fields, with other infrequent techniques including moving treatment beds, multiple SSDs in a given fraction, field Junctioning, helical tomotherapy (HT), volumetric modulated arc therapy (VMAT), and other individualized approaches. Bolus use varies from large amounts of bolus placed around the body to no bolus at all, or used only in small amounts in areas with small amounts of scatter such as the neck and legs. For in-vivo dosimetry, semiconductors are most popular in Europe (37 out of 56 centers), while the remaining European sites and the Canadian survey show a mix of semiconductors, MOSFETs, OSLDs, TLDs, and ion chambers.

3.2.3 Advances in conventional TBI

This section will present some recent research and development in traditional TBI techniques, and samples the innovation involved in designing them.

Various techniques are used in TBI to ensure that the entire patient fits within a radiation beam. The VCC technique, using a sweeping-beam Cobalt-60 source, is described as it was first implemented over 23 years ago by Hussein and El-Khatib [59]. Minor changes have been made to our technique since then, described in detail in its current form in section 3.3. Another Canadian Cobalt-60 TBI technique has been described at McGill University [60], where the larger SSD (220 cm) is used to irradiate the full patient without sweeping. This Cobalt unit was installed in the same room as a 10 MV linac that was used for other specialized, less frequent procedures to optimize the use of clinical space. This technique was decommissioned in 2015.

Many of the studies described in this chapter use parallel-opposed pair (POP) treatments where the patient lies supine and then prone, with the gantry at 0 degrees. Other centres use gantry angles of 90 or 270 degrees with the patient positioned either lying down or sitting. These treatment designs allow SSDs to reach up to 400 cm [61–63] to ensure complete coverage of the patient and a sufficiently

low dose rate, with one group reporting SSDs of 480 cm [64] or higher. Several other centres position the patient in the beam by having them stand rather than sit or lie down [65, 66].

Rather than using a moving source or a very large SSD to cover the entire patient, the patient can also be moved through a fixed beam on a translating couch [67–70]. One group has described attaching a tray table above a translating couch that can also move, to ensure appropriate positioning of lead lung shield penumbras while the patient is moving underneath [67]. Using a variable rather than constant couch velocity offers improvements in dose homogeneity [68]. A recent report from the Tom Baker Cancer Centre in Calgary describes the use of continuously moving MLC leaves in the direction of the patient motion with a fixed aperture width in the lateral direction of the patient, offering further improvements in dose homogeneity with a 15% decrease in lung dose and a reduction of the lateral body edge dose, from 20% over prescription to a 3% variation from prescription [69]. The dynamic MLCs render it unnecessary to produce patient-specific organ compensators, removing a step from the clinical workflow.

Moving the patient during a treatment requires the use of specialized equipment. There are other reports presenting TBI techniques that use equipment already available in most clinics, without needing to reinstall or recommission existing units or requiring very large treatment vaults, offering ways to implement new TBI programs with minimal disruption to the clinic. For example, one paper describes a POP technique with the gantry angle at 270 degrees and a seated patient. Cerrobend lung compensators are used during only one of the treatment fractions, and the only beam modulation required are two discrete adjustments to the collimator jaw setting during each fraction. The technique still gives acceptable dose homogeneity with a simple setup [63]. Another reported technique is arc-based where the gantry sweeps out a 100 degree angle while the patient lies supine or prone, feasible at any clinic using linear accelerators with flattening filters and arc rotation features. This strategy has been shown to be effective for patients up to 30 cm in thickness, and includes in-vivo dosimetry with nine semiconductors and an ion chamber [71].

A field-in-field IMRT forward-planning approach has been presented, using an 18 MV linac at 380 cm SSD. In this technique, reduced-weight fields are used in

planning to reduce dose in what would otherwise be higher-dose regions in the body. This technique does not require compensators or bolus, as homogeneity is achieved using the IMRT subfields [72]. Inverse planning has been proposed for TBI as well, using a modulated-arc TBI delivery system and cerrobend lung compensators. Using PinnacleTM (Philips Medical Systems, Andover, MA, USA), body and lung contours are produced for each patient, and the shapes of the lung compensators are imported to Pinnacle and placed above the patient for the dose calculations [73]. Most modern linear accelerators would be capable of using this inverse-planned technique in a standard sized vault, and it shows improved homogeneity over comparable forward-planning techniques. An interesting point is that the dose rate is restricted to 50 MU per minute in any beams that pass through the lungs (corresponding to a 10 cGy per minute dose rate), with respect to the earlier discussion of dose rate in TBI, while all other beams are delivered at 300 MU per minute.

Two further technical details are worth describing. First, beam spoilers are often used in linac-based TBI methods [61, 62, 64, 68, 72]. These are used to intentionally introduce electron contamination to reduce the depth of maximum dose in TBI treatments, to eliminate the amount of skin sparing that is typical of high-energy X-rays. Typically, these spoilers are on the order of one centimeter thick, made out of acrylic material, and positioned relatively close to the beam head, within around 30 cm. Second, some TBI techniques collect full body CT scans in their planning pipelines [71–73]. In these cases, it is often necessary due to the scan length capacity of CT scanners to collect two separate image volumes and then concatenate them manually in the treatment planning system. This can introduce registration error in the area of overlap, although the overlap region is typically selected in the region of the thigh, away from critical organs at risk.

Two more studies are included in this section to further demonstrate the range of creativity in TBI planning. A South Korean group, in a 2017 proof-of-concept study, reported using custom-designed compensators for a bilateral beam TBI treatment where the patient-specific compensators would be designed by 3D printing moulds and pouring Cerrobend into them, based on 3D optical scanning of the patients [74]. These compensators of variable thickness can accommodate for variations in patient thickness and would also allow for planning to be completed

without requiring CT scans. The technique does not presently account for tissue heterogeneity in the body, but could be adapted for this purpose in future studies.

Finally, an American group in 2016 considered using protons for TBI in a recent theoretical study [75]. Conventional proton therapy takes advantage of the Bragg peak, an effect where massive charged particles deposit most of their energy in tissue at a very narrow and well-defined depth compared to photons and electrons, offering better sparing of normal tissues surrounding the target volume. Leading up to the Bragg peak is a broad-slow-rising dose deposition curve, which currently serves no clinical purpose. The report suggests using an SSD of seven metres to contain a patient of thickness up to 29 g/cm^2 entirely within this broad-slow-rising region. Feasibility was shown with both phantom measurements and Monte Carlo measurements of a patient CT dataset at 250 MeV, 275 MeV and 300 MeV. This technique would not require beam spoilers or patient-specific compensation, as long as a double scattering system was used to produce the necessary large field size. To cite the paper directly, “to design a proton system just to make TBI treatment easier would not be economically wise”, although this approach illustrates the extent of TBI innovation in the literature.

3.2.4 Toxicities

Many studies have been published with toxicity data for treatments that include TBI. For several reasons, it is difficult to speak directly about the toxicities associated with TBI. First, TBI delivery does not occur in isolation as its own treatment technique in modern practice; rather, it precedes a bone marrow transplant, and is typically accompanied by chemotherapy. As a result, toxicities thought to be caused by TBI could be attributed, either in part or in full, to these other concurrent treatments. Second, TBI patients have typically received complex care plans in years leading up to a TBI treatment, either from their current or previous disease, which may contribute to toxicities as well. Third, with the broad diversity of TBI techniques used across the world, it is difficult to compare similar patients receiving similar treatments from different centres to a high degree of precision. That being said, it remains useful to examine toxicity findings on a clinic-by-clinic basis for consistencies, and some studies are able to produce aggregate data for

several centres.

The toxicities of most concern from TBI are the late effects, rather than the acute effects. A study of acute effects in 162 patients tracked and followed the acute toxicities of TBI patients, evaluating them prior to each radiotherapy fraction of a 12 Gy in 6 fraction protocol where the lung dose was limited to 10 Gy [76]. Nausea and vomiting were the most common conditions that patients complained of, in 42.6% and 22.8% of patients, respectively. Typically, a prophylactic treatment for gastrointestinal reactions is given to patients to mitigate these effects. Skin reactions including erythema were also reported in 41.4% of patients, as well as fatigue in 49.2% of female patients and 28.3% of male patients. Overall, in terms of acute toxicities, TBI is well-tolerated.

Of the late effects, lung toxicity is the most concerning toxicity from TBI. Interstitial pneumonitis is a known risk from administering TBI, and as described earlier, most centres implement lung shielding to prevent this. While many centres maintain a low dose rate to the lungs to prevent lung toxicity, there is conflicting evidence as to whether or not this is a relevant precaution with fractionated TBI protocols [47, 48]. Incidence rates of interstitial pneumonitis have been reported as 11% without lung shielding or 2.3% with lung shielding in a study of 12 Gy in 6 fractions [47], 14.3% for patients receiving over 9.4 Gy to the lung and 3.8% receiving less than 9.4 Gy to the lung in a 10 Gy in with three fractions delivered once per day [77], and 33% in a study of 101 patients receiving 13.5 Gy in 9 fractions [78]. In the latter study, survival at one year post-transplant was 28% for patients who had severe lung toxicities, and 81% for those who did not. The studies also suggested that allogeneic transplants have a higher risk of lethal pulmonary complications [77] and that prior chemotherapy is a risk factor [78]. In a study of pediatric patients, there was a reported rate of 23.3% for interstitial pneumonitis in a cohort of 129 patients receiving no more than 10 Gy to the lungs in TBI prescriptions of 10.5-14 Gy [79]. Another study of both pediatric and adult patients receiving either 11 Gy or 12 Gy to the lungs in a 12 Gy TBI dose saw that decreasing the lung dose reduced the rate of pneumonitis from 22.2% to 8.5% across the whole cohort of 257 patients; in the subset of 40 pediatric patients, the rate lowered from 25% at 12 Gy to 4.2% at 11 Gy [80]. Because it is not possible to determine by a biopsy if the pneumonitis is radiation-induced or infectious, it

would not be prudent to state that TBI is the only cause of these toxicities, although the statistical association warrants caution nonetheless.

The kidneys are another OAR during TBI, with some centres administering kidney shields in addition to more common lung shields. One study uses both CT and ultrasound to design the fabrication of these shields in an anterior-posterior POP technique [81]. A single-centre study of a pediatric TBI cohort of 92 patients found only one patient with unresolved renal dysfunction at one year after the transplant, with 28% of patients experiencing renal dysfunction that resolved within months of onset [82]. In this study, they limited the kidney dose to 10 Gy for patients with a history of renal dysfunction, but the patients otherwise had treatments of 11.1 Gy or 12 Gy. One meta-analysis found that there was only a kidney dose-response function for adult populations, but no similar response for pediatric populations [83]. Another meta-analysis found a threshold biologically effective dose of 16 Gy for renal toxicities, which would be lower than the 21.2 Gy biologically effective dose of a standard 12 Gy in 6 fraction scheme, although the age of the patients in the reviewed studies was not specified [84].

Cataractogenesis is also seen following TBI treatments, and like the kidneys, a small number of centres also use eye shields for patients to prevent this risk. The same meta-analysis that previously found a threshold dose for renal toxicity also suggests a biologically effective dose threshold of 40 Gy to the eyes, which is not exceeded in fractionated dose schemes [84]. An earlier meta-analysis of 1,063 European TBI patients with acute leukemia saw a 60% risk of cataract development at 10 years in patients who received a single dose and 43% in patients receiving a fractionated scheme [85, 86]. The use of eye shields is considered controversial as the eyes are sanctuary sites from chemotherapy, and their use can result in cylindrical areas of underdosage in the brain behind the eyes, leading to higher chances of relapse. One study aimed to determine if this risk could be observed, and studied a pediatric cohort of 188 children receiving TBI where 139 had eye shields and 49 did not [87]. The incidence rate of cataracts was 90% without shielding and 31% with shielding, and when they did develop, patients with eye shielding developed them at a longer time after treatment and with less severity. Two patients with eye shielding relapsed, but this small proportion did not suggest that eye shielding alone increases the risk of relapse. A recent multi-centre trial found that for

patients under three years of age receiving allogeneic transplants, whether or not TBI was included in the conditioning regimen was an independent risk factor for developing cataracts [88].

Pediatric patients make up a significant portion of TBI treatments and several studies have focused on this patient population. A 2005 study of 42 children receiving 9.9 Gy in 3 fractions with a median 5.7 years of follow-up found that 78% of patients developed cataracts, 12% developed hypothyroidism and 14% developed thyroid carcinoma [89]. For patients treated under three years of age, 29% of patients developed an osteochondroma (a benign bone tumour) at a median follow-up of 9.2 years, some of which required surgical removal. 74% of patients had some restrictive pulmonary toxicity but only 45% of patients continue to experience mild problems. Overall, while some late effects from the treatment could present as late as 10 years after treatment, these symptoms rarely affect quality of life significantly. Follow-up is necessary for these patients for family planning purposes as testicular and ovarian dysfunction had been noted as well. Another study of 62 pediatric patients receiving autologous bone marrow transplants at 12 years of follow-up, 30 without TBI and 32 with TBI, found an overall higher rate of toxicity in conditioning with TBI compared to conditioning without TBI [90]. A main toxicity noticed was growth delay, and hormone deficiencies were a concern as well. Growth hormone treatment may be beneficial in the post-transplant care plan for these patients. Secondary cancers were also more common in the TBI arm of the trial with six malignant tumours as well as eight benign tumours, appearing while the non-TBI arm saw only one patient develop leukemia. The previously discussed multi-centre trial for patients under three years of age found, across 717 patients, that the most common late effects were growth disturbance, cataracts, and hypothyroidism, and also suggests annual thyroid palpitation and earlier mammogram screening for females in the long-term care plans [88].

Another OAR that is not as frequently discussed in the context of TBI are the breasts for female patients. Based on long-term follow-up data from Seattle, 3,337 female survivors of bone marrow transplant procedures were studied, and it was found that the cumulative incidence of breast cancer at 25 year follow-up was 11.0%, although this figure is 3% for patients who did not receive TBI while it is 17% for patients who did receive it as part of their transplant [91].

3.2.5 Helical tomotherapy and VMAT

As more sophisticated beam modulation techniques have been developed, more conformal treatment options have been devised for TBI. The two main alternatives to the previously described POP techniques are helical tomotherapy (HT) and volumetric modulated arc therapy (VMAT). Full descriptions of these techniques can be found elsewhere; in short, HT involves a couch translation while the gantry fully rotates around the patient [92], while VMAT uses an optimization technique to produce multiple treatment arcs with continuously changing gantry rotation speeds, MLC patterns, and other settings [93].

An early feasibility study of using HT for TBI investigated the effects of several treatment parameters on treatment planning [94]. Smaller field sizes resulted in improved dose homogeneity, but also increased treatment times. Greater amounts of MLC modulation also resulted in longer treatments, but lead to lower doses to critical organs. Treatment planning with HT resulted in a dose reduction to critical organs by 35-70% of the prescription dose, including lungs, eyes, heart, liver, and kidneys, without the need for special blocks or other equipment during treatment. Additionally, megavoltage CT (MVCT) images were collected for positioning. It was found that using a limited MVCT approach would reduce the target localization time by 60%, instead of using an MVCT of the whole body. Depending on the treatment parameters selected, treatment times were in the range of 16-31 minutes per fraction for an anthropomorphic phantom.

Another feasibility study of TBI with HT directly compared HT plans to extended SSD treatment plans on four sets of patient CT data [95]. The HT plans treated the upper body with an HT technique and used a standard, nominal SSD treatment for the lower limbs. The extended SSD plans included an electron boost treatment. In this study, each treatment took about 4 hours to plan, including an hour to produce lung shields and compensators for the extended SSD treatment. The lung median doses were 5.4 Gy for HT plans and 8.34 Gy and 8.95 Gy for extended SSD plans (left and right lung, respectively). The mean dose delivered to the PTV was 12.3 Gy using HT plans and 10.3 Gy for the conventional TBI plans. The total beam-on time was longer for the planned HT deliveries, around 15.4 minutes per fraction, compared to 11.1 minutes per fraction for extended SSD

treatments, but offers superior dose homogeneity and lung sparing.

Another group has described an HT TBI technique using MVCT for both patient positioning and dose reconstruction [96], and reported treating four patients with this technique [97]. For each fraction, MVCT images were collected and deformed to the planning CT image with a deformable registration. Planned and delivered doses, as measured by the TPS calculations and the MVCT reconstructions respectively, differed by 2.7% at most. The beam-on time per fraction was between 19 and 23 minutes, not including time for MVCT data collection, intra-fraction contouring, or analysis between fractions. Another group studied how to optimize the amount of time required to collect MVCT images for patient positioning while maintaining an acceptable quality of the data, using three cadavers as imaging subjects [98]. Scan times ranged from 4 to 16 minutes per MVCT depending on the couch speed used (1 mm/s to 4 mm/s). An iterative reconstruction algorithm allowed for faster couch speeds, and hence shorter scan times, that produced images of acceptable quality for patient setup. This was at a cost of much higher computational times over a filtered back projection algorithm.

Another study focused on defining appropriate target volumes in HT TBI and examined the impact of positioning errors on treatment as measured in a TPS [99]. They examined three PTVs: one equal to the external body contour, one with a 5 mm air margin outside the patient to account for patient motion during treatments (similar to [95]), and one with a 5 mm margin trimmed into the patient to exclude the skin and restrict the skin dose (similar to [100]). They determined that setup errors up to 5 mm provided clinically acceptable dosimetric results, and that designing plans with PTVs including air margins were more vulnerable to larger setup errors. Given this, the authors reason that it is better to emphasize strict patient immobilization rather than including an air contour in HT planning to accommodate for patient movement.

An initial study of HT TBI on a cohort of 10 pediatric patients was carried out, with these patients being suitable for an HT trial due to their small size [101]. For larger patients, several reports describe needing two CT scans for planning treatments that use HT or VMAT for the whole body, due to the limited length of a single CT scan [101, 102]. In these cases, the patient is rotated 180 degrees during treatment between the fields planned on the upper or lower body. For this pediatric

study, patients smaller than 145 cm in height could be treated in 17 minutes of beam-on time per fraction, while patients who needed to be rotated and treated in two positions required up to 34 minutes of beam-on time per fraction. MVCT was also used for patient setup. The pediatric patients required strict immobilization, including sedation or anesthesia despite the twice-daily treatments, due to long treatment times in a single position as well as claustrophobia and loud noises in the unit.

Some clinical trials have been undertaken using HT techniques for TBI. One group treated four AML patients, finding improved critical organ sparing with lung doses of approximately 7 Gy and kidney doses of approximately 8 Gy from a 12 Gy in 6 fraction prescription [97]. The team also noted the benefit of not having to produce compensators or other cumbersome procedures. The main toxicity reported was low-grade dermatitis. Two patients live disease free at most recent follow-up and two patients succumbed to GvHD, but had no signs of disease at death. Another clinic using HT for TBI treatments reported a unique skin reaction in a band at the level of the femur in four out of twelve patients, arising one to two months after the stem cell transplant [103]. The region coincides with the field junction between upper body and lower body treatments where the fields overlap to 24 Gy over 6 fractions, which had been designed to ensure that no part of the target was missed. The lesions were improved within a week by applying moisturizing agents.

TBI techniques using VMAT have also been explored. One issue with HT is the requirement for long beam-on times. A 2015 paper planned a 12 Gy in 10 fraction treatment using RapidArc (Varian Medical Systems, Palo Alto, CA, USA) which would only take 7.2 minutes of beam-on time per fraction, compared to HT which can reach over half an hour [100]. This issue of long beam-on times was of particular concern due to a lack of clinical resources in the country of origin of the paper where beam-on time is valuable. By using six arc fields in VMAT plans with 177 control points each, taking five hours of planning time, the study team reached mean organ doses of 8.6 Gy to lung and 9.9 Gy to kidneys while ensuring 95% of the PTV received the prescription dose. This also eliminated the need for an electron chest wall boost and demonstrated the feasibility of using VMAT for TBI in this setting.

A clinical trial using VMAT TBI treated seven leukemia patients between July 2013 and July 2014 with 13.2 Gy in 8 fractions at 6 MV [102]. They used 8 VMAT segments, requiring a 180 degree patient rotation halfway through the treatment. The fractions each took 1.5-2 hours to execute due to extensive positioning requirements, and each treatment required 40-45 hours of planning time with the currently available computational resources. The optimizer was steered towards lung sparing by placing helping structures inside the lung as necessary. A full body elastic gel bolus as well as a thermoplastic mask were used. While doses were reduced to critical organs effectively, the increasing planning time could be a burden, but for this centre, the alternative for the patients would have been to travel to other more distant centres. There was a very low rate of early toxicities and five of the seven patients are disease-free at short-term follow-up.

An issue with HT or VMAT is the possibility that circulating malignant cells will not be completely irradiated, as the whole body is never being irradiated simultaneously as for POP techniques with large field sizes. A 2010 study of TBI used stochastic and deterministic modelling to investigate this issue, treating blood perfusion in the body as a sinusoid with a peak-to-peak displacement equal to the height of a standard adult patient [104]. It was determined that TBI is not likely to be prone to this issue.

Two further studies have made progress in clinical implementation of a VMAT TBI technique. One recent study describes a novel rotating immobilization system, allowing for the 90 degree rotation of a patient between an upper body VMAT treatment at standard SSD in three arcs and a lower body treatment of two or three pairs of anterior-posterior fields [105]. This reduces the chances of error due to patient positioning as only one setup is required at the beginning of the VMAT treatment. Compared to their previous standing POP technique with a linac at 550 cm, the mean dose to the body increased from 11.5 Gy to 12.8 Gy in changing from a conventional technique to VMAT, and the mean dose to the lungs decreased from 8.8 Gy to 7.9 Gy. The treatment was determined to be robust to positioning uncertainties of 5 mm. Another study has described how to use a clinically available diode array, ArcCHECKTM (Sun Nuclear Inc, Melbourne, FL, USA), to perform quality assurance (QA) of field junctioning in the context of VMAT TBI with multiple arcs, recognizing the trend towards these conformal TBI treatments

and a growing need for suitable QA tools [106].

3.2.6 Total marrow irradiation and total lymphatic irradiation

It has been acknowledged that a different conditioning radiotherapy technique, total marrow irradiation (TMI), is naturally suited for VMAT treatment planning. This treatment targets only bones with substantial red bone marrow content in the patient rather than treating the whole body. On the same line of thought, total lymphatic irradiation (TLI) has surfaced where only the lymphatic system is treated, as well as total marrow and lymphatic irradiation (TMLI) where the PTV is the sum of the TLI and TMI PTVs. Other papers discuss combining a standard TBI treatment with a TMI boost to treat the entire body with additional dose only to bones, allowing for dose escalation beyond the traditional 12 Gy prescription to minimize the chance of relapse without increasing the dose to critical organs, leading to improved outcomes without increased rates of toxicities.

TMI target volumes include the marrow-containing skeleton, such as the upper extremities, pelvic bones, and thoracic bones. A group at the City of Hope National Medical Centre in Duarte, California has published several reports regarding both TMI and TMLI using an HT technique, and had treated 120 patients with TMLI as of 2012 [107]. An earlier feasibility study in 2007 showed that TMI patients received 7.2 Gy or less to 84% of the lung volume while maintaining TBI-equivalent doses elsewhere in the body [108]. MVCTs are used for positioning, and different planning CTs are taken during shallow breathing, inspiration, and expiration to determine margins for the ribs [109]. The contouring process, including contouring OARs, took up to 8 hours for TMI plans and 12-16 hours for TMLI plans in these initial studies. The lower extremities are treated with an anterior-posterior POP treatment junctioned with the HT plan [108, 110]. A study was also undertaken using VMAT planning with eight arcs and found similar TMLI dose conformity with only 10.5 minutes of beam-on time compared to 18.7 minutes of beam-on time for HT, although the VMAT plan required more patient positioning and setup time [111]. One risk of using TMLI had been that by delivering less dose to the whole body, there was a higher chance of extramedullary relapse (that is, relapse of the disease outside of the bone marrow region), but a retrospective study from

this clinic found there was no higher risk of extramedullary relapse compared to conventional TBI [107], using dose escalation up to 15 Gy. Most recently, a 2017 paper from City of Hope describes a clinical trial of VMAT TMLI to treat 51 patients with relapsed or refractory acute leukemia, using several dose escalation levels between 12 Gy and 20 Gy [112]. For prescriptions above 13.5 Gy, the brain and liver doses were limited to 12 Gy. The overall survival at one year was 55.5% with 88% of patients in complete remission at 30 days, including 100% of the patients treated at 20 Gy. Non-relapse mortality rates were 3.9% at 100 days and 8.1% at one year. Overall, the trial was well-tolerated and a phase II clinical trial is now in progress.

A group in Minneapolis has extensive TMI experience as well, using an HT technique for the full body. A feasibility study was included in a previously mentioned work that also considered HT for TBI [94]. For TMI, this required a total of 31 minutes of beam-on time, and 70 minutes of treatment time total in a first patient experience including 10-15 minutes of MVCT collection time [108]. Breathing motion was accommodated for by adding a 1 cm margin around the CTV. A dose escalation study published ten years later [113] found that escalation to 15 Gy with TMI was feasible, while escalation to 18 Gy saw three out of six patients succumbing to treatment-related mortality. A technical issue called the thread effect can arise in TMI due to helical field junctioning, which can manifest as a dose inhomogeneity in peripheral doses away from the PTV in the shape of a ripple [114]. The group found that the DVH parameters of the bones of the upper arms were influenced by this, but this could be remedied by using different couch pitch values and the dose to the whole PTV was not significantly affected.

Using TMI as a boost in addition to TBI has been performed in one clinic by delivering 2 Gy in TMI on the day after a standard 12 Gy in 6 fractions delivered twice-daily [115]. Anticipating dosimetry challenges at the field junction region, they chose the level of the knees for the field junction where there is no bone marrow present. A 4 mm margin was added to all of the bones in an isotropic expansion in planning. Beam-on time ranged from 24 to 35 minutes for the TMI fraction.

In efforts to decrease the time resources required for TMI planning, one study found that a treatment planning system called Voxel-Less OptimizationTM (Accu-

ray Inc, Sunnyvale, CA, USA) could plan and optimize TMI plans over four times more quickly than Eclipse [116], while an international multi-centre study has evaluated the use of 2D tomograms for patient positioning instead of full MVCTs which can be produced in less than a minute instead of the usual ten to fifteen minutes [117].

3.2.7 Treatment planning systems and in-vivo dosimetry

Commercially available treatment planning systems (TPSs) such as EclipseTM (Varian Medical Systems, Palo Alto, CA, USA) or Pinnacle are able to perform dose calculations given a set of beam configurations and a patient CT image. These dose calculations are usually designed for treatments delivered within a standard SSD range and have known limitations even within this range, particularly for tissue inhomogeneities and surface doses. At extended SSD, these calculations may become even less accurate, and precautions must be taken before making clinical decisions based on the output of a TPS calculation for TBI. This also emphasizes the need for in-vivo dosimetry for quality assurance (QA) purposes.

One comparison of TPS approaches for TBI planning was made by a group in Quebec, using different options in Pinnacle to determine the most accurate calculation model despite the above challenges [118]. The TBI technique is a moving couch technique with variable couch velocity. Two different beam commissioning approaches were studied, one using default settings and the other using a TBI-specific beam model in Pinnacle that incorporates features such as large field size and extended SSD. Two different dose calculation algorithms, a 3D pencil beam algorithm and a superposition-convolution algorithm, were used, and TPS doses were compared to ion chamber measurements. Except for the build-up region and at depths beyond 20 cm, where errors were as high as 27% at some points, the maximum discrepancy was 2% between TPS and measurement, using the TBI-specific beam model in Pinnacle and the superposition-convolution algorithm. A correction factor was determined and applied which brought this error down to -0.68%.

As mentioned before, several in-vivo dosimetry techniques have been applied to TBI. One group with a translating couch TBI technique used MOSFETs on the patient surface to measure entrance and exit doses at several points in the patient

[119]. After the first treatment fraction, if MOSFET readings varied by more than 10% from the prescribed dose, the velocity of the couch is modulated appropriately in the remaining fractions to ensure the total prescription dose is reached. In a retrospective study of 161 patients treated this way, while a few cases saw patients with very large dose differences (over 35% in one region), most discrepancies were resolved in subsequent fractions with the immediate MOSFET feedback. This technique is effective as long as the treatment includes multiple fractions; for example, a similar overdosage in a single 2 Gy fraction treatment would not be able to be compensated.

There are similar retrospective studies in the literature of clinics using semiconductor diodes for in-vivo dosimetry, with two examples being a study in London, UK of 363 patients across three hospitals using bilateral 10 MV beams [120], and another in Melbourne, Australia of 86 patients treated with either an 18 MV technique or a combined 6 MV and 18 MV technique with bilateral beams [121]. The advantage of dosimetry using semiconductors includes being able to use several dosimeters at a time with one electrometer system, immediate readout for analysis during treatment fractions allowing for treatment adjustment if needed, and reusability of equipment, although they must be calibrated in TBI conditions, including but not limited to a low dose rate. The Australian study found a consistent discrepancy where the TPS overestimated the TBI doses by about 5% over seven years of patient data, for prescriptions of either 12 Gy or 13.2 Gy to whole body, with the worst agreement in the lung.

Another group compared TPS calculations to dosimetry results, using the collapsed cone convolution (CCC) algorithm in Pinnacle and alanine dosimeters which make up part of their routine TBI treatments, in an anthropomorphic phantom at 400 cm SSD and 18 MV [66]. Alanine dosimeters use a spectroscopy technique where the brightness of a central line of the spectrum from the dosimeter is proportional to the dose delivered. Pinnacle gave doses lower than the alanine dosimeters, 2% lower throughout the body axis and 3% lower in the lung region. While a small difference, this can and should be accounted for. TLDs and MOSFETs have also been used in combination to compare dose calculations of the XiOTM planning system (CMS, St. Louis, MO, USA), using either fast-Fourier transform convolution or multigrid superposition algorithms [62], which would be expected to face

similar challenges as other TPS calculations for TBI. Deviations between physical dosimeters and the TPS were found in the lung region, although the data collected from this dosimetry experiment allowed for a conversion factor to be determined for lung dose in treatment planning.

Similarly, the field-in-field technique described earlier compared MOSFET readings to calculations in Eclipse with pencil beam convolution and Batho in-homogeneity corrections [72]. MOSFET readings were 4-5.5% higher than TPS calculations for the lungs and shoulder regions. Further studies of TBI calculations in Eclipse comparing the analytic anisotropic algorithm (AAA) and AcurosTM algorithm found that while the relative doses given by two treatment planning algorithms in Eclipse were accurate at 400 cm SSD, absolute dose was sometimes wrong in the TPS by over 10% compared to ion chamber measurements in both homogeneous and heterogeneous phantoms, reinforcing the fact that while TPS calculations may assist in TBI treatment planning, they cannot be the only method of dose calculation [122].

A recent report demonstrates the use of OSLDs for TBI dosimetry [123]. OSLDs are convenient dosimeters, although they are calibrated at standard dose rates of 6 Gy per minute rather than the low dose rates customary for TBI. It was shown that OSLDs can still be used for TBI purposes as they show negligible differences in sensitivity between these irradiation conditions, and that the OSLDs simply need to be pre-irradiated to work around a known short-term signal fading effect. A correction table is provided to compare readings between standard conditions and TBI conditions for up to 7 days following OSLD irradiation, along with other practical considerations.

3.2.8 Monte Carlo dosimetry

Monte Carlo (MC) dosimetry is the gold standard for dosimetry in radiotherapy, described in detail in Chapter 4, but is not routinely applied to TBI. This is for several reasons, including complicated treatment configurations with custom-designed compensators resting away from the patient, difficulty in accounting for beam spoilers or flattening filters, a lack of complete CT imaging in clinical protocols, difficulty in modelling treatment sources, challenges in simulating a moving pa-

tient or source, and perhaps most importantly, insufficient computational resources to handle the large number of histories required to reach acceptably low statistical uncertainties in very large phantoms.

One group produced a MC simulation of a static Cobalt-60 beam using a custom-designed MC code written in the C programming language, attempting to simplify the simulation to reach appropriate computation times [124]. The simulations were about ten times more efficient compared to a similar simulation in GEANT4 (a widely used set of MC codes from CERN), with results agreeing within 2%. Dose distributions in an anthropomorphic phantom and beam profiles in a water phantom showed good agreement between simulation and measurement, although the method requires refining before it can be applied to patients for routine use. In the theoretical paper described earlier using protons for a TBI treatment, these calculations were also done with Monte Carlo simulations in GEANT4, but here the focus of the work was on the feasibility of a new treatment design and not on the dosimetry of currently used techniques [75].

A Canadian group treating TBI patients with a static Cobalt-60 beam has recently used MC simulations to design patient-specific compensators [125]. Without organ dose compensators, doses in the MC simulations were strongly inhomogeneous with doses ranging from -5% to +25% of the prescription dose, with notable differences in the neck and lung regions. A deformable registration tool, VelocityAI™ (Varian Medical Systems, Palo Alto, CA, USA), was used to deform the prone dose distribution to the supine image and add the two distributions together. Based on this distribution produced without compensators, a new compensator of variable thickness was designed for the supine and prone treatments of one patient on a voxel-by-voxel basis to reduce the doses to prescription level. Such compensators have not yet been physically constructed, but the authors consider that they could be 3D printed. Only one patient was shown in this conceptual study and dose-volume information is not reported. The disadvantage to this technique is the requirement to run two sets of simulations for each patient, one with and one without the compensators.

A group in Sweden produced two papers, in 2013 and 2014, describing a MC approach to studying TBI [64, 126]. Their TBI technique uses a 15 MV linac with bilateral beams at an SSD of 460 cm, where the patient couch is rotated 180

degrees between treatments, obviating the need for repositioning or a second planning image. Compensators are used to improve dose homogeneity and the arms are positioned in such a way to assist in the reduction of lung dose. Dose profiles were produced for five patients with MC calculations, with the results of two simulations presented to illustrate improvements in dose homogeneity with the use of compensators. Dose-volume information for individual organs is not presented. The 2014 paper is technically focused and employs these MC techniques to determine what the optical thickness of a beam spoiler should be, as well as the most appropriate source-to-spoiler distance, with respect to TBI beam characteristics and superficial dose.

A report described earlier of a novel positioning scheme for a VMAT TBI technique reports preliminary Monte Carlo organ doses and DVHs [105]. While it is clear that the team has achieved Monte Carlo dosimetry of their pre-existing POP technique with organ compensators, comprehensive organ doses were not described as the focus of the report was the new positioning technique.

Finally, a 1988 textbook written by pioneers in the application of MC techniques to medical physics describes an initial MC simulation of TBI from a Cobalt-60 source [127]. 5,000 histories per voxel of a phantom of approximately 30,000 voxels were simulated, which took about 30 hours. The phantom included only thoracic slices that also included lung tissue. The measurements were relative only, and showed that doses in the lung and at the sides of the body were more than 120% of the dose at the center of the thorax. These results remain valid and, viewed together with the results presented in Chapter 5 of this thesis, elegantly demonstrate 30 years of progress in MC for medical physics.

3.3 TBI at the Vancouver Cancer Centre

The TBI technique in use at the VCC has been in use for at least 23 years, and was updated in 2011 from a film-based planning technique to a CT-based planning technique [59, 128]. The most common prescription at our center is 12 Gy in 6 fractions to the whole body delivered twice daily, with at least six hours between fractions, with other dose prescriptions at our clinic including 13.5 Gy in 9 fractions, 6 Gy in 4 fractions, 4 Gy in 2 fractions, and 2 Gy in 1 fraction. Between 30

and 50 patients are currently treated per year.

A Cobalt-60 unit (Theratron 780C, Atomic Energy of Canada Ltd., Ottawa, Canada) with a head swivel feature is used to sweep a treatment field over the patient at an extended SSD. Each fraction is comprised of two fields, with the patient lying supine for one field and prone for the other. Because of the inverse square loss of radiation intensity with distance, this technique would lead to much larger dose being delivered to the center of the patient, which is closest to the source, compared to the extremities in the superior and inferior directions. To maintain a uniform dose profile across the patient, a PMMA flattening filter is positioned below the treatment head and centered on the beam axis. Additionally, because lung tissue has a lower density than other tissues, the dose delivered would be higher than prescription without any sort of compensation. To maintain the lung dose at prescription levels, lead lung block compensators are designed on a patient-by-patient basis and are placed on a thin plastic tray above the patient. A schematic of the treatment unit is shown in Figure 3.1.

The treatment planning process for each patient begins with a simulation appointment. A CT image volume is taken over the torso of the patient, spanning from a few centimetres below the umbilicus to the level of the neck. This is done for both supine and prone treatment positions. Three treatment marks are made on each side of the patient: one below the umbilicus to mark the beam central axis position (reference mark t0), one at the sternum (reference mark t1), and one at the level of the nipples which represents a point at depth between the lungs (reference mark t2). Reference marks t1 and t2 are used to position the lung compensators in each treatment fraction. Radio-opaque markers are placed on the patient at each mark in each CT image for planning purposes, as shown in Figure 3.2. During patient simulation, the patient SSD is measured in each treatment position. Patients with a lower height may be positioned on styrofoam mats to reduce the SSD, which allows for slightly shorter treatment times due to reduced inverse square losses.

Based on the CT images collected, an oncologist delineates the contours of the lung compensators. With these contours and the measurements collected during simulation, a physicist determines the appropriate thickness for the lung compensators using a ray-tracing program that measures tissue deficits for rays traversing lung tissue through the lung contour from the source position [128]. This procedure

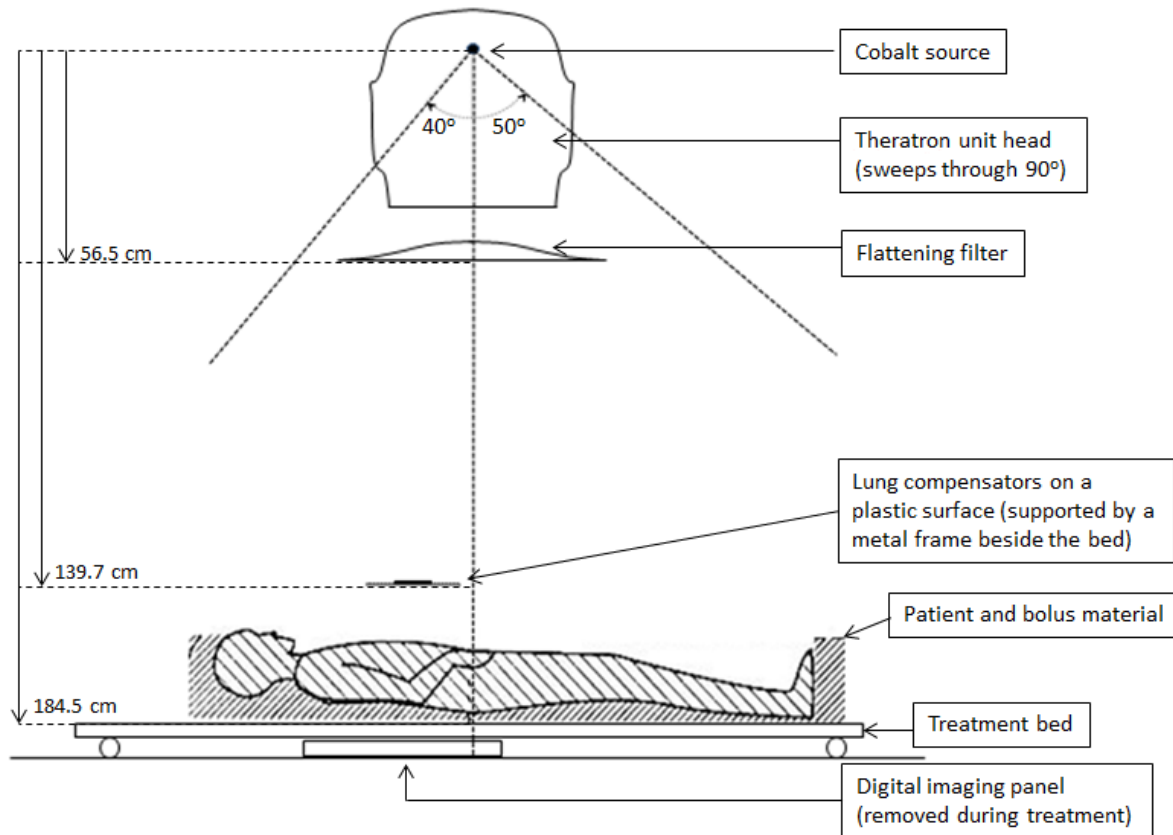
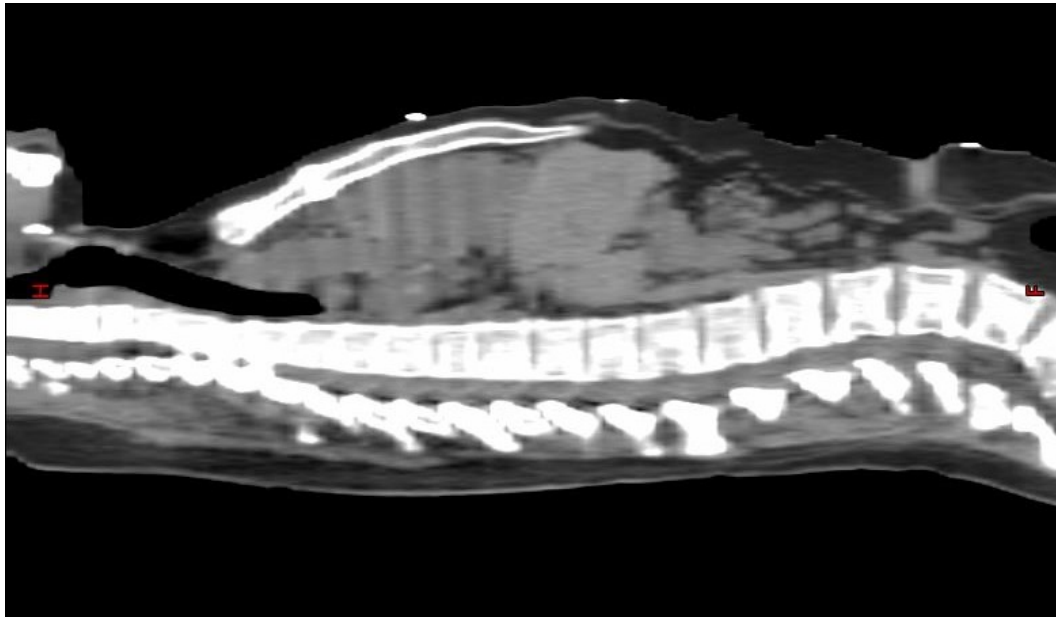


Figure 3.1: Schematic representation of a TBI treatment at the VCC. Patient is shown in the supine position. Labelled distances are drawn to scale, measured from the location of the source.

also produces a MC phantom file for the patient CT which is used and described in Chapter 4. The thickness of the compensators as calculated from the ray-tracing program is rounded up to the next 0.5 mm increment and the compensators are then produced by machinists in our department. Typical thicknesses for compensators range from 1.0 to 3.0 mm.

The treatment time for each field is determined as a function of the measured SSD, the time elapsed between the treatment date and the source installation, and the patient separation (thickness below reference mark t0) measured during simu-



(a)



(b)

Figure 3.2: CT images of a TBI patient, in the (a) supine and (b) prone positions, with three radio-opaque markers visible in each scan at the patient surface (t0, t1, and t2, from right to left).

lation. A reference dose, D_R , is determined based on the prescribed dose per field D_{Tx} and the PDD at mid-separation depth d ,

$$D_R = \frac{D_{Tx}}{\text{PDD}(d, SSD)} \quad (3.1)$$

where the PDD is tabulated for an SSD of 160 cm and corrected with a Mayneord factor for the actual SSD for the treatment.

The dose rate at mid-separation below t_0 , \dot{D}_R , is calculated as

$$\dot{D}_R = I F_{TBI} F_{ISL} \quad (3.2)$$

where F_{TBI} and F_{ISL} are factors accounting for the dose delivered on the beam central axis by a sweeping beam compared to a static beam, and the inverse square losses, respectively. I is an output factor based on the activity of the source on the treatment start date,

$$I = I_o \text{ RDF} \exp\left(-\frac{t \ln 2}{t_{1/2}}\right) \quad (3.3)$$

where $t_{1/2}$ is the half-life of Cobalt-60, 1921.5 days, and t is the time in days elapsed since the last source change. The relative dose factor RDF is a ratio converting the measured intensity at 80 cm and a 10x10 cm² field size to an extended SSD with 35x35 cm² field size as used in TBI. The final treatment time per field is obtained by dividing the reference dose by the dose rate,

$$T_{Tx} = \frac{D_R}{\dot{D}_R}. \quad (3.4)$$

The TBI treatment pipeline was commissioned to deliver a mean body dose within 10% of the prescription dose (e.g. between 10.8-13.2 Gy for a 12 Gy prescription) based on this point dose calculation at patient mid-separation. A semiconductor diode is placed in the beam at 100 cm from the source during treatments for in-vivo dosimetry to ensure that treatments are delivered as planned.

Given the half-life of Cobalt-60 of roughly five years and three months, treatment times double over the five-year clinical lifetime of the source. The previous two source installations at our centre occurred in July 2010 and August 2015. Typical treatment times increase from around 6.5 minutes per field within two months

of a source change to around 13.0 minutes per field within two months prior to a source change. The source replacement cost is on the order of \$300,000.

A medical physicist is present at the first fraction of each treatment. The role of the physicist is to ensure proper positioning of the lung compensators. As shown in Figure 3.1, a digital imaging panel can be placed underneath the treatment bed. With this in place, very short beam exposures are delivered in each treatment position with the lung compensators in place. Based on the images acquired, the lung compensator positions may be adjusted slightly at the discretion of the physicist.

Bolus material is used between the legs, around the head, and between the arms and torso of the patient where possible. This allows for a full scatter dose contribution to all parts of the body. During each treatment, radiation therapists count the number of beam sweeps delivered to the patient. Treatments are only delivered in integer numbers of sweeps which may not necessarily subdivide to contain the entire treatment time. At the final fraction, an additional sweep is added if necessary to reduce the error caused by the discrete number of sweeps compared to the continuously-measured treatment time. There is also a timer error involved in cobalt teletherapy units due to the finite amount of time required for the source to move from its shielding unit to the beam opening during a treatment. For treatments longer than three minutes, which encompasses most TBI treatments at our clinic, 0.72 seconds are subtracted from the treatment time to accommodate for this.

Chapter 4

Monte Carlo dosimetry of the TBI technique in Vancouver

4.1 Introduction to Monte Carlo

4.1.1 History

In 1945, the first electronic computer was completed at the University of Pennsylvania. The Electronic Numerical Integrator and Computer, or ENIAC, was a wartime investment that accelerated routine military calculations. This was one of many key developments leading to the bombing of Hiroshima and Nagasaki and, consequently, the end of the Second World War [129].

Researchers with the Manhattan Project at the Los Alamos Laboratory, including John von Neumann, were invited to see the ENIAC in Philadelphia before the war had ended. Using the capability of the ENIAC to perform calculations that would have been intractable to compute by hand, these researchers were able to design a computational model of a thermonuclear problem, the results of which were presented in 1946. Stanislaw Ulam, a mathematician with a keen interest in random processes, was in the audience and saw clearly the potential of this machine to solve problems by statistical sampling. For instance, to determine the probability of a shuffled deck yielding a successful outcome in a game of solitaire, would it not be better to lay out a hundred games and count the successes, rather than to spend countless hours on combinatorial calculations? [130] Such sampling techniques had been conceived in mathematics before, but had not been pursued due to the tediousness involved in manual calculations.

Ulam and von Neumann soon began collaborating on a statistical technique to study neutron chain reactions that would help predict the explosive behaviours of nuclear weapons that were being designed [130]. Nicholas Metropolis suggested naming this sampling technique Monte Carlo, after the Monte Carlo Casino in Monaco where an uncle of Ulam's often gambled with borrowed money [129]. The first paper describing the MC method was published in 1949 [131], and since then, the technique has been applied in problems across finance, molecular structure, systems biology [132], and most importantly for this report, medical physics, where MC simulations have become the gold standard for dosimetry.

It may seem strange that the machine can simulate the production of a series of random numbers, but this is indeed possible.
 — Metropolis and Ulam, The Monte Carlo Method, 1949 [131]

4.1.2 Monte Carlo simulations in radiation oncology physics

In medical physics, the photon and electron interactions of interest are inherently probabilistic in nature, as explained in Chapter 2. The interaction probabilities, amount of transferred energy, and initial states of created particles depends on the energy of the incident photons and the density and composition of the material being traversed. Random number generators provide a natural way of exploring these processes where analytical calculations would be out of the question, given the complex shapes and compositions of patients and treatment geometries.

An example of how random numbers are useful in medical physics is given by Equation 2.2 representing the number of photons attenuated from a beam traversing a material. The probability distribution of having a photon interact in a slab of thickness dx after travelling distance x is given by

$$p(x)dx = \mu e^{-\mu x}dx. \quad (4.1)$$

The cumulative probability distribution $P(x)$ giving the probability of interacting

at some point between $x = 0$ and a distance x is found by integrating,

$$P(x) = \int p(x)dx \quad (4.2a)$$

$$P(x) = \int_0^x \mu e^{-\mu x'} dx' \quad (4.2b)$$

$$P(x) = 1 - e^{-\mu x} \quad (4.2c)$$

and then, solving for the inverse function gives

$$x = -\frac{1}{\mu} \ln(1 - P(x)) \quad (4.3a)$$

$$x = -\frac{1}{\mu} \ln(R). \quad (4.3b)$$

These equations allow us to sample the distribution of photon distances travelled before interacting. R is a random number between 0 and 1, as this is equivalent to sampling one minus the value and saves a computational step. By substituting random numbers between 0 and 1 for the probability $P(x)$, an appropriate distribution between 0 and ∞ is obtained. This is an example of the transformation method, one type of sampling technique used in MC simulations to make use of uniform distributions of random numbers in physically meaningful ways.

Each particle history in a MC simulation begins with an incident particle. An incident high-energy photon can give rise to many other photons and charged particles which are all tracked as part of the same particle history. Each particle is tracked with a three-dimensional position, a three-dimensional direction of travel, an energy, a particle type, and other flags may be implemented as well to count additional properties (e.g. the number of times the particle has interacted). These coordinates of a high-dimensional phase space are updated incrementally as the tracked particle travels through the treatment geometry as visualized in Figure 4.1. In short, a distance of travel is selected before an interaction occurs, the type of interaction is determined based on the interaction cross-sections (provided the distance travelled did not bring the particle outside the treatment geometry), and the resulting particle types, energies, and directions are determined for each interaction, all of which use the production of random numbers in their calculations. This

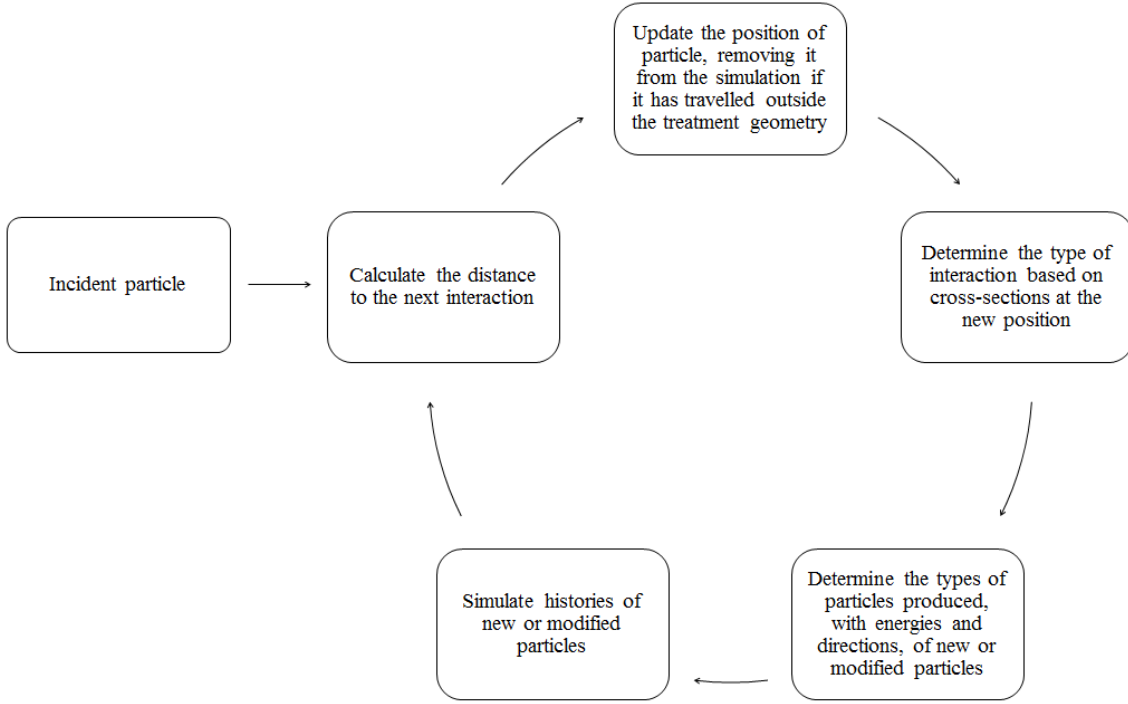


Figure 4.1: Flowchart describing the basic elements of a Monte Carlo simulation of charged particle transport. The process continues until all new particles and their subsequent generations leave the geometry or reach very low energies.

continues until all particles are removed from the simulation geometry or the particle energies fall below set thresholds.

Charged particles undergo very many more interactions than photons, and so condensed history techniques and approximations have been devised to simulate these interactions to an appropriate level of physical accuracy within an acceptable allotment of computational time [133, 134]. A simple example of this is the continuous slowing down approximation (CSDA) where electrons are modelled as transferring energy continuously along their path of motion, rather than computing discrete chunks and collisions.

4.1.3 EGSnrc

Given the roots of the MC method in nuclear physics, it is unsurprising that photon transport was among the early problems to harness it. A set of photon and neutron transport codes was released in 1973 by Los Alamos researchers [135]. Many more sets of MC codes have since been developed around the world; one such set, called EGSnrc, was developed in Ottawa to simulate coupled photon and electron transport and is in routine use around the world for simulations in medical physics (EGS for “electron gamma shower” and nrc for the National Research Council of Canada) [133].

For the purposes of this thesis, each particle simulation in EGSnrc can be thought of as two sub-simulations: one for the treatment head, where the radiotherapy source produces photons that travel through and exit the head of the unit, and one for the scoring of dose in a given voxel geometry. These two processes are carried out in systems named BEAMnrc and DOSXYZnrc, respectively. The treatment geometry is given in an “egsphant” file (short for EGS phantom), where a coordinate system is specified and each voxel has both a medium number (an integer from 0-9) as well as a density value. A portion of an egsphant file for a lung compensator is shown in Figure 4.2. The output file, called a “3ddose” file, has the same geometry and coordinate system as the egsphant file and contains, in each voxel, both a dose value and the associated statistical uncertainty.

Doses in DOSXYZnrc are scored in units of Gy per particle history. As a result, as the number of simulated histories increases, it is not the dose values that increase; rather, the dose values converge while the statistical uncertainties decrease, reflecting improved statistics from a larger amount of sampling. The initial 3ddose file produced by DOSXYZnrc thus has doses on the order of 10^{-16} Gy which must be converted to clinical values based on the amount of radiation delivered by the treatment machines. An advantage to this technique is that the results of the MC simulation can easily be scaled to any prescription dose. Even with very large numbers of histories, the statistical uncertainty can and must be reduced further by using several variance reduction techniques available in EGSnrc. These include range rejection, interaction forcing, bremsstrahlung splitting, and Russian Roulette, which are described in detail elsewhere [136–138]. Statistical uncer-

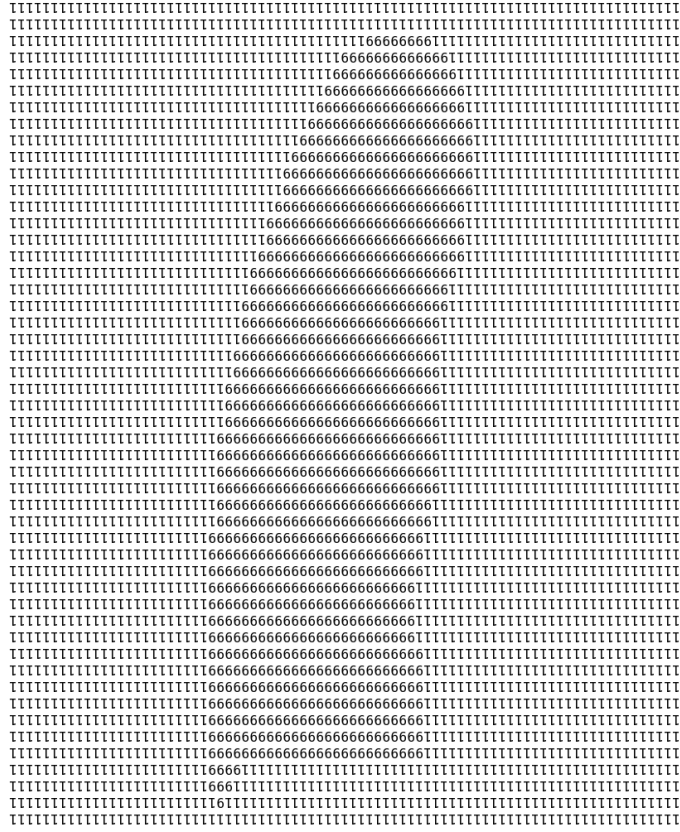


Figure 4.2: A screenshot from an egsphant file modelling a lung compensator. Here, 1 indicates an air voxel and 6 indicates a lead voxel. In the same file, there is a corresponding matrix of material density values.

tainties are also decreased further by using Savitzky-Golay filtering, described in section 4.3.2.

4.2 Phantom production for TBI simulations

Part of the TBI treatment planning at our clinic already includes the production of an egsphant file for each patient in the supine and prone positions using ctcreate, as part of the calculation where the thickness of the lung compensators is determined (described in section 3.3). These patient egsphants, matching the patient CT scans, span from several centimetres below the umbilicus to the level of the neck. The

egsphants are routinely produced at a resolution of $0.25 \times 0.25 \times 0.25$ cm³, and so this resolution was used throughout this MC simulation pipeline.

For a standard MC simulation, a phantom produced from a patient CT scan alone would be sufficient. However, for TBI, the phantom must include three additional components:

1. Lead lung compensators, specific to the treatment field
2. A thin piece of Perspex that holds these compensators in place above the patient
3. The polystyrene flattening filter below the treatment unit head.

To construct a complete TBI MC phantom, egsphant files are first produced for each of these components individually.

The outlines of the lung compensators are stored as a set of points in the treatment planning system as part of the treatment planning routine. However, in Eclipse, these points are given as coordinates centered over the lowest treatment reference marker, t0, and are scaled to a distance of 100 cm from the Cobalt source. A Python (Python Software Foundation, Beaverton, OR, USA) script is used to scale and shift these contour points to reflect their actual positions over t2, 139.7 cm from the source, and to convert these points to an appropriate file format. Next, the egsphants for both the lung compensators and the Perspex support are produced by a MatlabTM (The Mathworks, Inc., Natick, MA, USA) script, using the same coordinate system as the existing patient egsphant. The Perspex support for standard TBI cases is 6 mm thick and 24.7 cm wide in the patient superior-inferior direction, centered over a point 1 cm superior to t2, and covers the patient entirely in the left-right direction.

An egsphant for the polystyrene flattening filter was produced by CT scanning it and using ctcreate, carried out by a previous student. The coordinate grid of the filter phantom is shifted for each patient so that its center is directly above the t0 reference point with the bottom of the filter positioned 56.5 cm below the Cobalt source. The filter is about 70 cm long in the superior-inferior direction, which is longer than the planning CT used. To ensure the entire filter phantom fits above the

patient phantom in simulation, most patient phantoms were padded with 35 cm of air voxels in the inferior direction with a C++ script.

To produce the final MC phantom for the patient, these four phantoms are stacked using a series of C++ scripts. Using measurements from the treatment room and points from the planning CT images, phantoms are produced with appropriate distances between each component to reflect the treatment setup. To reduce computational times, single large air voxels are placed between the components rather than filling a grid with air between them. A visual representation of this phantom for a patient is shown in Figure 4.3, with an axial and sagittal slice of the full geometry and a coronal slice to show the shape of the lung compensators. The display from the EGSnrc simulation software is unable to handle variable resolutions, so Figure 4.3a does not accurately represent the air gaps between the components. However, the simulation calculations use the correct geometry.

A point of interest in the phantom production pipeline is that we did not use the SSD values measured by radiation therapists at the patient simulation appointments. Rather, we measured the SSD from the patient CT scans based on the separation of the patient (measured below point t0), the number of styrofoam pads placed below the patient (each 3.7 cm thick), and the fixed distance of 184.5 cm from the source to the treatment bed surface. This is because the patient may move slightly while being measured in treatment simulation, and the measurements are being collected in a clinical setting where the number of tasks to be accomplished in a limited time make it impractical to measure the treatment SSD with precision better than ± 1 cm. By looking at CT images, we obtained an SSD that reflects the actual position of the patient CT scan with respect to the source during treatment. The measured SSDs from the CT scans were typically 0-2 cm larger than the values provided in the patient treatment specifications.

This entire procedure was performed twice for each patient, once for the supine treatment and once for the prone treatment, resulting in two complete TBI phantoms for each patient. It currently takes roughly 1.5 hours to complete this process for each patient. For a typical adult patient, the initial CT egsphant contains around $6.0 * 10^6$ voxels with a filesize around 50 MB, and the complete TBI egsphant contains around $1.2 * 10^7$ voxels with a filesize around 125 MB.

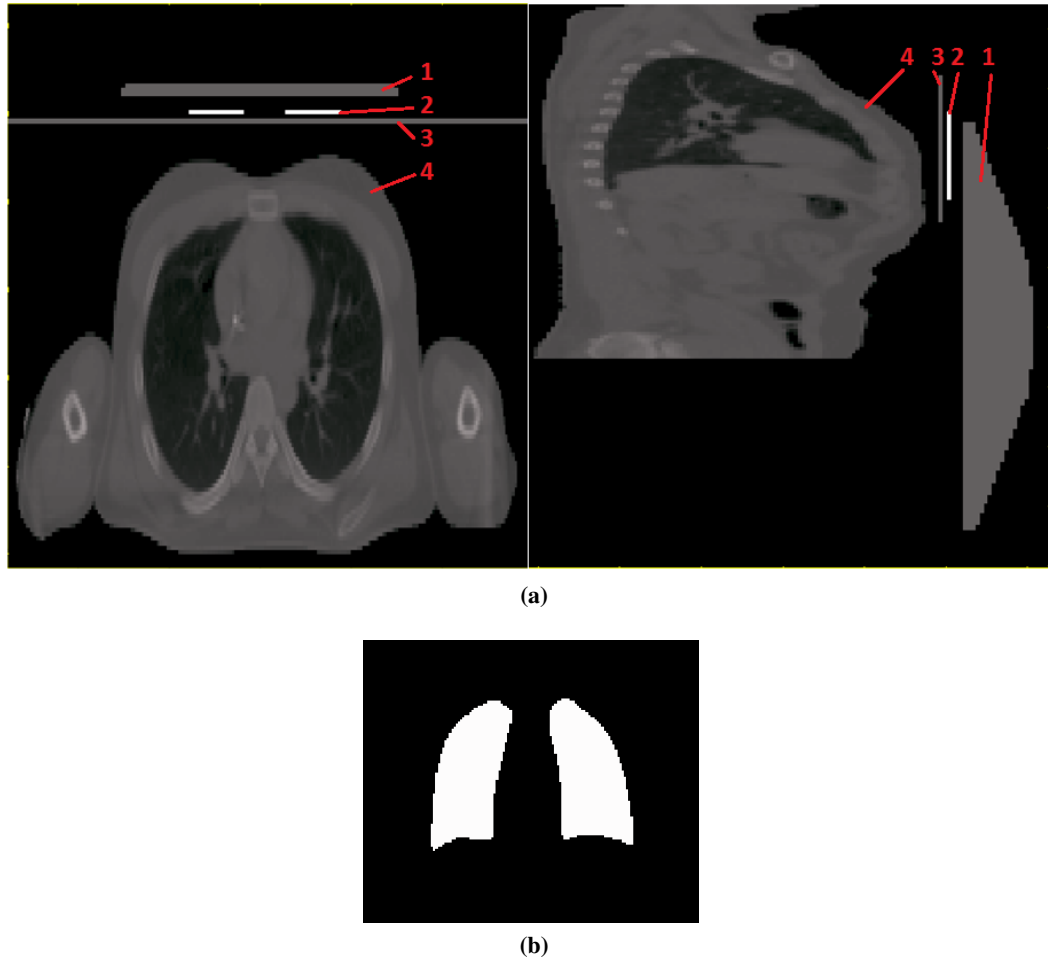


Figure 4.3: Slices of a MC phantom. In (a), the flattening filter (1), the lung compensators (2), the plastic tray (3), and the patient (4) are all shown in both axial and sagittal views. In (b), the lung compensators are shown. The visualization software in EGSnrc is unable to display variable resolution which is used in the beam direction, but the distances are correctly to scale in the simulations.

4.3 Simulations

4.3.1 Cobalt source model

As described in section 4.1.3, MC simulated particles first travel through a source in BEAMnrc, and then are scored in a phantom with DOSXYZnrc. The Cobalt source in BEAMnrc was commissioned by Dr. Tony Teke and collaborators and is described in his Ph.D thesis work [139]. In brief, the Cobalt unit head is modelled in a cylindrical geometry with sets of tungsten and lead slabs reflecting the construction of the source housing container. The source itself is modelled based on a Cobalt spectrum measured by a group in Ottawa [30].

To ensure proper commissioning of the Cobalt source in BEAMnrc, several validation measurements were conducted in water tank measurements, also described in Dr. Teke’s thesis. Lateral beam profiles at four depths in a water tank and a PDD curve from the top of the tank to 25 cm of depth along the beam axis were measured with an ionization chamber, treating at an SSD of 80 cm and a field size of 35x35 cm² at 80 cm (which is the field size used in TBI treatments). An identical treatment geometry for the water tank was modelled in DOSXYZnrc. Both the beam profile shapes and absolute dose values at several points in the tank showed excellent agreement between simulation and measurement.

4.3.2 Simulation procedure and de-noising

For our sweeping beam TBI technique, we require a Monte Carlo source that is able to sweep over the patient geometry. Two such sources in DOSXYZnrc, called Source 20 and Source 21, were invented by Popescu and Lobo to model continuously varying beam configurations [140]. Source 21 is applied to the following simulations to harness this capability. The 90 degree sweep of the Cobalt unit head is modelled with twenty-one control points spaced equally over an arc in the patient phantom with coordinates depending on the patient treatment markers and SSD,

$$y_i = t_{0y} + \text{SSD} \cos(90 - \theta_i) \quad (4.4)$$

$$z_i = t_{0z} - \text{SSD} \sin(90 - \theta_i) \quad (4.5)$$

where t_{0y} and t_{0z} correspond to the y and z coordinates of reference marker $t0$ and θ is the angle of the treatment head with respect to the horizontal (that is, an angle of zero degrees would represent the treatment head pointing directly at a wall).

In each patient simulation, two billion histories were simulated. This number is justified in the following section. The default cutoff energies in EGSnrc for electrons and photons (0.7 MeV and 0.01 MeV respectively) were used. A factor of 1000 was used for directional bremsstrahlung splitting [136]. MC simulations at our centre are run in parallel, spread across as many as 256 jobs operating simultaneously. The Condor High-Throughput Computing software housed at the Kamloops Data Centre serves as the platform for our simulations. A typical simulation for one treatment position with two billion histories in an adult-sized patient, split into 250 jobs, takes approximately 75 minutes to complete.

Recall that the phantoms used in MC simulations are composite phantoms including several materials in addition to the patient. The first step in processing the simulation data is to strip the 3ddose files to remove the doses to the flattening filter, lung compensators, and Perspex tray, as well as the 35 cm of air that was often added inferior to the patient CT scan to accommodate the full flattening filter. The stripped 3ddose file is thus restored to a uniform resolution of $0.25 \times 0.25 \times 0.25 \text{ cm}^3$ with the same geometry as the initial patient egsphant. The initial dose file is over 300 MB in size, and after stripping and processing, the file is around 125 MB in size.

Given the nature of a MC simulation, there is bound to be a level of statistical noise present in the data, whereas a real dose distribution would be continuous in the patient. To reduce the statistical uncertainties of the dose files, a three-dimensional Savitzky-Golay filter is applied. This smoothing filter passes through the data in a $7 \times 7 \times 7$ region of voxels at a time, but a smoothing fit for the data is accepted in each region only if a statistical test is passed that determines whether the fit is harmlessly minimizing the statistical noise or erasing a true feature of the dose distribution [141, 142].

After Savitzky-Golay de-noising, the 3ddose file is converted from Gy per particle values to real dose values in Gy. The calibration factor was determined by an ion chamber measurement described in section 4.3.4 and is adjusted for each patient based on the date of their treatment and their treatment time.

4.3.3 Optimization

The very large size of these TBI MC phantoms compared to those used for standard MC dosimetry procedures exacerbates the issue of statistical noise in the simulations. To decrease statistical uncertainties and mitigate the issue of hot and cold spikes in the dose distributions, we can run several independent MC simulations for each phantom and then combine these sub-simulation results voxel-by-voxel with a weighted mean, rather than use a boundlessly increasing number of histories [142].

This strategy then raises the following question: in the interest of producing the highest possible quality of data in the least amount of computational time, what is the optimal number of sub-simulations to use for each simulation, and what is the optimal number of histories to use for each one? To answer this question systematically, for one supine patient phantom, twenty-five MC simulations were carried out: five simulations each of 1.0×10^9 , 1.5×10^9 , 2.0×10^9 , 2.5×10^9 , and 3.0×10^9 histories, using different seeds in the egsinp files to ensure the random number sequences were different for each simulation. Then, dose distributions were produced by taking the weighted mean of either two, three, four, or five of the simulation results of a given number of particle histories. All dose distributions were stripped and de-noised individually, and then the composite dose distribution after taking the weighted mean was de-noised a second time. Simulations of different particle history numbers were not mixed, and individual simulations were included for comparison as well. The total number of final dose files for comparison was twenty-five: five individual simulation results, and twenty composites from two to five sub-simulations.

The composite simulation of five times three billion histories was taken as the highest quality for comparison with the other simulations. The goal was to determine the smallest number of histories and simulations that could be used to obtain similar organ dose results as this composite. The results of the simulations were compared by looking at the dose to the left and right lungs of the patient as well as a spherical contour 2.5 cm in diameter centered at a depth of 5 cm below treatment marker t0. Both the mean and standard deviation of the doses within the contours were considered and an abridged version of the results is given in Table 4.1. It is seen that there is a noticeable decrease in the standard deviations and thus im-

Histories per sub-simulation	Number of sub-simulations	Spherical contour		Left lung		Right lung	
		Mean (Gy)	SD	Mean (Gy)	SD	Mean (Gy)	SD
$1 * 10^9$	1	6.76	5.8%	5.18	12.2%	5.38	11.7%
$2 * 10^9$	2	6.76	3.1%	5.16	9.5%	5.36	8.5%
$3 * 10^9$	5	6.75	2.8%	5.16	8.9%	5.37	8.6%

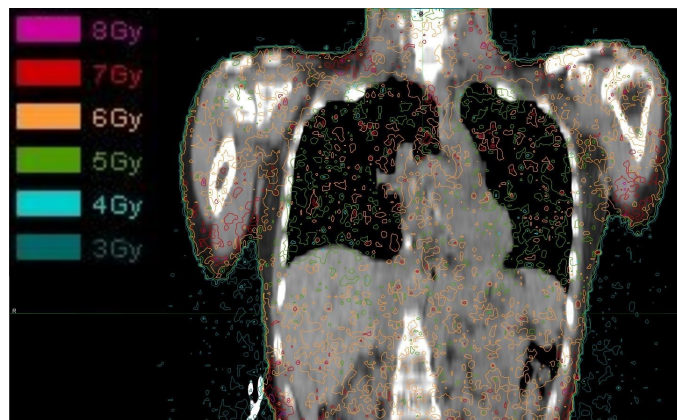
Table 4.1: Abridged results of an optimization study. Dose information are shown from MC simulations of the same supine treatment (6 Gy to prescription point) with different numbers of particle histories and sub-simulations. The simulation with the most histories was taken as the best possible simulation quality. While the dose results remain similar with decreasing numbers of particles, the images can be seen to have more statistical noise as shown in Figures 4.4.

proved homogeneity when using more than one simulation, but the improvement from two times two billion histories to five times three billion histories was not as strong, despite the large increase in total histories used. The distributions were also compared qualitatively, and three cases are shown in Figures 4.4. Based on these results, it was decided that two times two billion histories would give dose data of acceptable quality in a reasonable amount of computation time. The statistical error of a composite dose file from two times two billion particle histories for a standard adult-sized patient is on the order of 2% in the lung and 1% in the rest of the body.

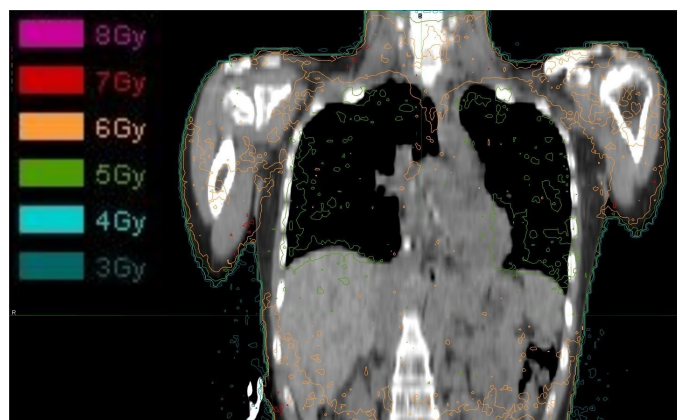
It is worth noting that while the organ doses are visibly noisier with fewer simulated particle histories, the organ doses are not dramatically different in these cases. This is because the statistical errors cancel out in the large organ contours. In cases where a point dose will need to be examined, a larger number of sub-simulations and histories should be used (e.g. five times three billion histories), but in cases where only organ doses will be considered, smaller simulation numbers can be used to obtain the same results.

4.3.4 Calibration

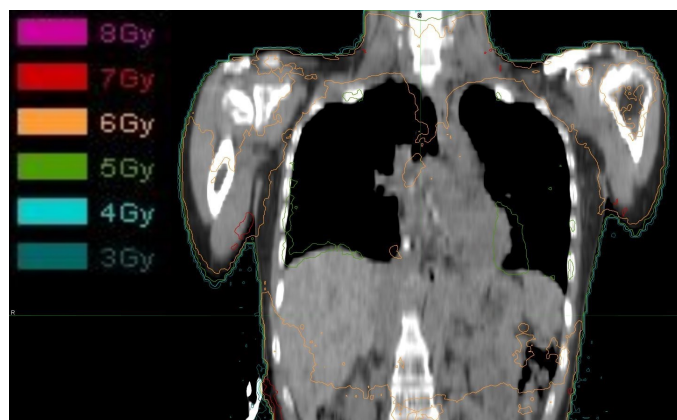
For linear accelerators, the amount of radiation delivered is parameterized by monitor units (MUs). The conversion of DOSXYZnrc outputs to clinically meaningful



(a) One simulation, one billion histories.



(b) Two simulations, two billion histories each.



(c) Five simulations, three billion histories each.

Figure 4.4: Isodoses for the three dose distributions corresponding to the three conditions listed in Table 4.1. The distributions become less noisy with more simulated particle histories at the expense of computational time.

dose values for linear accelerator MC simulations is outlined by Popescu et al [143]. For a Cobalt unit, however, this method does not work, as the treatment is parameterized by time rather than MUs. In order to scale our simulation results from Gy per particle to physical dose in Gy, a ratio between measured dose and simulated dose at a point was used for a radiation delivery resembling a TBI treatment. The measurement was made with an ion chamber in a block of solid water at a depth of 10 cm on the beam axis. The solid water phantom had dimensions 40x40x20 cm³, centered beneath the treatment head at an SSD of 160.2 cm. The flattening filter was positioned between the treatment head and solid water. The solid water was irradiated during five full sweeps of the gantry with a field size of 35x35 cm² at 80 cm from the source. A picture of the setup is shown in Figure 4.5.

A MC simulation was executed with the same treatment geometry, appending the flattening filter phantom above the solid water phantom at an appropriate distance. Five simulations of three billion particles each were used, as the desired measurement was a point dose at the location of the ion chamber, rather than some contour where statistical uncertainties would cancel out. A visualization of the phantom is given in Figure 4.6. As before, the visualization software does not accurately depict the large air voxel placed between the filter and solid water phantoms, but appropriate spacing is in place for the simulations.

Using the ratio of the measured dose rate and simulated dose, with units of Gy per minute and Gy per particle respectively, a conversion factor of the number of particles per minute emitted by the Cobalt source is obtained. This value is to correct for source decay over the time between the measurement and the calibration in August 2015, giving 1.17×10^{15} particles emitted per minute. The reason for dialling the dose rate back to the calibration date is to provide a more convenient value that can be adjusted for each patient based on the day that they were treated.

Therefore, for each patient simulated in Chapter 5, the conversion factor is calculated by multiplying the above value by three factors: an exponential decay factor corresponding to the treatment date, the treatment time for the patient per field, and the number six to reflect the six treatments given for a 12 Gy treatment. This could easily be applied to other prescription doses as well. The supine and prone dose files obtained this way are ultimately added together, described in section 4.4.



Figure 4.5: Setup of the calibration measurement. The clinical flattening filter is in place and an ion chamber is inserted at a depth of 10 cm in a 40x40x20 cm³ block of solid water. The treatment was delivered over five sweeps of the beam.

4.3.5 Validation measurements

Initial validation measurements were undertaken when the MC Cobalt source was commissioned by a previous graduate student as described in section 4.3.1. We performed a new set of validation measurements to ensure that the strong fit between measured and simulated doses holds true for a more realistic patient simulation and not only in a homogeneous tank of water.

Two patients, who are not included in the study in Chapter 5, received treat-

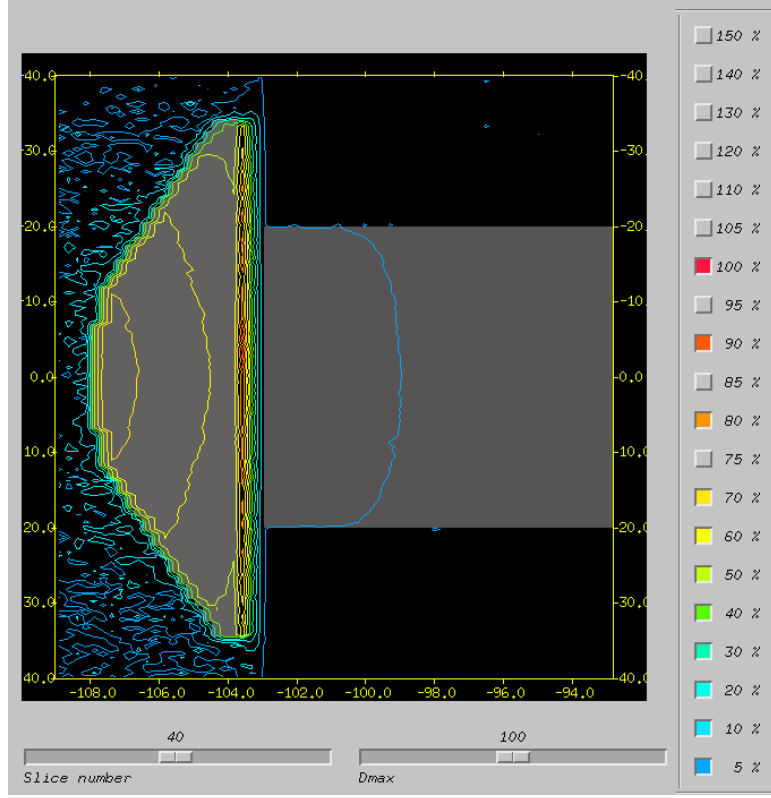


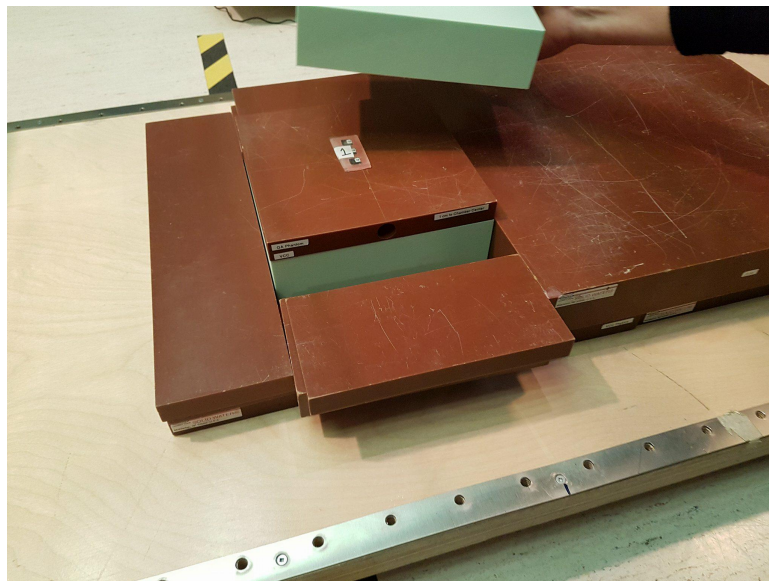
Figure 4.6: Visualization of the simulated dose distribution corresponding to the measurements shown in Figure 4.5. The coordinate system in the simulation is rotated; here, the beam axis is from left to right across the page. Most dose is delivered to the flattening filter with a relatively small amount delivered to water. The dose to the point corresponding to the ion chamber location in solid water was recorded.

ments on a different treatment protocol with non-standard lead lung compensators. One patient had a single set of 12 mm blocks, while another patient had a standard set of 2 mm blocks with a second narrower set of 11 mm blocks to sit on top of the first set. We used these non-standard lung blocks in both a simulation of a treatment and a measurement. To create the phantom, blocks of solid water were used to create a shape roughly the size and depth of a patient. Two sets of lung-equivalent foam were used as well to provide a non-homogeneous tissue distribution to mimic the non-uniform patient geometry. A picture of the setup is shown in Figures 4.7.

The phantom was treated at extended SSD and ion chamber measurements were taken in a piece of solid water between the two pieces of lung foam. Sets of three OSLDs were used as well, in two places: one set at the patient surface underneath 6 mm of paraffix wax buildup, and one set beneath the first lung foam block, on top of solid water. The beam was turned on for 20 sweeps of the unit head.

After these measurements, the phantom was transported to a CT simulator and was rebuilt on the CT couch. The phantom was scanned (without an ion chamber in place, leaving an air gap in the phantom) and converted to a MC phantom with `ctcreate`. Five sub-simulations of three billion histories each were produced for two MC phantoms, which were identical apart from the two different sets of lung compensators that were used. Statistical uncertainties were below 1% and simulated isodoses for one of the treatments is shown in Figure 4.8.

The results of both measurement and simulated doses are given in Table 4.2. In simulation, the lung blocks were intentionally offset slightly from the tip of the ion chamber insert in the simulation so that the penumbra from the lung blocks would overlap with solid water at an appropriate depth instead of the air gap in the phantom from the ion chamber insert. Additionally, there were no OSLDs present in the CT scan of the phantom. To obtain the simulated doses at points representative of where the OSLDs were placed during the measurement from the Cobalt unit, we measured at a depth of 6 mm below the top of the phantom for the surface OSLD set to accommodate for the thickness of the OSLD and the buildup provided by the paraffin wax, and a depth of 1 mm into the solid water beneath the first lung block. The results show strong agreement at most points of comparison. Reasons for differences between points could be due to several factors: changes in the positions of phantom components when transporting the phantom from the Cobalt unit to the CT scanner, and when transferring from the TBI treatment couch to the CT couch; differences in positioning of the top pieces of solid water and lung foam with and without the OSLDs present, which produced small air gaps in the measurement that were not present in the MC phantom; inaccuracies in the approximation used to compare measured OSLD doses with doses at depth in solid water (e.g. this did not account for small inverse square effects as a result of collecting data further from the source). The goal of these measurements was not necessarily to see 100% agreement, but rather to test the TBI MC procedure in a complex, heterogeneous



(a)



(b)

Figure 4.7: Experimental setup used for the validation measurements at treatment conditions. The flattening filter is also in place as shown in Figure 4.5. (a) The interior of the phantom includes two pieces of lung-equivalent foam to mimic a heterogeneous patient environment. A set of OSLDs is placed below the first piece of foam. (b) Solid water is placed above the top foam block, and another OSLD is placed on top of this. An ion chamber is placed at depth at a position within the penumbra of the lung compensators.

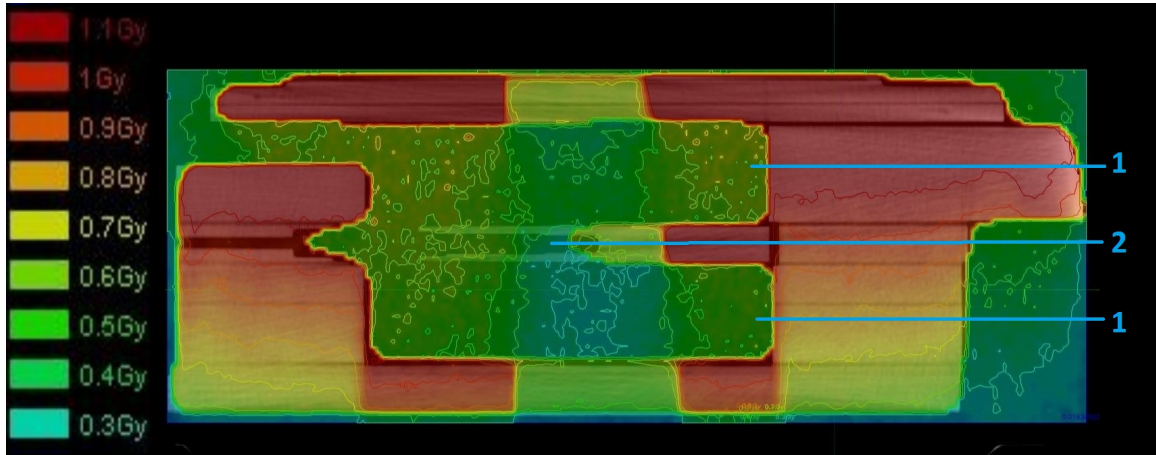


Figure 4.8: Isodoses for the simulation of the experimental setup shown in Figure 4.7. The treatment corresponded to a 1 Gy prescription to mid-separation in the phantom. The simulated phantom includes two lung-equivalent blocks (1), an air gap in the ion chamber insert (2), and various blocks of solid water (rest of phantom).

geometry resembling a treatment. Given these results in tandem with the earlier water tank measurements when the MC Cobalt source was commissioned, we are satisfied and confident in the doses reported by this MC dosimetry technique.

4.4 Deformable registration of dose distributions

So far, the pipeline for simulating a single MC phantom has been described in either the prone or supine positions. To obtain organ dose data, the prone and supine distributions must be combined. The shape of the patient changes between the supine and prone positions for reasons including differential compression of mobile tissues in the two positions, or different positions of the arms or head relative to the torso. Additionally, the CT scanning boundaries on the patient may be slightly different between the two scans. As a result, the dose files from the supine and prone treatments cannot simply be overlaid, as the geometry is not the same. Instead, an intensity-based deformable registration tool in MIM MaestroTM v6.6.8 (MIM Software Inc., Cleveland, OH, USA) is used to add the doses together based on the positioning of the tissues in each image. The prone dose data is deformed to

	Case # 1		Case # 2	
	Simulation (Gy)	Measurement (Gy)	Simulation (Gy)	Measurement (Gy)
Ion chamber	0.59	0.54	0.55	0.55
OSLD (surface)	0.68	0.63	0.61	0.61
OSLD (lung)	0.64	0.63	0.59	0.65

Table 4.2: Results of a validation study. Measured and simulated doses are presented for the two OSLD measurements and ion chamber measurement pictured in Figure 4.7 compared with the simulated doses at those points in the corresponding MC phantom. Given the uncertainties involved in producing an MC phantom exactly identical to the treatment delivered on a different unit, as well as the very close agreement between measurement and simulation in earlier homogeneous water tank studies, the agreement here between measurement and simulation is acceptable.

the supine image volume, and these deformed data can then be added to the supine data after they have been registered to a common geometry. A sample set of supine dose, prone dose, and total dose distributions acquired with this technique is given in Figure 4.9.

The exact details of the deformation algorithms of commercially available software are often obscured from users for competitive reasons, although some studies have been undertaken to study the effectiveness of the registration in MIM Maestro alongside other similar commercially available tools [144, 145]. Deformable registration is used clinically for cases including patients being treated in the same treatment position on different dates who have lost weight since an earlier treatment, or have tumour shrinkage during a radiation therapy course with a large number of fractions, or for changes in internal geometry, such as organ resections or changes in bladder filling levels between scans. Additionally, the tools can be used when patients are being treated with a second course of radiotherapy to determine which regions have already received dose in the first course. A full validation of the deformable registration algorithm to measure the uncertainties borne by the registration would be a highly nontrivial and challenging task beyond the scope of this thesis. However, given the large CT images with a large amount of bony anatomy present to guide the registration, and by visual inspection of the results

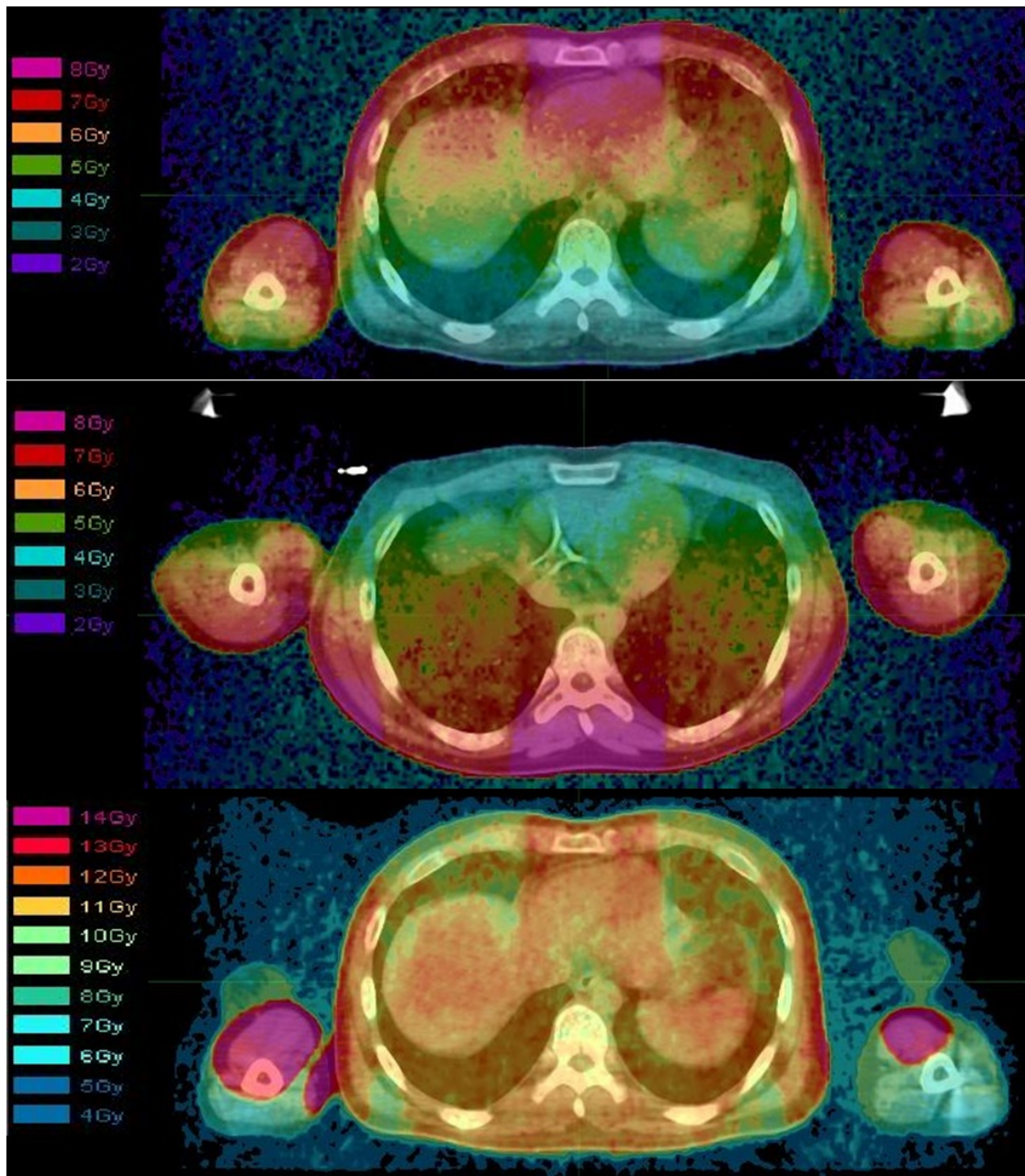


Figure 4.9: Final results of a MC simulation for a patient. The three images correspond to the supine treatment, prone treatment, and final distribution. The prone treatment is displayed upside-down for ease of comparison with the other figures.

and from the experience of physicists using MIM Maestro clinically in the department, we are confident in the results obtained from this technique.

It is possible to improve the quality of the deformable registration in MIM Maestro using a tool called RegRefine. With this tool, an expert user can place “locks” over certain areas of the CT image at intermediate stages when prompted by the software, to place more importance on certain regions and to reiterate registrations over challenging areas until a satisfactory result is produced. When this TBI MC technique is implemented clinically, locks could be applied to our technique, but in the interest of reproducibility of the results in the next chapter, no manual intervention was involved in the deformable registrations for this study.

Chapter 5

Retrospective dose analysis of a TBI patient cohort

5.1 Purpose and aim

The TBI technique used in our clinic is described in detail in Chapter 3 alongside approaches in place at other institutions. Our technique, like the majority of techniques in place around the world, is a POP treatment with custom-designed lung blocks for each patient.

Our technique is effective, being commissioned to deliver a dose within 10% of prescription and has been in place for over 23 years [59]. However, given the advances in technology and radiation oncology physics in recent years, it is now possible to achieve a higher degree of conformity than the current 10% limit; for most other radiation treatments, the allowed variation from a prescription dose is -5% to +7%.

There are some features of our current treatment that could be improved in a new technique. For many patients, the experience of being lowered to a floor-level treatment bed for an extended period of time, especially for the portion spent in the prone position, can be uncomfortable. A treatment that allows for the patient to be treated on a couch of standard height would represent a shift towards an improved TBI patient experience. Moreover, if the patient can be treated in one position instead of two, then there is less time spent positioning the patient and less opportunity for patient positioning errors. Additionally, the process of producing lung blocks for each patient is resource-intensive and time-consuming, and lung blocks of a single shape and thickness cannot fully account for the three-dimensional vol-

ume of the lung in the patient. The lung compensators also block the tissue anterior and posterior to the lungs. This technique was commissioned to maintain the lung doses at prescription level, but it is not trivial to adjust the level of shielding if a new protocol required further lung dose reductions or other organ dose reductions. A more conformal TBI technique that does not use physical lung blocks could provide the same amount of organ sparing with a simpler clinical workflow, and would allow for different protocols to be enacted should they become of interest.

These challenges could be overcome by a technique such as helical tomotherapy or VMAT, as described in Chapter 3. Our clinic has a high level of physicist expertise in delivering VMAT treatments, making this a logical choice in upgrading our TBI technique. In VMAT, organ dose constraints must be specified in advance, and the treatment is inverse planned from these constraints. To reproduce our existing treatment on a new platform, we thus require organ doses from our sweeping Cobalt-60 technique, which have not been available. With the novel MC approach described in Chapter 4, we can now obtain organ doses from TBI patients to satisfy this goal and bring our clinic closer to implementing a new technique. Moreover, our clinical TBI experience is based on the sweeping-beam method, and change cannot be implemented to delivered doses without a good understanding of the impact on clinical outcomes, further justifying this study. In this study, we simulated the treatments of recently treated TBI patients in our clinic and present organ dose data from this population.

5.2 Methods: patient selection and contouring

20 patients were selected who had received 12 Gy in 6 fractions. Patients could only be simulated if the treatment took place after 2011 when our technique was updated from a film-based method to the current CT-based method [128]. For convenience in calculations, we only chose patients who had been treated since the last Cobalt source replacement in August 2015. Patients with a range of body sizes were selected, as measured by the anterior-posterior separation beneath the t0 reference mark, (range: 10.1 cm - 23.6 cm). The patients include 10 males and 10 females, including pediatric and adult patients (age range at treatment: 3 years - 51 years). Patients with resected organs were excluded from the study, as were any

patients whose data records were non-standard for any reason (e.g. uneven spacing between rows in the CT phantoms, lung compensators saved in an unusual format).

Based on the toxicities that are most of interest in TBI as outlined in section 3.2.4, the contoured organs for this study were the thyroid gland, the lungs, the kidneys, and the liver. These were contoured by the author in MIM Maestro with sample contours for a patient shown in Figures 5.1.

A body contour was produced for each patient with the four most superior slices (2 cm) and inferior-most eight slices (4 cm) subtracted from the contour. In these two regions, because the CT image volume does not include superior and inferior portions of the body that would otherwise provide scatter dose contributions to these slices in our phantom, we subtract these areas to remove slices from the mean body dose calculation that are known to be underdosed. A previous graduate student in our department studied this underdosing effect for TBI MC simulations, measuring dose at the prescription point beneath reference mark t0 [139]. It was found that, in this direction, having only 4 cm of scatter gave 8% less dose than a measurement with 16 cm of scatter, with the dose difference falling off dramatically with less than 4 cm of scatter. This explains our choice to remove 4 cm of CT slices from the inferior edge of the body contour. We assume that in the superior direction, the same effect is present, but less pronounced because the missing head occupies a smaller volume than the missing torso region and would thus provide less scatter if it was present in the CT volumes. The thyroid gland of one patient resided completely within the top four slices that are expected to have underestimated dose, and part of the gland was truncated by the anatomical location of the CT cutoff in the superior direction. As a result, this thyroid is excluded from the organ results in Figure 5.5 in the next section.

For some patients, the prone and supine CT images were not cut off at the same anatomical locations in treatment planning, and the deformable registration was not able to produce a summed dose in voxels that did not have a corresponding point in the other image. Where it was clear that this happened for a patient, further crops were made from the body contour at the superior-inferior edges of the image. Additionally, the arms were removed from the body contour up to the level of the shoulder. The primary reason was due to the challenge of the deformable registration tool in these areas, as the arms are located at different positions relative

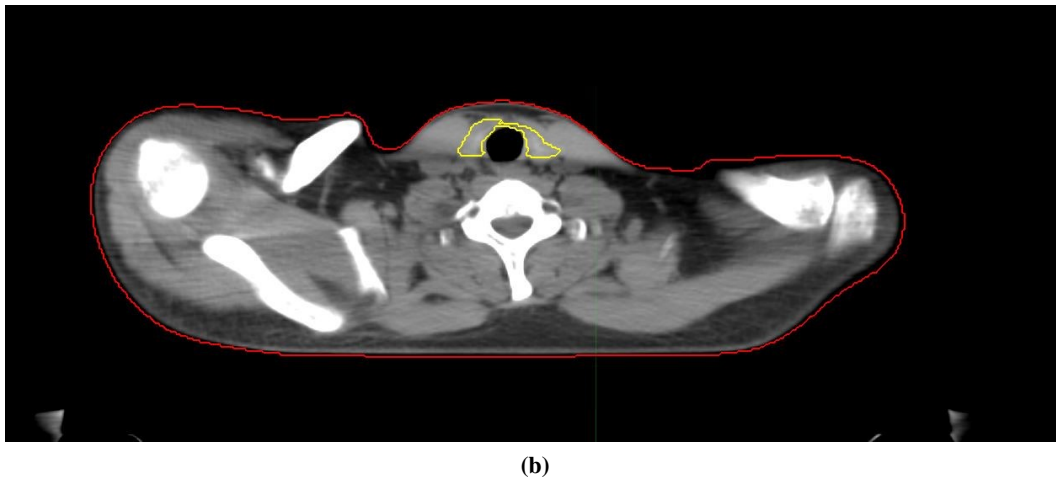


Figure 5.1: Contours shown in MIM Maestro for a patient. (a) The body contour (red), lungs (blue and purple), kidneys (orange and brown), and liver (green). (b) The body contour (red) and thyroid gland (yellow).

to the rest of the body in the supine and prone positions. Moreover, as we did not model bolus in our simulations that is present in treatment to provide scatter dose to the arms, and because of CT artifacts in the arms that would interfere with Monte Carlo dose calculations in these regions (visible in Figure 5.1a), the true body dose was not accurately represented in the arms in our simulations.

Within each contour, the mean, minimum, and maximum doses, along with the standard deviation of the dose in each contour, were determined with MIM Maestro. Additionally, a homogeneity index (HI) was calculated for the body contours,

$$HI = \frac{D_5 - D_{95}}{D_{50}} \quad (5.1)$$

to provide another metric of dose conformality within the target volume. D_x is the dose that is delivered to the $x\%$ of voxels within the contour receiving the highest doses. There are different definitions for HI in the literature [146]; here, D_5 and D_{95} were chosen for robustness against hot or cold spots due to statistical noise. In this definition of HI, a perfectly conformal plan would have an HI of zero.

5.3 Results and discussion

Aggregate results representing the organ doses and the standard deviations of organ doses across all 20 patients are shown in Tables 5.1 and 5.2. This data provides our clinical team with the range of doses that are delivered to each organ in the interest of implementing VMAT constraints on a future technique.

However, these data do not account for the size of the patient. In Figure 5.2, it is demonstrated that there is a strong relationship between the size of the patient and the mean body dose as measured within our body contours ($R^2 = 0.91$ with either linear or exponential models). All mean body doses fell within the $12 \text{ Gy} \pm 10\%$ prescription dose, although the smaller patients received doses on the lower edge of the threshold while only the largest patient received a mean dose of 12 Gy. One reason why most patients are receiving less dose than prescription is the blocking of tissue anterior and inferior to the lungs by the lead compensators.

A factor that explains the variation of mean body dose with patient size is the changing shape of POP dose distributions with increasing patient size. This effect

	Mean	SD	Min	Max
Left lung	10.99	0.29	10.44	11.62
Right lung	10.48	0.30	10.48	11.49
Left kidney	11.65	0.33	10.98	12.25
Right kidney	11.73	0.42	10.90	12.29
Liver	11.24	0.27	10.73	11.69
Thyroid	11.79	0.45	10.84	12.58
Body contour	11.46	0.33	10.93	12.01

Table 5.1: Aggregate organ dose results (in Gy) across the 20 simulated patients. The values represent the mean and standard deviation of the average doses delivered to each organ. The maximum and minimum average doses delivered to patients for each organ are shown.

	Mean of SD	Min SD	Max SD
Left lung	0.49	0.35	0.67
Right lung	0.48	0.29	0.68
Left kidney	0.26	0.16	0.40
Right kidney	0.28	0.19	0.47
Liver	0.37	0.25	0.53
Thyroid	0.20	0.14	0.29
Body contour	0.78	0.64	0.86

Table 5.2: Standard deviation information of the doses delivered to each organ are shown (in Gy) to illustrate the level of dose homogeneity in the final simulated distributions. The average of the standard deviations across the 20 patients is given for each organ, as well as the minimum and maximum standard deviations.

is illustrated in Figure 5.3 with Cobalt-60 PDD curves for three different amounts of water at extended SSD. These curves are normalized to 12 Gy at mid-separation, mimicking the prescription of a TBI patient. With an increasing depth of water, higher peaks are seen in the PDD curves, and the average doses for these three sizes are 12.0 Gy, 12.1 Gy, and 12.3 Gy, respectively.

Another contribution to the lower mean body dose in smaller patients is due to lower scatter dose contributions throughout the body. While patients are positioned

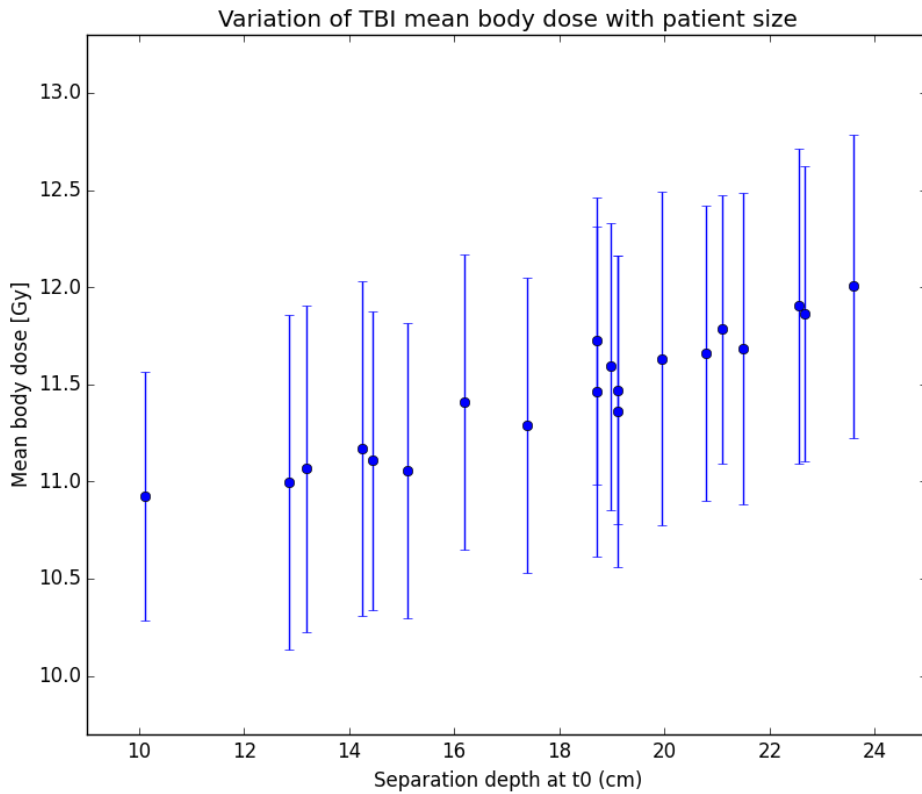


Figure 5.2: Variation of TBI mean body dose with patient size for the 20 patients. Size is measured by the separation depth at reference mark t0. The error bars show the standard deviation of the dose delivered to voxels inside the body contour. All mean doses are within the prescription tolerance. It can be seen that the mean doses increase with patient size.

with bolus around the head and the legs, smaller patients would still receive a lower scatter dose contribution, simply from having less tissue for scatter. This variation with patient size does not appear in the standard deviations of the voxels within the body contours. That is, while the doses delivered to the smaller patients were lower, the conformality of the treatments was the same as for larger patients. Accordingly, the HI values are not impacted by patient size, with ranges from 0.14 to 0.22 and an average value of 0.19 across the patient population, shown in Figure 5.4.

Because of the increasing mean body dose with patient size, the organ doses

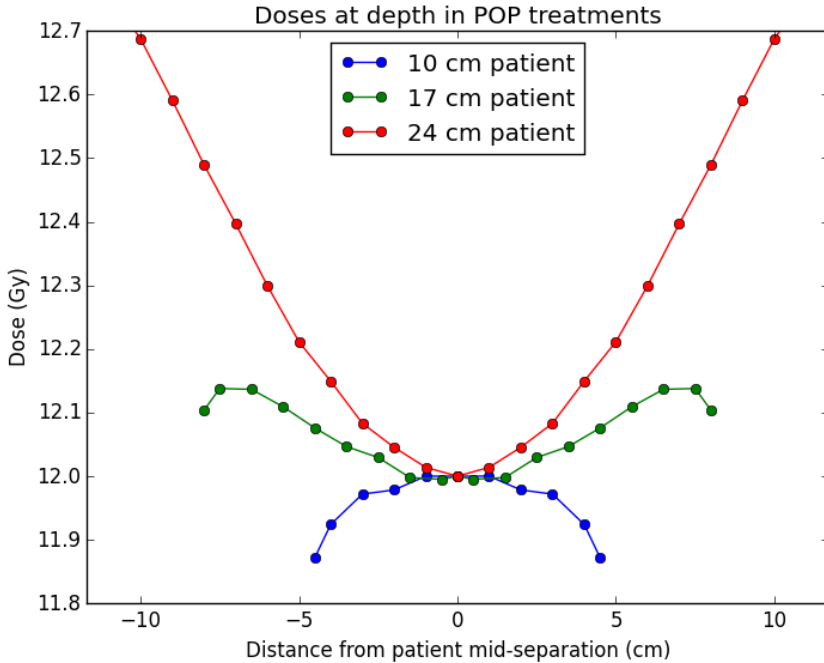


Figure 5.3: PDD curves for POP beams in water for three patient widths.

Tabulated Cobalt-60 PDD data [147] (collimator setting $35 \times 35 \text{ cm}^2$, SSD 160 cm calculated using Mayneord factors) are added together and scaled to 12 Gy at mid-separation.

are better represented relative to the mean body dose for each patient as shown in Figure 5.5. The straight line in each of these figures represents the mean body dose; points above these lines represent organs receiving more than the mean body dose for a given patient, and vice-versa. From these figures, we can see that the lungs and liver consistently receive lower doses than the mean body dose in each patient, and vice-versa for the kidneys and thyroid. A sample dose-volume histogram (DVH) is shown in Figure 5.6 for an individual patient. An ideal DVH for a patient would approach the shape of a rectangle with 100% of the PTV receiving the prescription dose, although real treatment plans do not achieve this.

The results from this retrospective study, in addition to serving as a basis for VMAT organ dose constraint implementation, suggest that the treatment time for

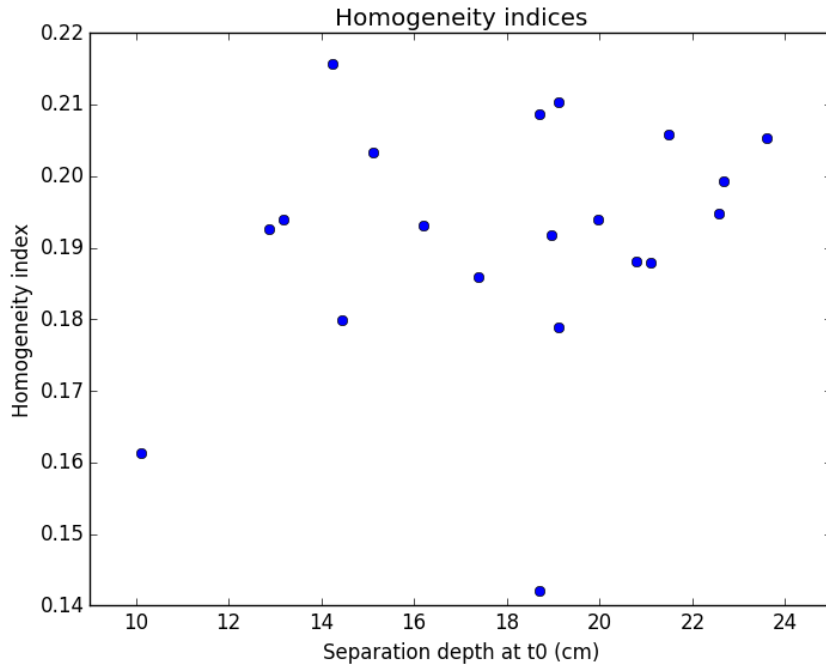


Figure 5.4: The homogeneity indices of the dose delivered to the body contour for each patient plotted against patient size. There is no clear trend, indicating that the homogeneity of the dose does not change with size.

smaller patients could be increased if it is desired for them to receive doses closer to 12 Gy. This would not be challenging to implement. For individual organ doses, on the other hand, while there exists some flexibility in our technique to modulate organ doses (such as modified lung shielding or shielding for additional organs), it is much more challenging to meaningfully adjust these without upgrading to a technique such as VMAT or helical tomotherapy.

It is important to recall that the mean body doses in all patients are likely to be systematically underdosed by a few percent because of the missing scatter in each direction, even with the precautions in the body contours described in section 5.2. Additionally, the bolus material above the shoulders and around the head and neck are not included in our simulations at present, and could lead to further simulated underdosing of the patient.

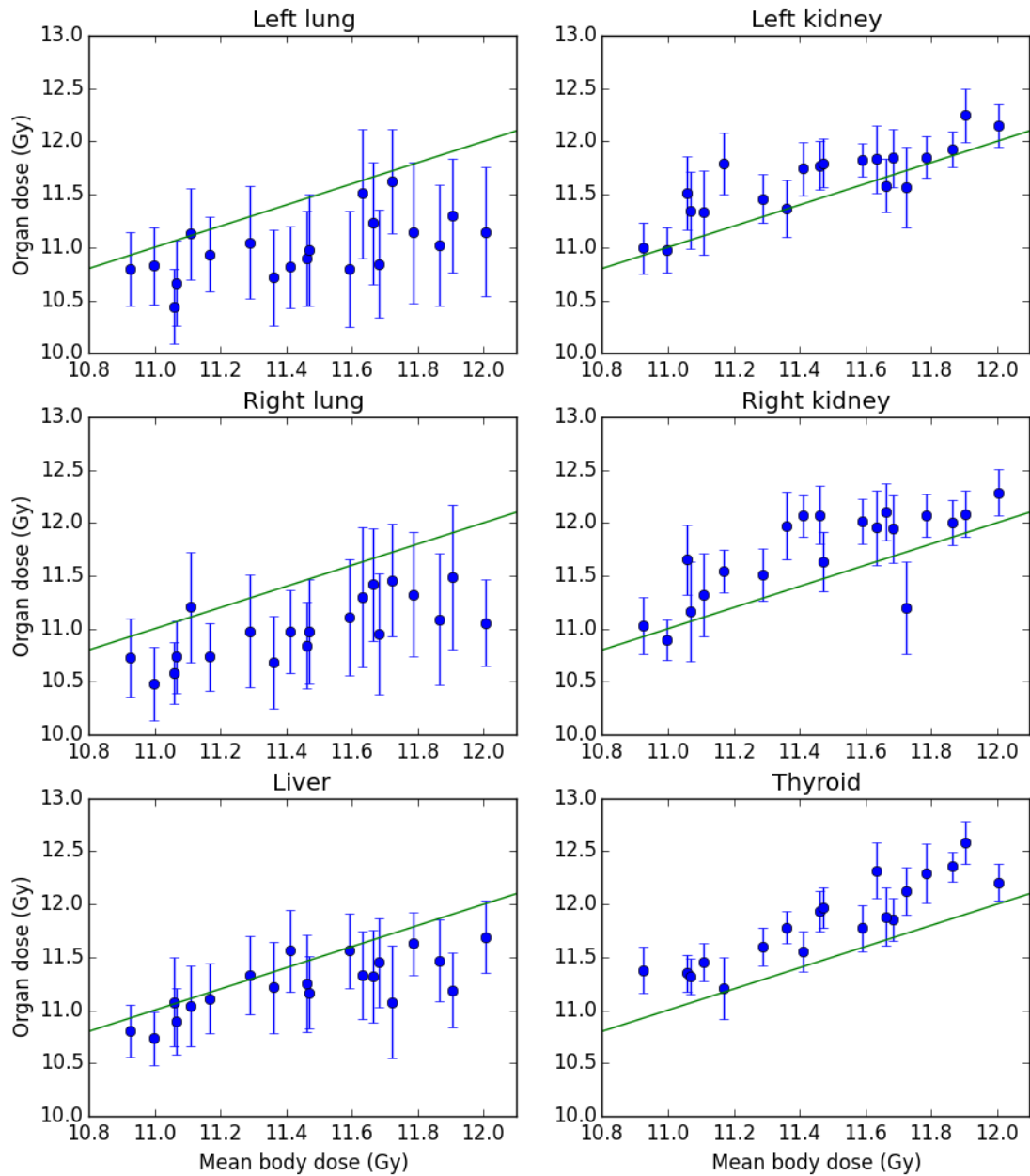


Figure 5.5: Organ dose data plotted against mean body dose. Each subplot includes a line of equality for ease of interpretation. Points above the line indicate that the organ dose for the patient was above the mean body dose, and vice-versa. The lungs and liver are consistently below the mean body dose, and the kidneys and thyroid are consistently above. The error bars are the standard deviation of the dose delivered to voxels within the organ contours.

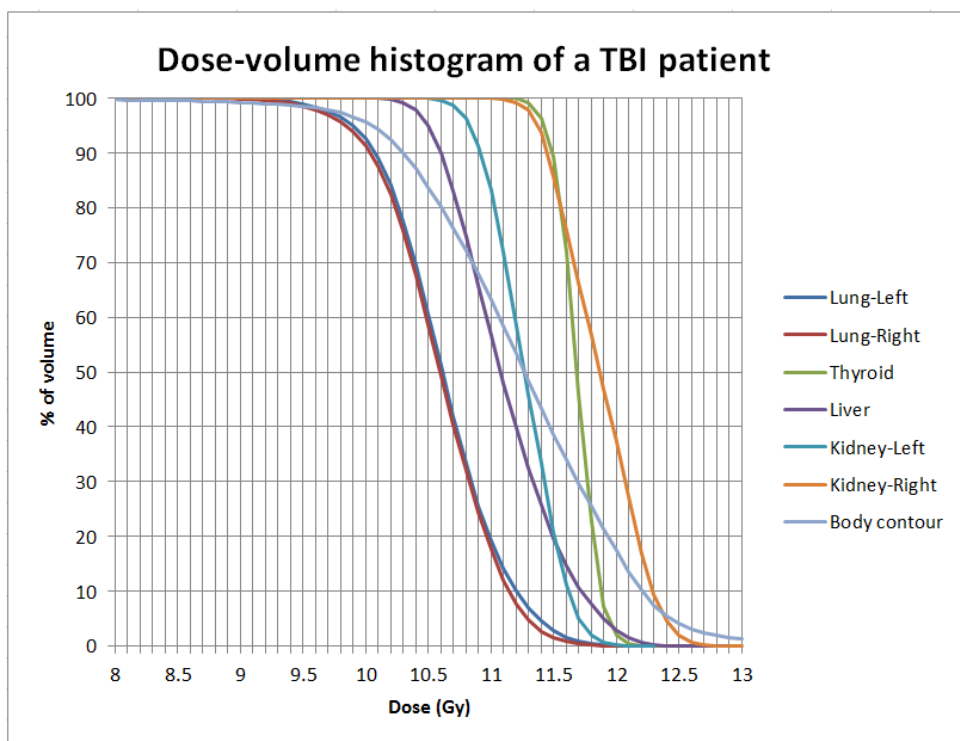


Figure 5.6: Dose-volume histogram for a simulated patient.

Chapter 6

Future work

6.1 Ongoing investigations

This thesis presents a novel Monte Carlo dosimetry technique for TBI as well as the findings from a retrospective study. This project has given rise to several more opportunities for further research, and investigations to either use or improve this technique continue at present. Briefly outlined below are the areas for continued research.

Implementation for QA purposes: Several points must be considered before this MC technique can be implemented for routine clinical use. The technique would have to be implemented without significant disruption to the workflow and workload distribution of the clinical medical physicists. First and foremost, the amount of manual time involved in using the technique must be minimized. This includes the time involved in producing a pair of MC phantoms for a patient, converting MC simulation dose files to real dose files, importing to these files to MIM Maestro for registration, and contouring. Many of the steps involved in producing MC phantoms are already automatic, and with some additional modifications, this part of the pipeline may be able to run without manual intervention for standard treatments. Most of the steps in converting a MC dose file to a real dose file are also automatic already, and with the help of expert MIM Maestro users, these dose files may be able to be imported and deformed more efficiently. Contouring is a task that could be shared with other physicists, oncologists, or therapists depending on the concerns of the clinical team.

Additionally, computational time and resources must be considered. Cur-

rently, producing two sets of simulations with two billion particle histories takes around five hours using all 256 nodes of the clinical MC cluster, depending on the size of the patient. This is not only time consuming, but draws resources away from clinical MC and could clash with other research efforts in the clinic.

An important adjustment to this method for clinical implementation is to decrease the resolution of egsphant files to $0.5 \times 0.5 \times 0.5 \text{ cm}^3$ resolution, rather than the current $0.25 \times 0.25 \times 0.25 \text{ cm}^3$ resolution. The high resolution was used because this has been the default resolution for determination of lung compensator thickness (as described in section 3.3. By reducing the resolution, we will retain an acceptable level of accuracy in the data, decrease the computational time by an order of magnitude, and reduce the sizes of the egsphant and 3ddose files.

Finally, it may be possible to use even fewer histories to obtain clinically useful data. The optimization study in section 4.3.3 describes only a single treatment simulation and does not consider the fact that two simulations (one supine, one prone) may serve to de-noise each other out without running two simulations per position. If only one simulation is used per side, this cuts the computational cost of the technique by another 50%.

Changing the CT imaging protocol for TBI to include more critical organs: It would be valuable to collect dose-volume information from several OARs that were not included in this research because our existing TBI imaging protocol does not allow for the retrieval of these data. The most interesting missing organ would be the eyes, as cataractogenesis is a well-known and well-studied late toxicity of TBI, especially for pediatric patients. The brain and gonads would also be useful. Additionally, some team members have expressed interest in the dose delivered to the bones. If all of the pelvic bones, which contain bone marrow, were included in the CT imaging process, then meaningful data could be obtained representing all marrow-containing bones, rather than only the bones that happen to be included in the current CT protocol. At the time of writing this thesis, the protocol is changing to include a full-length CT (as far as possible in a single scan) and

this supplementary dose information would become available to the clinical team in the near future using this MC technique.

Additionally, the issue of missing scatter at superior-inferior edges of the patient, as described in section 5.2, would be solved with complete CT image volumes. Currently, we have worked around this issue by manually removing inferior and superior slices from our body contours, but this eliminates our ability to study these regions, such as the neck where overdosing is expected due to the smaller thickness. On a related note, we are currently discussing how we may incorporate bolus into a MC simulation. This may be too cumbersome to implement for routine QA, but if simulations with bolus were executed for one or two model patients, this would allow for an estimation of how far off our MC results are without accounting for bolus. Using a full-body CT will also mandate the previous suggestion of using a lower resolution for the MC phantoms because DOSXYZnrc has an inherent size limit of 512 slices in each dimension.

Testing the robustness to uncertainty in lung compensator positioning: A brief study is underway to assess the robustness of our current TBI technique against lung compensator positioning errors. By incrementally shifting the lung compensators several millimetres in superior-inferior and left-right directions and examining the resulting isodoses and organ dose information, we can get an idea for how forgiving our treatment is to this source of human error.

Validation of the deformable registration: This task is nontrivial and beyond the scope of this thesis. Expert users are able to qualitatively observe and guide the registration in MIM Maestro using the RegReveal and RegRefine tools, but meaningful metrics to describe the validity of this registration are unavailable, and would be very useful for this full-body prone-to-supine registration.

Exploring dose reduction within our current technique: We are currently investigating the extent to which further lung dose reduction may be achieved in our current technique, without a shift to VMAT or HT. Our TBI tech-

nique was commissioned to obtain a mean body dose of 12 Gy throughout the whole body. Many investigators have become interested in reducing the lung dose, although many TBI techniques are based on point dose calculations and organ dose information has not been obtainable. With our MC technique, we can explore the design of thicker compensators or different shapes of contours, adding a very useful degree of freedom to our treatment.

Developing and implementing a conformal VMAT technique: Finally, we re-state the long-term purpose of this research. While our TBI technique is effective, we hope to follow suit with several centers in the world in upgrading to a more conformal technique using the extensive VMAT experience at our centre. Discussions are underway to modify an existing field junctioning technique that is in place for craniospinal radiotherapy treatments for application to TBI, as well as discussions to treat the patient in a single position without needing to reposition the patient between beam arcs, similar to an approach described by Ouyang et al [105]. The organ dose data provided in Chapter 5 will serve as a basis for the development of this technique. In addition to the physics challenges of implementing a more conformal technique, the logistical challenges of moving a relatively simple planning process to an extremely advanced planning process, by moving from a point dose calculation to a full-body VMAT optimization, will need to be considered as well, in terms of physicist hours and linac availability in a clinic that is already operating at capacity.

6.2 Conclusion

A years-long effort at our centre to achieve MC simulations of TBI had been hindered by computational resources and technical challenges, but has finally been achieved owing to the patience and dedication of several physicists over the past decade. This MC technique has been validated and has already been informing clinical decisions about both individual treatment cases and big-picture changes to our treatment workflow. It has been shown that smaller TBI patients receive smaller doses than larger patients while still falling within tolerance levels from

prescription, and a basis for VMAT organ dose constraints is provided by the retrospective study. While the technique is currently optimized for retrospective data collection where time constraints are not an issue, it can and will be optimized for routine quality assurance purposes as well.

Bibliography

- [1] P Mazzarello. A unifying concept: the history of cell theory. *Nature Cell Biology*, 1(1):E13–E15, 1999. → page 3
- [2] A Bongso and M Richards. History and perspective of stem cell research. *Best Practice & Research Clinical Obstetrics and Gynaecology*, 18(6):827–842, 2004. → pages 3, 4
- [3] *Anatomy and Physiology*. OpenStax, Rice University, 2013.
<https://openstax.org/details/books/anatomy-and-physiology>. → pages 4, 5, 6, 7
- [4] M Ogawa, A C LaRue, and M Mehrotra. Hematopoietic stem cells are pluripotent and not just “hematopoietic”. *Blood Cells, Molecules and Diseases*, 51(1):3–8, 2013. → page 4
- [5] A V Hoffbrand and P A H Moss. *Hoffbrand's Essential Haematology*. Wiley-Blackwell, 7th edition, 2016. → pages 4, 5, 6, 9, 17
- [6] S Standring. *Gray's Anatomy: The Anatomical Basis of Clinical Practice*. Elsevier Limited, 41st edition, 2016. → pages 4, 7
- [7] B Clarke. Normal bone anatomy and physiology. *Clinical Journal of the American Society of Nephrology*, 3(Suppl 3):S131–S139, 2008. → page 4
- [8] R S Taichman. Blood and bone: two tissues whose fates are intertwined to create the hematopoietic stem-cell niche. *Blood*, 105(7):2631–2639, 2005. → page 5
- [9] D Hanahan and R A Weinberg. The hallmarks of cancer. *Cell*, (100):57–70, 2000. → pages 7, 8
- [10] S Pelengaris and M Khan. *Molecular Biology of Cancer: A Bridge from Bench to Bedside*. Wiley-Blackwell, 2nd edition, 2013. → page 8
- [11] S Mukherjee. *The Emperor of All Maladies*. Simon and Schuster, Inc., 2010. → pages 8, 12
- [12] D Hanahan and R A Weinberg. Hallmarks of cancer: the next generation. *Cell*, 144(5):646–674, 2011. → page 8

- [13] Canadian Cancer Society. Cancer types. <http://www.cancer.ca/en/cancer-information/cancer-type/see-all/?region=bc>. Accessed February 2018. → pages 9, 12
- [14] Dana-Farber Cancer Institute. Hematologic oncology cancer types and programs. <http://www.dana-farber.org/hematologic-oncology-treatment-center/cancer-types-and-programs/>. Accessed February 2018. → pages 9, 12, 13
- [15] A Chavez-Gonzalez, B Bakhshinejad, K Pakravan, M L Guzman, and S Babashah. Novel strategies for targeting leukemia stem cells: sounding the death knell for blood cancer. *Cellular Oncology*, 40(1):1–20, 2017. → page 9
- [16] M Dowling, M Kelly, and T Meenaghan. Multiple myeloma: managing a complex blood cancer. *British Journal of Nursing*, 25(16):S18–S28, 2016. → page 10
- [17] M Mohty and J Harousseau. *Handbook of Multiple Myeloma*. Springer International Publishing, 2015. → page 10
- [18] D A Arber, A Orazi, R Hasserjian, J Thiele, M J Borowitz, M M Le Beau, C D Bloomfield, M Cazzola, and J W Vardiman. The 2016 revision to the World Health Organization classification of myeloid neoplasms and acute leukemia. *Blood*, 127(20):2391–2405, 2016. → page 10
- [19] S H Swerdlow, E Campo, S A Pileri, N L Harris, H Stein, R Siebert, R Advani, M Ghielmini, G A Salles, A D Zelenetz, and E S Jaffe. The 2016 revision of the World Health Organization classification of lymphoid neoplasms. *Blood*, 127(20):2375–2390, 2016. → page 10
- [20] Canadian Cancer Society’s Advisory Committee on Cancer Statistics. Canadian cancer statistics 2017. Available at cancer.ca/Canadian-Cancer-Statistics-2017-EN.pdf. → page 10
- [21] M L Sorror, B M Sandmaier, B E Storer, G N Franke, G G Laport, T R Chauncey, E Agura, R T Maziarz, A Langston, P Hari, et al. Long-term outcomes among older patients following nonmyeloablative conditioning and allogeneic hematopoietic cell transplantation for advanced hematologic malignancies. *Journal of the American Medical Association*, 306(17):1874–1883, 2011. → page 12

- [22] L L Popplewell and S J Forman. Is there an upper age limit for bone marrow transplantation? *Bone Marrow Transplantation*, 29(4):277–284, 2002. → page 12
- [23] H Zhang, J Chen, and W Que. Allogeneic peripheral blood stem cell and bone marrow transplantation for hematologic malignancies: meta-analysis of randomized controlled trials. *Leukemia Research*, 36(4):431–437, 2012. → page 13
- [24] H E Johns and J R Cunningham. *The Physics of Radiology*. Charles C Thomas, 4th edition, 1983. → pages 13, 18
- [25] J T Bushberg, J A Seibert, E M Leidholdt, and J M Boone. *The Essential Physics of Medical Imaging*. Lippincott Williams and Wilkins, 4 edition, 2012.
- [26] F H Attix. *Introduction to Radiological Physics and Radiation Dosimetry*. John Wiley and Sons, 1st edition, 2004. → pages 13, 20
- [27] E J Hall and A J Giaccia. *Radiobiology for the Radiologist*. Lippincott Williams and Wilkins, 7th edition, 2012. → page 17
- [28] S Braunstein and J L Nakamura. Radiotherapy-induced malignancies: review of clinical features, pathobiology, and evolving approaches for mitigating risk. *Frontiers in Oncology*, 3:73, 2013. → page 17
- [29] E Hutton. The atom bomb that saves lives. *Maclean's Magazine*, 1952. February 15 issue. → pages 18, 19
- [30] G M Mora, A Maio, and D W O Rogers. Monte Carlo simulation of a typical 60-Cobalt therapy source. *Medical Physics*, 26(11):2494–2502, 1999. → pages 18, 58
- [31] H E Johns, L M Bates, E R Epp, D V Cormack, S O Fedoruk, A Morrison, W R Dixon, and C Garrett. 1,000-Curie Cobalt-60 units for radiation therapy. *Nature*, 168:1035–1036, 1951. Letter to the editor. → page 19
- [32] The Official Website of the Nobel Prize. Nobel prizes and laureates. https://www.nobelprize.org/nobel_prizes/. Accessed February 2018. → pages 21, 22
- [33] J A del Regato. *Radiological Oncologists: The Unfolding of a Medical Specialty*. Radiology Centennial, Inc., 1993. → page 21

- [34] A Barrett. Total body irradiation. *Reports of Practical Oncology and Radiotherapy*, 4(3):47–64, 2000. → pages 21, 22
- [35] C A Barker, T J LoSasso, and S L Wolden. Total body irradiation. <https://oncohemakey.com/total-body-irradiation-2/>. Clinical search engine for hematology and oncology. Accessed February 2018. → page 21
- [36] A C Heublein. A preliminary report on continuous irradiation of the entire body. *Radiology*, 18(6):1051–1062, 1932. → page 21
- [37] Advisory committee on human radiation experiments : final report, 1995. Produced by an advisory committee struck by US President Clinton. Official US Government document, publically available. → page 22
- [38] J P Merrill, J E Murray, J H Harrison, A Friedman, J B Dealy, and G J Dammin. Successful homotransplantation of the kidney between nonidentical twins. *The New England Journal of Medicine*, 262(25):1251–1260, 1960. → page 22
- [39] E D Thomas. A history of haemopoietic cell transplantation. *British Journal of Haematology*, 105(2):330–339, 1999. → page 22
- [40] C E Hill-Kayser, J P Plastaras, Z Tochner, and E Glatstein. TBI during BM and SCT: review of the past, discussion of the present and consideration of future directions. *Bone Marrow Transplantation*, 46(4):475–484, 2011. → pages 22, 23
- [41] H J Deeg, R Storb, G Longton, T C Graham, H M Shulman, F Appelbaum, and E D Thomas. Single dose or fractionated total body irradiation and autologous marrow transplantation in dogs: effects of exposure rate, fraction size, and fractionation interval on acute and delayed toxicity. *International Journal of Radiation Oncology Biology Physics*, 15(3):647–653, 1988. → page 23
- [42] R Storb, R Raff, H J Deeg, T Graham, F R Appelbaum, F G Schuening, H Shulman, K Seidel, and W Leisenring. Dose rate-dependent sparing of the gastrointestinal tract by fractionated total body irradiation in dogs given marrow autografts. *International Journal of Radiation Oncology Biology Physics*, 40(4):961–966, 1998. → page 23
- [43] J A O'Donoghue. Fractionated versus low dose-rate total body irradiation. radiobiological considerations in the selection of regimes. *Radiotherapy and Oncology*, 7(3):241–247, 1986. → page 23

- [44] L Peters. Discussion: The radiobiology bases of TBI. *International Journal of Radiation Oncology Biology Physics*, 6(6):785–787, 1980. → page 23
- [45] R A Clift, D Buckner, F R Appelbaum, S I Bearman, F B Petersen, L D Fisher, C Anasetti, P Beatty, W I Bensinger, K Doney, et al. Allogeneic marrow transplantation in patients with acute myeloid leukemia in first remission: a randomized trial of two irradiation regimens. *Blood*, 76(9):1867–1871, 1990. → page 23
- [46] M M Bortin, H E M Kay, R P Gale, and A A Rimm. Factors associated with interstitial pneumonitis after bone-marrow transplantation for acute leukaemia. *The Lancet*, 319(8269):437–439, 1982. → page 23
- [47] S Sampath, T E Schultheiss, and J Wong. Dose response and factors related to interstitial pneumonitis after bone marrow transplant. *International Journal of Radiation Oncology Biology Physics*, 63(3):876–884, 2005. → pages 23, 30
- [48] S A Carruthers and M M Wallington. Total body irradiation and pneumonitis risk: a review of outcomes. *British Journal of Cancer*, 90(11):2080–2084, 2004. → pages 23, 30
- [49] American College of Radiology (ACR) and American Society for Radiation Oncology (ASTRO). ACR-ASTRO practice parameter for the performance of total body irradiation. 2017. Clinical practice statement, revised regularly, publically available. → page 23
- [50] A Bacigalupo, K Ballen, D Rizzo, S Giralt, H Lazarus, V Ho, J Apperley, S Slavin, M Pasquini, B M Sandmaier, et al. Defining the intensity of conditioning regimens: working definitions. *Biology of Blood and Marrow Transplantation*, 15(12):1628–1633, 2009. → page 24
- [51] D R Adkins and J F DiPersio. Total body irradiation before an allogeneic stem cell transplantation: is there a magic dose? *Current Opinion in Hematology*, 15(6):555–560, 2008. → page 24
- [52] P H Wiernik, J M Goldman, J P Dutcher, and R A Kyle. *Neoplastic diseases of the blood*. Cambridge University Press, 5th edition, 2013. → page 24
- [53] J L Mikell, E K Waller, J M Switchenko, S Rangaraju, Z Ali, M Graiser, W A Hall, A A Langston, N Esiashvili, H J Khouri, et al. Similar survival for patients undergoing reduced-intensity total body irradiation (TBI)

versus myeloablative TBI as conditioning for allogeneic transplant in acute leukemia. *International Journal of Radiation Oncology Biology Physics*, 89(2):360–369, 2014. → page 24

- [54] S L McAfee, S N Powell, C Colby, and T R Spitzer. Dose-escalated total body irradiation and autologous stem cell transplantation for refractory hematologic malignancy. *International Journal of Radiation Oncology Biology Physics*, 53(1):151–156, 2002. → page 24
- [55] S Altouri, M Sabloff, D Allan, H Atkins, L Huebsch, D Maze, R Samant, and C Bredeson. Total body irradiation without chemotherapy as conditioning for an allogeneic hematopoietic cell transplantation for adult acute myeloid leukemia. *Case Reports in Hematology*, 2016. Article ID 1257679. → page 24
- [56] R C N Studinski, D J Fraser, R S Samant, and M S MacPherson. Current practice in total-body irradiation: results of a canada-wide survey. *Current Oncology*, 24(3):181–186, 2017. → pages 24, 25
- [57] S Giebel, L Miszczyk, K Slosarek, L Moukhtari, F Ciceri, J Esteve, N Gorin, M Labopin, A Nagler, C Schmid, and M Mohty. Extreme heterogeneity of myeloablative total body irradiation techniques in clinical practice. *Cancer*, 120(17):2760–2765, 2014. → pages 24, 25
- [58] S Peca. Informal survey conducted via email; results not published, shared via private communication. → page 25
- [59] S Hussein and E El-Khatib. Total body irradiation with a sweeping 60-Cobalt beam. *International Journal of Radiation Oncology Biology Physics*, 33(2):493–497, 1995. → pages 26, 43, 72
- [60] M D C Evans, R Larouche, M Olivares, P Léger, J Larkin, C R Freeman, and E B Podgorsak. Total body irradiation with a reconditioned cobalt teletherapy unit. *Journal of Applied Clinical Medical Physics*, 7(1):42–51, 2006. → page 26
- [61] R Ravichandran, J P Binukumar, C A Davis, S S Sivakumar, K Krishnamurty, Z Al Mandhari, and B Rajan. Beam configuration and physical parameters of clinical high energy photon beam for total body irradiation (TBI). *Physica Medica*, 27(3):163–168, 2011. → pages 26, 28
- [62] E J Bloemen-van Gurp, B J Mijnheer, T A M Verschueren, and P Lambin. Total body irradiation, toward optimal individual delivery: evaluation with

metal oxide field effect transistors, thermoluminescence detectors, and a treatment planning system. *International Journal of Radiation Oncology Biology Physics*, 69(4):1297–1304, 2007. → pages 28, 40

- [63] R Yao, D Bernard, J Turian, R A Abrams, and W Sensakovic. A simplified technique for delivering total body irradiation (TBI) with improved dose homogeneity. *Medical Physics*, 39(4):2239–2248, 2012. → pages 26, 27
- [64] R Chakarova and M Krantz. A Monte Carlo evaluation of beam characteristics for total body irradiation at extended treatment distances. *Journal of Applied Clinical Medical Physics*, 15(3):182–189, 2014. → pages 27, 28, 42
- [65] S V Harden, D S Routsis, A R Geater, S J Thomas, P J Taylor, R E Marcus, and M V Williams. Total body irradiation using a modified standing technique: a single institution 7 year experience. *The British Journal of Radiology*, 74(887):1041–1047, 2001. → page 27
- [66] B Schaeken, S Lelie, P Meijnders, D Van den Weyngaert, H Janssens, and D Verellen. Alanine/EPR dosimetry applied to the verification of a total body irradiation protocol and treatment planning dose calculation using a humanoid phantom. *Medical Physics*, 37(12):6292–6299, 2010. → pages 27, 40
- [67] L Papież, J Montebello, C DesRosiers, and E Papież. The clinical application of dynamic shielding and imaging in moving table total body irradiation. *Radiotherapy and Oncology*, 51(3):219–224, 1999. → page 27
- [68] M Chrétien, C Côté, R Blais, L Brouard, L Roy-Lacroix, and M Larochelle. A variable speed translating couch technique for total body irradiation. *Medical Physics*, 27(5):1127–1130, 2000. → pages 27, 28
- [69] A Hussain, J E Villarreal-Barajas, P Dunscombe, and D W Brown. Aperture modulated, translating bed total body irradiation. *Medical Physics*, 38(2):932–941, 2011. → page 27
- [70] S Ahmed, D Brown, S B S Ahmed, M B Kakakhel, W Muhammad, and A Hussain. Translating bed total body irradiation lung shielding and dose optimization using asymmetric MLC apertures. *Journal of Applied Clinical Medical Physics*, 17(2):112–122, 2016. → page 27
- [71] A Jahnke, L Jahnke, F Molina-Duran, M Ehmann, S Kantz, V Steil, F Wenz, G Glatting, F Lohr, and M Polednik. Arc therapy for total body

irradiation - a robust novel treatment technique for standard treatment rooms. *Radiotherapy and Oncology*, 110(3):553–557, 2014. → pages 27, 28

- [72] C Onal, A Sonmez, G Arslan, S Sonmez, E Efe, and E Oymak. Evaluation of field-in-field technique for total body irradiation. *International Journal of Radiation Oncology Biology Physics*, 83(5):1641–1648, 2012. → pages 28, 41
- [73] N Kirby, M Held, O Morin, S Fogh, and J Pouliot. Inverse-planned modulated-arc total-body irradiation. *Medical Physics*, 39(5):2761–2764, 2012. → page 28
- [74] S Park, J Kim, Y H Joo, J C Lee, and J M Park. Total body irradiation with a compensator fabricated using a 3D optical scanner and a 3D printer. *Physics in Medicine and Biology*, 62(9):3735–3756, 2017. → page 28
- [75] M Zhang, N Qin, X Jia, W J Zou, A Khan, and N J Tue. Investigation on using high-energy proton beam for total body irradiation (TBI). *Journal of Applied Clinical Medical Physics*, 17(5):90–98, 2016. → pages 29, 42
- [76] A Buchali, P Feyer, J Groll, G Massenkeil, R Arnold, and V Budach. Immediate toxicity during fractionated total body irradiation as conditioning for bone marrow transplantation. *Radiotherapy and Oncology*, 54(2):157–162, 2000. → page 30
- [77] A Della Volpe, A J M Ferreri, C Annaloro, P Mangili, A Rosso, R Calandrino, E Villa, G Lambertenghi-Deliliers, and C Fiorino. Lethal pulmonary complications significantly correlate with individually assessed mean lung dose in patients with hematologic malignancies treated with total body irradiation. *International Journal of Radiation Oncology Biology Physics*, 52(2):483–488, 2002. → page 30
- [78] C R Kelsey, M E Horwitz, J P Chino, O Craciunescu, B Steffey, R J Folz, N J Chao, D A Rizzieri, and L B Marks. Severe pulmonary toxicity after myeloablative conditioning using total body irradiation: an assessment of risk factors. *International Journal of Radiation Oncology Biology Physics*, 81(3):812–818, 2011. → page 30
- [79] M Abugideiri, R H Nanda, C Butker, C Zhang, S Kim, K Chiang, E Butker, M K Khan, A E Haight, Z Chen, and N Esiashvili. Factors influencing pulmonary toxicity in children undergoing allogeneic hematopoietic stem cell transplantation in the setting of total body irradiation-based

myeloablative conditioning. *International Journal of Radiation Oncology Biology Physics*, 94(2):349–359, 2016. → page 30

- [80] R A Schneider, J Schultze, J M Jensen, D Hebbinghaus, and R M Galalae. Long-term outcome after static intensity-modulated total body radiotherapy using compensators stratified by pediatric and adult cohorts. *International Journal of Radiation Oncology Biology Physics*, 70(1):194–202, 2008. → page 30
- [81] O I Craciunescu, B A Steffey, C R Kelsey, N A Larrier, C J Paarz-Largay, R G Prosnitz, N Chao, J Chute, C Gasparetto, M Horwitz, et al. Renal shielding and dosimetry for patients with severe systemic sclerosis receiving immunoablation with total body irradiation in the scleroderma: cyclophosphamide or transplantation trial. *International Journal of Radiation Oncology Biology Physics*, 79(4):1248–1255, 2011. → page 31
- [82] J Gerstein, A Meyer, K Sykora, J Fröhlauf, J H Karstens, and M Bremer. Long-term renal toxicity in children following fractionated total-body irradiation (TBI) before allogeneic stem cell transplantation (SCT). *Strahlentherapie und Onkologie*, 185(11):751–755, 2009. → page 31
- [83] J C Cheng, T E Schultheiss, and J Y C Wong. Impact of drug therapy, radiation dose, and dose rate on renal toxicity following bone marrow transplantation. *International Journal of Radiation Oncology Biology Physics*, 71(5):1436–1443, 2008. → page 31
- [84] H B Kal and M L van Kempen-Harteveld. Induction of severe cataract and late renal dysfunction following total body irradiation: dose-effect relationships. *Anticancer Research*, 29(8):3305–3309, 2009. → page 31
- [85] Y Belkacémi, M Ozsahin, F Pène, B Rio, J Laporte, V Leblond, E Touboul, M Schlienger, N Gorin, and A Laugier. Cataractogenesis after total body irradiation. *International Journal of Radiation Oncology Biology Physics*, 35(1):53–60, 1996. → page 31
- [86] Y Belkacémi, M Labopin, J Vernant, H G Prentice, A Tichelli, A Schattenberg, M A Boogaerts, P Ernst, A Della Volpe, A H Goldstone, et al. Cataracts after total body irradiation and bone marrow transplantation in patients with acute leukemia in complete remission: a study of the European Group for Blood and Marrow Transplantation. *International Journal of Radiation Oncology Biology Physics*, 41(3):659–668, 1998. → page 31

- [87] M L van Kempen-Harteveld, R Brand, H B Kal, L F Verdonck, P Hofman, A V Schattenberg, R W van der Maazen, J J Cornelissen, W M H Eijkenboom, J P van der Lelie, et al. Results of hematopoietic stem cell transplantation after treatment with different high-dose total-body irradiation regimens in five dutch centers. *International Journal of Radiation Oncology Biology Physics*, 71(5):1444–1454, 2008. → page 31
- [88] L M Vrooman, H R Millard, R Brazauskas, N S Majhail, M Battiwalla, M E Flowers, B N Savani, G Akpek, M Aljurf, R Bajwa, et al. Survival and late effects after allogeneic hematopoietic cell transplantation for hematologic malignancy at less than three years of age. *Biology of Blood and Marrow Transplantation*, 23(8):1327–1334, 2017. → page 32
- [89] M Faraci, S Barra, A Cohen, E Lanino, F Grisolia, M Miano, F Foppiano, O Sacco, M Cabria, R De Marco, et al. Very late nonfatal consequences of fractionated TBI in children undergoing bone marrow transplant. *International Journal of Radiation Oncology Biology Physics*, 63(5):1568–1575, 2005. → page 32
- [90] I Flandin, O Hartmann, J Michon, R Pinkerton, C Coze, J L Stephan, B Fourquet, D Valteau-Couanet, C Bergeron, T Philip, and C Carrie. Impact of TBI on late effects in children treated by megatherapy for stage IV neuroblastoma. a study of the French Society of Pediatric Oncology. *International Journal of Radiation Oncology Biology Physics*, 64(5):1424–1431, 2006. → page 32
- [91] D L Friedman, A Rovo, W Leisenring, A Locasciulli, M E D Flowers, A Tichelli, J E Sanders, H J Deeg, and G Socie. Increased risk of breast cancer among survivors of allogeneic hematopoietic cell transplantation: a report from the FHCRC and the EBMT-Late Effect Working Party. *Blood*, 111(2):939–944, 2008. → page 32
- [92] Mackie T R. History of tomotherapy. *Physics in Medicine and Biology*, 51(13):R427–R453, 2006. → page 33
- [93] K Otto. Volumetric modulated arc therapy: IMRT in a single gantry arc. *Medical Physics*, 35(1):310–317, 2008. → page 33
- [94] S K Hui, J Kapatoes, J Fowler, D Henderson, G Olivera, R R Manon, B Gerbi, T R Mackie, and J S Welsh. Feasibility study of helical tomotherapy for total body or total marrow irradiation. *Medical Physics*, 32(10):3214–3224, 2005. → pages 33, 38

- [95] A H Zhuang, A Liu, T E Schultheiss, and J Y C Wong. Dosimetric study and verification of total body irradiation using helical tomotherapy and its comparison to extended SSD technique. *Medical Dosimetry*, 35(4):243–249, 2010. → pages 33, 34
- [96] M Chao, J Peñagarícano, Y Yan, E G Moros, P Corry, and V Ratanatharathorn. Voxel-based dose reconstruction for total body irradiation with helical tomotherapy. *International Journal of Radiation Oncology Biology Physics*, 82(5):1575–1583, 2012. → page 34
- [97] J A Peñagarícano, M Chao, F Van Rhee, E G Moros, P M Corry, and V Ratanatharathorn. Clinical feasibility of TBI with helical tomotherapy. *Bone Marrow Transplantation*, 46(7):929–935, 2011. → pages 34, 35
- [98] T Magome, A Haga, Y Takahashi, K Nakagawa, K E Dusenberry, and S K Hui. Fast megavoltage computed tomography: a rapid imaging method for total body or marrow irradiation in helical tomotherapy. *International Journal of Radiation Oncology Biology Physics*, 96(3):688–695, 2016. → page 34
- [99] R Takenaka, A Haga, H Yamashita, and K Nakagawa. Adequate target volume in total-body irradiation by intensity-modulated radiation therapy using helical tomotherapy: a simulation study. *Journal of Radiation Research*, 58(2):210–216, 2017. → page 34
- [100] S Chakraborty, S Cheruliyil, R Bharathan, and G Muttath. Total body irradiation using VMAT (RapidArc): A planning study of a novel treatment delivery method. *International Journal of Cancer Therapy and Oncology*, 3(2), 2015. → pages 34, 35
- [101] A Gruen, W Ebell, W Wlodarczyk, O Neumann, J S Kuehl, C Stromberger, V Budach, and S Marnitz. Total body irradiation (TBI) using helical tomotherapy in children and young adults undergoing stem cell transplantation. *Radiation Oncology*, 8(92), 2013. → page 34
- [102] A Springer, J Hammer, E Winkler, C Track, R Huppert, A Böhm, H Kasparu, A Weltermann, G Aschauer, A L Petzer, et al. Total body irradiation with volumetric modulated arc therapy: Dosimetric data and first clinical experience. *Radiation Oncology*, 11(46), 2016. → pages 34, 36
- [103] R Takenaka, H Yamashita, T Toya, A Haga, S Shibata, M Kurokawa, K Ootomo, and K Nakagawa. Unique radiation dermatitis related to total

body irradiation by helical tomotherapy. *The Journal of Dermatology*, 43(11):1376–1377, 2016. → page 35

- [104] J A Molloy. Statistical analysis of dose heterogeneity in circulating blood: implications for sequential methods of total body irradiation. *Medical Physics*, 37(11):5568–5578, 2010. → page 36
- [105] L Ouyang, M Folkerts, Y Zhang, B Hrycushko, R Lamphier, P Lee, E Chambers, E Ramirez, R Reynolds, Y Yan, et al. Volumetric modulated arc therapy based total body irradiation: Workflow and clinical experience with an indexed rotational immobilization system. *Physics and Imaging in Radiation Oncology*, 4:22–25, 2017. → pages 36, 43, 86
- [106] C T Morrison, K L Symons, S J Woodings, and M J House. Verification of junction dose between VMAT arcs of total body irradiation using a Sun Nuclear ArcCHECK phantom. *Journal of Applied Clinical Medical Physics*, 18(6):177–182, 2017. → page 37
- [107] J H Kim, A Stein, N Tsai, T E Schultheiss, J Palmer, A Liu, J Rosenthal, S J Forman, and J Y C Wong. Extramedullary relapse following total marrow and lymphoid irradiation in patients undergoing allogeneic hematopoietic cell transplantation. *International Journal of Radiation Oncology Biology Physics*, 89(1):75–81, 2014. → pages 37, 38
- [108] S K Hui, M R Verneris, P Higgins, B Gerbi, B Weigel, SK Baker, C Fraser, M Tomblyn, and K Dusenbery. Helical tomotherapy targeting total bone marrow–first clinical experience at the University of Minnesota. *Acta Oncologica*, 46(2), 2007. → pages 37, 38
- [109] T E Schultheiss, J Wong, A Liu, G Olivera, and G Somlo. Image-guided total marrow and total lymphatic irradiation using helical tomotherapy. *International Journal of Radiation Oncology Biology Physics*, 67(4):1259–1267, 2007. → page 37
- [110] J Y C Wong, J Rosenthal, A Liu, T Schultheiss, S Forman, and G Somlo. Image-guided total-marrow irradiation using helical tomotherapy in patients with multiple myeloma and acute leukemia undergoing hematopoietic cell transplantation. *International Journal of Radiation Oncology Biology Physics*, 73(1):273–279, 2009. → page 37
- [111] C Han, T E Schultheiss, and J Y C Wong. Dosimetric study of volumetric modulated arc therapy fields for total marrow irradiation. *Radiotherapy and Oncology*, 102(2):315–320, 2012. → page 37

- [112] A Stein, J Palmer, N Tsai, M M Al Malki, I Aldoss, H Ali, A Aribi, L Farol, C Karanes, S Khaled, et al. Phase I trial of total marrow and lymphoid irradiation transplantation conditioning in patients with relapsed/refractory acute leukemia. *Biology of Blood and Marrow Transplantation*, 23(4):618–624, 2017. → page 38
- [113] S Hui, C Brunstein, Y Takahashi, T DeFor, S G Holtan, V Bachanova, C Wilke, D Zuro, C Ustun, D Weisdorf, et al. Dose escalation of total marrow irradiation in high-risk patients undergoing allogeneic hematopoietic stem cell transplantation. *Biology of Blood and Marrow Transplantation*, 23(7):1110–1116, 2017. → page 38
- [114] Y Takahashi, M R Verneris, K E Dusenberry, C T Wilke, G Storme, D J Weisdorf, and S K Hui. Peripheral dose heterogeneity due to the thread effect in total marrow irradiation with helical tomotherapy. *International Journal of Radiation Oncology Biology Physics*, 87(4):832–839, 2013. → page 38
- [115] M Zeverino, S Agostinelli, G Taccini, F Cavagnetto, S Garelli, M Gusinu, S Vagge, S Barra, and R Corvò. Advances in the implementation of helical tomotherapy-based total marrow irradiation with a novel field junction technique. *Medical Dosimetry*, 3(37):314–320, 2012. → page 38
- [116] A Nalichowski, D G Eagle, and J Burmeister. Dosimetric evaluation of total marrow irradiation using 2 different planning systems. *Medical Dosimetry*, 41(3):230–235, 2016. → page 39
- [117] Y Takahashi, S Vagge, S Agostinelli, E Han, L Matulewicz, K Schubert, R Chityala, V Ratanatharathorn, K Tournel, J A Peñagarìcano, et al. Multi-institutional feasibility study of a fast patient localization method in total marrow irradiation with helical tomotherapy: A global health initiative by the international consortium of total marrow irradiation. *International Journal of Radiation Oncology Biology Physics*, 91(1):30–38, 2015. → page 39
- [118] M Lavallée, L Gingras, M Chrétien, S Aubin, C Côté, and L Beaulieu. Commissioning and evaluation of an extended SSD photon model for PINNACLE3: an application to total body irradiation. *Medical Physics*, 36(8):3844–3855, 2009. → page 39
- [119] Y Akino, K P McMullen, and I J Das. Patterns of patient specific dosimetry in total body irradiation. *Medical Physics*, 40(4), 2013. → page 40

- [120] R P Patel, A J Warry, D J Eaton, C H Collis, and I Rosenberg. In vivo dosimetry for total body irradiation: five-year results and technique comparison. *Journal of Applied Clinical Medical Physics*, 15(4):306–315, 2014. → page 40
- [121] C M Lancaster, J C Crosbie, and S R Davis. In-vivo dosimetry from total body irradiation patients (2000-2006): results and analysis. *Australasian Physics & Engineering Sciences in Medicine*, 31(3):191–195, 2008. → page 40
- [122] N Lamichhane, V N Patel, and M T Studenski. Going the distance: validation of Acurus and AAA at an extended SSD of 400 cm. *Journal of Applied Clinical Medical Physics*, 17(2):63–73, 2016. → page 41
- [123] M Butson, M Haque, L Smith, E Butson, D Odgers, D Pope, T Gorjiana, M Whitaker, J Morales, A Hong, et al. Practical time considerations for optically stimulated luminescent dosimetry (OSLD) in total body irradiation. *Australasian Physical & Engineering Sciences in Medicine*, 40(1):167–171, 2017. → page 41
- [124] Z Liu, D Lack, J T Rakowski, C Knill, and M Snyder. Fast Monte Carlo simulation for total body irradiation using a 60-Co teletherapy unit. *Journal of Applied Clinical Medical Physics*, 14(3):133–149, 2013. → page 42
- [125] M Serban, J Seuntjens, E Roussin, A Alexander, J-R Tremblay, and W Wierzbicki. Patient-specific compensation for Co-60 TBI treatments based on Monte Carlo design: A feasibility study. *Physica Medica*, 32(1):67–75, 2016. → page 42
- [126] R Chakarova, K Müntzing, M Krantz, E Hedin, and S Hertzman. Monte Carlo optimization of total body irradiation in a phantom and patient geometry. *Physics in Medicine and Biology*, 58(8):2461–2469, 2013. → page 42
- [127] A Ito. Three-dimensional dose calculation for total body irradiation. In *Monte Carlo Transport of Electrons and Photons*, chapter 27. Plenum Press, New York, 1988. → page 43
- [128] J Lucido, C Yuen, M Pearson, and I Popescu. New CT-based planning method for TBI treatment. 2011. Abstract presented at the 2011 meeting of the American Association of Medical Physicists and Canadian Organization of Medical Physicists (AAPM-COMP). → pages 43, 44, 73

- [129] N Metropolis. The beginning of the Monte Carlo method. *Los Alamos Science*, 15:125–130, 1987. → pages 49, 50
- [130] R Eckhardt. Stan Ulam, John von Neumann, and the Monte Carlo method. *Los Alamos Science*, 15:131–137, 1987. → pages 49, 50
- [131] N Metropolis and S Ulam. The Monte Carlo Method. *Journal of the American Statistical Association*, 44(247):335–341, 1949. → page 50
- [132] W K Chan. *Theory and Applications of Monte Carlo Simulations*. InTech, 2013. → page 50
- [133] I Kawrakow. Accurate condensed history Monte Carlo simulation of electron transport. I. EGSnrc, the new EGS4 version. *Medical Physics*, 27(3):485–498, 2000. → pages 52, 53
- [134] I J Chetty, B Curran, J E Cygler, J J DeMarco, G Ezzell, B A Faddegon, I Kawrakow, P J Keall, H Liu, and C M C others Ma. Report of the AAPM Task Group No. 105: Issues associated with clinical implementation of Monte Carlo-based photon and electron external beam treatment planning. *Medical Physics*, 34(12):4818–4853, 2007. → page 52
- [135] G D Doolen and J Hendricks. Monte Carlo at work. *Los Alamos Science*, 15:142–143, 1987. → page 53
- [136] I Kawrakow, D W O Rogers, and B R B Walters. Large efficiency improvements in BEAMnrc using directional bremsstrahlung splitting. *Medical Physics*, 31(10):2883–2898, 2004. → pages 53, 59
- [137] A F Bielajew. *Fundamentals of the Monte Carlo method for neutral and charged particle transport*. 2016. Unpublished book, arising from course notes from a course the author taught at The University of Michigan, Ann Arbor, Michigan, USA.
- [138] I Kawrakow and M Fippel. Investigation of variance reduction techniques for Monte Carlo photon dose calculation using XVMC. *Physics in Medicine and Biology*, 45(8):2163–2183, 2000. → page 53
- [139] T Teke. Monte carlo techniques for patient specific verifications of complex radiation therapy treatments including TBI, VMAT and SBRT lung. 2012. Ph.D thesis at the University of British Columbia. → pages 58, 74
- [140] J Lobo and I A Popescu. Two new DOSXYZnrc sources for 4D Monte Carlo simulations of continuously variable beam configurations, with

applications to RapidArc, VMAT, TomoTherapy and CyberKnife. *Physics in Medicine and Biology*, 55(16):4431–4443, 2010. → page 58

- [141] A Savitzky and M J E Golay. Smoothing and differentiation of data by simplified least squared procedures. *Analytical Chemistry*, 36(8):1627–39, 1964. → page 59
- [142] I Kawrakow. On the de-noising of Monte Carlo calculated dose distributions. *Physics in Medicine and Biology*, 47(17):3087–3103, 2002. → pages 59, 60
- [143] I A Popescu, C P Shaw, S F Zavgorodni, and W A Beckham. Absolute dose calculations for Monte Carlo simulations of radiotherapy beams. *Physics in Medicine and Biology*, 50(14):3375–3392, 2005. → page 63
- [144] P B Johnson, K R Padgett, K L Chen, and N Dogan. Evaluation of the tool “Reg Refine” for user-guided deformable image registration. *Journal of Applied Clinical Medical Physics*, 17(3):158–170, 2016. → page 69
- [145] K Nie, J Pouliot, E Smith, and C Chuang. Performance variations among clinically available deformable image registration tools in adaptive radiotherapy – how should we evaluate and interpret the result? *Journal of Applied Clinical Medical Physics*, 17(2):328–340, 2016. → page 69
- [146] T Kataria, K Sharma, V Subramani, K P Karrthick, and S S Bisht. Homogeneity index: An objective tool for assessment of conformal radiation treatments. *Journal of Medical Physics*, 37(4):207, 2012. → page 76
- [147] A L McKenzie. Cobalt-60 gamma-ray beams. *British Journal of Radiology Supplement*, 25, 1996. → page 79